# Parametric Model for Astrophysical Proton-Proton Interactions and Applications

Niklas Karlsson

SLAC-R-890

Prepared for the Department of Energy
under contract number DE-AC02-76SF00515

Printed in the United States of America. Available from the National Technical Information Service, U.S. Department of Commerce, 5285 Port Royal Road, Springfield, VA 22161.

# Parametric Model for Astrophysical Proton-Proton Interactions and Applications

NIKLAS KARLSSON

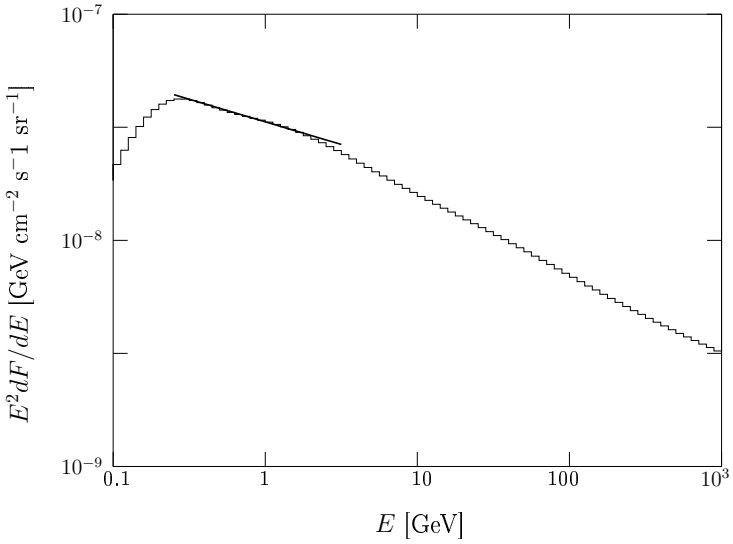


KTH Engineering Sciences

Doctoral Thesis in Physics
Stockholm, Sweden 2007


KTH Engineering Sciences

Doctoral Thesis in Physics

# Parametric Model for Astrophysical Proton-Proton Interactions and Applications

Niklas Karlsson

Particle and Astroparticle Physics, Department of Physics
School of Engineering Sciences
Royal Institute of Technology, SE-106 91 Stockholm, Sweden

Stockholm, Sweden 2007

Typeset in LaTeX

Cover illustration: Diffuse gamma-ray spectrum from the Large Magellanic Cloud calculated using matter column densities from ATCA/Parkes and NANTEN surveys, gamma-ray observations with EGRET and the proton-proton interaction model presented in this thesis. The solid line is the best-fit power law matching the observed EGRET spectrum in the EGRET energy range.

Akademisk avhandling som med tillstånd av Kungl Tekniska Högskolan framlägges till offentlig granskning för vinnande av teknologie doktorsexamen fredagen den 30 november 2007, kl 10.30 i sal FB55, AlbaNova Universitetscentrum, Roslagstullsbacken 21, Stockholm.
Avhandlingen försvaras på engelska.

ISBN 978-91-7178-779-8
TRITA-FYS 2007:74
ISSN 0280-316X
ISRN KTH/FYS/--07:74--SE


Printed by Universitetsservice US AB, 2007

# Abstract

Observations of gamma-rays have been made from celestial sources such as active galaxies, gamma-ray bursts and supernova remnants as well as the Galactic ridge. The study of gamma rays can provide information about production mechanisms and cosmic-ray acceleration. In the high-energy regime, one of the dominant mechanisms for gamma-ray production is the decay of neutral pions produced in interactions of ultra-relativistic cosmic-ray nuclei and interstellar matter.

Presented here is a parametric model for calculations of inclusive cross sections and transverse momentum distributions for secondary particles - gamma rays, $e^{\pm}$, $\nu_e$, $\bar{\nu}_e$, $\nu_\mu$ and $\bar{\nu}_\mu$ - produced in proton-proton interactions. This parametric model is derived on the proton-proton interaction model proposed by Kamae et al.; it includes the diffraction dissociation process, Feynman-scaling violation and the logarithmically rising inelastic proton-proton cross section. To improve fidelity to experimental data for lower energies, two baryon resonance excitation processes were added; one representing the $\Delta(1232)$ and the other multiple resonances with masses around 1600 MeV/c$^2$. The model predicts the power-law spectral index for all secondary particles to be about 0.05 lower in absolute value than that of the incident proton and their inclusive cross sections to be larger than those predicted by previous models based on the Feynman-scaling hypothesis.

The applications of the presented model in astrophysics are plentiful. It has been implemented into the Galprop code to calculate the contribution due to pion decays in the Galactic plane. The model has also been used to estimate the cosmic-ray flux in the Large Magellanic Cloud based on HI, CO and gamma-ray observations. The transverse momentum distributions enable calculations when the proton distribution is anisotropic. It is shown that the gamma-ray spectrum and flux due to a pencil beam of protons varies drastically with viewing angle. A fanned proton jet with a Gaussian intensity profile impinging on surrounding material is given as a more realistic example. As the observer is moved off the jet axis, the peak of the spectrum is moved to lower energies.



**Key words**: astrophysics, cosmic rays, gamma rays, proton-proton interactions

# Contents

# Chapter 1

# Introduction

Gamma rays constitute the highest energy band in the electromagnetic spectrum, ranging from a few hundred keV and above. Such energetic photons are produced in phenomena involving very-high energies. On Earth only particle accelerators are able to attain such energies, but the Universe is host to great numbers of gamma-ray emitting sources, including supernova remnants (SNRs), active galactic nuclei (AGN) and gamma-ray bursts (GRBs).

Although there is a widespread spectrum of source types producing cosmic gamma rays, the fundamental mechanisms involved in these sources are few and well-known physics processes; bremsstrahlung, synchrotron radiation, neutral pion decays and Compton up-scattering (sometimes referred to as inverse Compton scattering). In the GeV and TeV bands, commonly associated with gamma-ray astronomy, gamma-ray emission is dominated by the latter two.

A common requirement for both pion decay and Compton up-scattering is the acceleration of primary particles, nuclei and electrons, to high energies. In supernova remnants the expanding material can create shock fronts as it plows through the interstellar medium and in these shock fronts particles are accelerated. Escaping particles produce gamma rays as they interact with the interstellar medium, through the creation of neutral pions, or the interstellar radiation field, through Compton up-scattering of the low-energy ambient photons. Other sites of particle acceleration include active galactic nuclei, where the accretion of matter onto the black hole causes the formation of a jet of accelerated particles, accreting binary systems and gamma-ray bursts. Gamma-ray bursts emit copious amounts of energy in a very short period of time caused by, for example, core-collapsing high-mass stars or mergers of neutron stars in binary systems.

There is also a diffuse component of gamma-ray emission from the Galaxy, mainly in the Galactic ridge. This diffuse emission is presumed to be dominated by decays of neutral pions, which are created as high-energy cosmic rays interact with the interstellar matter (ISM; Stecker, 1973, 1989; Strong et al., 1978, 1982,

2000; Stephens & Badhwar, 1981; Dermer, 1986a; Hunter et al., 1997). The gamma-ray flux and spectral shape measured by the Energetic Gamma-Ray Experiment Telescope (EGRET; Hunter et al., 1997) is considered as the key attestation of this interpretation. Such diffuse emission may also be present in other galaxies with cosmic-ray content similar to our Galaxy. The Large Magellanic Cloud (LMC) was the only external galaxy detected as a gamma-ray source with EGRET (Sreekumar et al., 1992). Sreekumar et al. (1992) measured the integrated flux above 100 MeV over the entire LMC to be $(1.9\pm0.4)\times10^{-7}$ photons cm$^{-2}$ s$^{-1}$. In the third EGRET catalog, the LMC was detected as a point source with flux $(14.2\pm2.2)\times10^{-8}$ photons cm$^{-2}$ s$^{-1}$ and a power-law spectral energy distribution

$$\frac{dF}{dE} \propto E^{-\Gamma} \tag{1.1}$$

The spectral index $\Gamma$ was measured by EGRET to be $\Gamma = 2.20 \pm 0.20$ (Hartman et al., 1999). In the case of the Small Magellanic Cloud (SMC) EGRET was only able to determine an upper limit for the gamma-ray flux, about 1/3 of that from the LMC (Sreekumar et al., 1993). It has been suggested that the SMC is unable to confine cosmic rays enough to produce an observable gamma-ray flux. Upper-limit detections were also made for the Andromeda galaxy M31 and the giant radio galaxy M87 (Sreekumar et al., 1994). The latter has now been detected in TeV energies with the H.E.S.S. Cherenkov telescope array (Beilicke et al., 2005), although this TeV emission most likely comes from the AGN in the center. The low luminosity of galactic diffuse emission and the large distances involved makes it unlikely that many more galaxies will be detected as extended sources with future instruments.

Observations of gamma rays from AGNs have been made with EGRET as well as with atmospheric Cherenkov telescopes. Gamma-ray emission from AGN jets is commonly explained using leptonic models, where ambient photons are up-scattered on very-high-energy electrons in the jet. Support for this comes from the observed radio and X-ray spectra which match those of synchrotron radiation from high-energy electron populations. The apparent synchronization in the observed variability of X-ray and gamma-ray fluxes gives further support for the leptonic modeling (Ong, 1998; Schönfelder, 2001; Schlickeiser, 2002; Aharonian et al., 2004a). There are observations of AGN jets where the leptonic scenario faces difficulties and gamma-ray emission due to production of neutral pions in interactions between accelerated nuclei, mostly protons, and matter surrounding the AGN has been put forward as an alternative (Böttcher & Reimer, 2004; Mücke & Protheroe, 2001; Mücke et al., 2003). The synchrotron-proton blazar (SPB)[1] model (Reimer et al., 2004) is another approach to explain gamma-ray emission in AGNs where leptonic models seem to fail. The SPB model is less favorable because of the requirement of ultra-high-energy protons or very strong magnetic fields.

A multitude of gamma-ray sources are already known today (see, e.g., Hartman et al., 1999; Macomb & Gehrels, 1999; Ong, 2005) and with current and future

[1] A blazar is a type of AGN where the jet is pointing almost directly at the Earth.

gamma-ray telescopes covering GeV to TeV energies many more are expected to be found (Aharonian et al., 2003, 2004a,b; Ong, 1998; Schroedter et al., 2005; Schönfelder, 2001; Weekes, 2003a). The GeV energy window, in particular above 10 GeV, has been poorly explored. EGRET detected one single 18 GeV photon, associated with the gamma-ray burst GRB 940217 (Hurley et al., 1994). The GLAST Large Area Telescope (GLAST-LAT) is expected to provide high-statistics data from about 20 MeV up to several hundred GeV and will complement atmospheric Cherenkov telescopes currently in operation. Multi-wavelength observations will benefit immensely from data provided by the GLAST-LAT.

Interpretation of the observed gamma-ray spectra and identification of the involved interactions require not only high-quality observational data, but also good knowledge of the contributing mechanisms, which translates to having accurate models describing them. Kamae et al. (2005) concluded that the widely adopted models (Stecker, 1970, 1973; Strong et al., 1978; Stephens & Badhwar, 1981; Dermer, 1986a,b; Stecker, 1989; Mori, 1997; Strong et al., 2000, 2004) for gamma-ray production through neutral pion decay did not include all features of the inelastic proton-proton interaction process. They noted that the diffractive interaction and the violation of the Feynman-scaling hypothesis had been neglected. They also found that the inelastic proton-proton cross sections used were not up to date.

This thesis concerns the development of a phenomenological model in parametric form for the production of stable secondary particles in inelastic proton-proton interactions. The presented model incorporates the details of the proton-proton interaction mentioned above and enables accurate calculations of secondary particle spectra and transverse momentum distributions without time-consuming simulations. It will be a useful tool in the analysis of data from instruments such as the GLAST-LAT and in efforts to disentangle possible production mechanisms.

## 1.1 Outline of the Thesis

Chapter 1 has given a brief introduction to the topic and purpose of the work presented in this thesis. This is followed by an overview of the history and current understanding of cosmic rays in Chapter 2 and Chapter 3 introduces the area of gamma-ray astronomy and covers topics such as production mechanisms and the development of instruments for cosmic gamma-ray observations. The different approaches for detecting cosmic gamma rays will be described as well as scientific discoveries. The importance of proton-proton interactions is explained and Chapter 4 describes the proton-proton interaction model used in the present work. Chapter 5 describes the parametric model of secondary particle spectra and transverse momentum distributions derived from simulations of the proton-proton interaction model. The thesis is concluded with applications of the parametric model in Chapter 6 and conclusions and outlook in Chapter 7.

# Chapter 2

# Cosmic Rays

The term "cosmic ray" was first coined by Millikan in 1926 and is today referred to as particles produced in both Galactic and extragalactic sources. These particles range in energy from a few MeV to about $10^{20}$ eV (Yoshida et al., 1995), the most energetic particles ever detected. This should be compared with the energy levels of modern particle accelerators. For example, the Tevatron at Fermilab can produce center-of-mass (cm) energies of about 2 TeV and the Large Hadron Collider (LHC) at CERN will be able to produce 14 TeV in center of mass. This corresponds to proton energies of $1.9 \times 10^{15}$ eV and $9.2 \times 10^{16}$ eV in a collision with a stationary target. Cosmic rays provide insights to physics at energy levels presently unattainable with accelerator-based experiments; such as the conditions in the very young Universe.

## 2.1 History of Cosmic Rays

The very first evidence of the existence of cosmic rays came with the ground-breaking measurements of Victor Hess[1] in 1912. Before Hess, radiation of unknown origin had been detected on Earth and it was generally believed that this radiation originated in radioactive isotopes in the ground. Hess set out to test this hypothesis. If the theory was correct the radiation levels would decrease with altitude. He made flights with a hot-air balloon and used an electroscope to measure this strange radiation at different altitudes. The results were not the ones expected. Hess' measurements showed that the level of radiation first decreased, following the hypothesis, but then 1.5 km above sea level the radiation level began to increase continuously rather than continue to decrease as he went higher up in the atmosphere. He correctly proposed that the radiation was coming from high up in the atmosphere or even outside it rather than from the Earth. Following Hess' discovery, it was proposed that the Sun might be the source of this radiation. This hypothesis was falsified by Hess when he made measurements during the 1912 solar

[1] Victor Hess was awarded the Nobel Prize in 1936 for the discovery of cosmic rays.

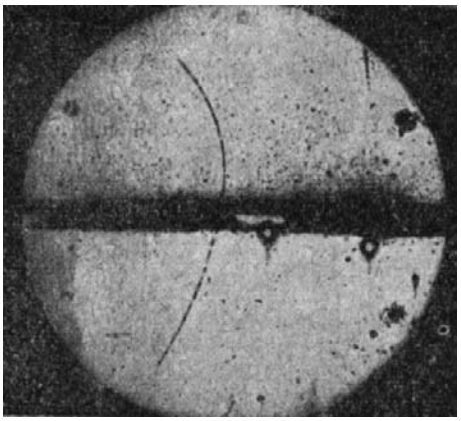

**Figure 2.1:** Track from a positron photographed in a cloud chamber by Anderson in 1932. The track shows a charged particle traveling upward, being bent in a magnetic field. Energy is lost in the lead plate in the middle, resulting in changed curvature of the track. Figure taken from the Wikimedia Commons.

eclipse. Hess' work was confirmed by further measurements made by Kolhörster in 1913 and 1914.

The development of new detectors played an important part in the early days of cosmic-ray physics. The first electroscope measurements by Hess only measured the ionization levels. Detection of separated events was made possible with the invention of the Geiger-Mueller detector in 1929. In the 1930's, cloud chambers were refined for use in cosmic-ray studies and in 1932 C. D. Anderson[2] discovered the first antiparticle, the positron, by studying cosmic rays. Using the cloud chamber, Anderson was able to photograph individual particle tracks as particles traversed a magnetic field in the cloud chamber. Some of the tracks where peculiar (see Figure 2.1). Anderson interpreted these as tracks from a particle with the same mass as the electron but with opposite charge. This was the particle that Dirac had predicted theoretically a few years earlier.

The discovery of the positron was soon followed by discoveries of a multitude of particles at the subatomic level. In 1935 Yukawa proposed a theory[3] where the interaction between protons and neutrons in the atomic nucleus is mediated by a particle with a mass of about 100 MeV/$c^2$. His proposed theory initiated the search for the pion, the force mediating particle in Yukawa's theory. In 1936 a particle with a mass near to what Yukawa had predicted was detected, but this turned out to be the muon, the electron's heavier cousin. The real pion was found about a

[2]Anderson shared the 1936 Nobel prize with Hess for the discovery of the positron.
[3]Yukawa was awarded the Nobel prize in 1949 following the discovery of the pion.

decade later by Powell and Occhialini. In the years to follow, many new particles were discovered in cosmic-ray based experiments, among them the K mesons.

The antiproton was first observed in 1955 (Chamberlain et al., 1955).[4] This discovery led to speculations on the existence of antimatter in the Universe. Motivated by reasons of symmetry it was believed that the Universe should contain equal amounts of matter and antimatter. Swedish physicist Alfvén[5] was one of the proponents of a Universe rich in antimatter. In such a Universe, stars and galaxies made up of antimatter might exist, as well as boundaries between antimatter and matter regions. In such boundaries, annihilation of matter and antimatter would produce neutral pions and observable fluxes of gamma rays. No such observations have been made. Further measurements with balloons and satellites have shown that there are only small amounts of antimatter in the Universe and this asymmetry is thought to be caused by a breaking of the matter-antimatter symmetry during the time of baryogenesis.

With the first particle accelerators in the 1950's the focus of cosmic-ray physics moved from particle physics to astrophysics. Instead of studying what cosmic rays are, which was quite clear from the 1940's and on, astrophysicists started using observations of cosmic rays to investigate, among many things, the origin of cosmic rays and how they are accelerated to the extreme energies observed.

## 2.2 Composition

In the early days of cosmic-ray physics, it was conjectured that the cosmic radiation discovered by Hess was electromagnetic in nature, hence the term *cosmic rays*. This was proven to be incorrect. Experiments performed in 1927 (Carlson, 2005) suggested that the cosmic-ray intensity should be affected by latitude. The cause for this effect is the Earth's magnetic field and these experiments suggested that cosmic rays were in fact charged particles. Rossi (1930) then proposed the East-West effect, in which the spatial distribution would feature an asymmetry depending on the charge of the cosmic-ray particles. In 1932, the first experimental evidence for this effect was found. Later on, in 1941, a balloon experiment performed by Schein et al. (1941) showed that cosmic rays are mostly protons.

Today, cosmic rays are widely known to consist of ionized nuclei, mostly protons and alpha particles, roughly 90% and 9% respectively. The rest is heavier nuclei and electrons and positrons. Gamma rays and neutrinos are also considered part of the cosmic-ray flux and even though only a small fraction of the cosmic-ray flux is photons (roughly 0.1%), cosmic gamma rays are important keys in the understanding of cosmic rays and the sites producing them. Cosmic gamma rays will be discussed in more detail in the next chapter.

[4] O. Chamberlain and E. Sergè were awarded the Nobel prize in 1959 for the discovery.

[5] H. Alfvén was awarded the Nobel prize in 1970 for his work in magnetohydrodynamics and plasma physics.

## 2.3 Cosmic-Ray Experiments

Many cosmic ray experiments have been conducted following the discovery and the early balloon experiments by Hess, Kolhörster, Schein and others in the first half of the 20th century. Because cosmic rays interact with atmospheric nuclei, these early experiments were flown with balloons to measure the primary cosmic rays. In recent years, satellite-borne cosmic-ray experiments have also been commissioned.

In the 1930's, Pierre Auger discovered the phenomenon of extensive atmospheric showers. As high-energy cosmic rays hit the Earth's atmosphere they will interact with atmospheric nuclei and cascades of secondary particles develop. For cosmic-ray nuclei the cascades are known as hadronic showers. Gamma rays initiate electromagnetic showers, as will be described in the next chapter. The initial interaction of a hadronic shower typically generates pions. Pions are unstable and their decays initiate secondary electromagnetic showers. The charged pions are relatively long-lived and as they traverse the atmosphere they can interact with atmospheric nuclei which extend the cascade. By measuring the particles in the atmospheric showers it is possible to indirectly detect cosmic rays and measure both energy and direction.

Measurements of cosmic rays, in particular the antimatter components of the cosmic-ray flux, may provide important answers for both particle physics and cosmology. Low-energy antiprotons are unique probes into elementary particle physics of the early Universe. The light nuclei present in the cosmic-ray flux are probes for cosmic-ray transport in the Galaxy and beyond. In the following, an overview over some important cosmic-ray experiments will be given.

### 2.3.1 Balloon and Satellite Experiments

The BESS (Balloon-borne Experiment with a Superconducting Spectrometer) is a joint American and Japanese cosmic antimatter experiment (Yamamoto et al., 2003; Abe et al., 2003; Mitchell et al., 2005). The BESS instrument uses a high-resolution spectrometer to measure the magnetic rigidity of incoming charged particles. Rigidity is defined as momentum per unit charge

$$R = \frac{pc}{Ze} \tag{2.1}$$

where $p$ is the momentum of a particle and $Z$ is the atomic number. A superconducting solenoidal coil provides a uniform magnetic field of 1 T and drift chambers track the particles inside the magnetic field. A Cherenkov counter and an electromagnetic shower counter provides particle identification. The instrument was first flown in 1993 and has been modified on a yearly basis. The latest version of the instrument is BESS-Polar (Yoshida et al., 2004).

The CAPRICE (Cosmic Anti-Particle Ring Imaging Cherenkov Experiment) instruments were also balloon experiments with the purpose to measure antiprotons, positrons and light isotopes with energies up to about 6 GeV. Built by the

WiZard collaboration[6], these instruments used a magnetic spectrometer to measure charged particle rigidities and used an imaging silicon-tungsten calorimeter and a ring imaging Cherenkov (RICH) detector for particle identification. Flights were made in 1994 with CAPRICE94 (Boetzio et al., 2000) and in 1998 with CAPRICE98 (Boetzio et al., 2004).

In 2006 the PAMELA (a Payload for Antimatter Matter Exploration and Light-nuclei Astrophysics; Picozza et al., 2007)[7] instrument was launched into orbit. It is the latest cosmic-ray instrument from the WiZard collaboration (earlier instruments include balloon experiments MASS (Grimani et al., 1989; Bellotti, 1999), TS93 (Aversa et al., 1997) and CAPRICE). Like its predecessor balloon experiment CAPRICE, the instrument uses a magnet spectrometer to measure charged particle rigidities, but it has a sampling imaging calorimeter for the separation of positrons from protons and electrons from antiprotons.

### 2.3.2 Atmospheric Shower Arrays

Several extensive air-shower experiments have been built. One of the earlier large-scale experiments was the Haverah Park array operated by the University of Leeds. In recent years, AGASA (Akeno Giant Air Shower Array; Chiba et al., 1992) and HiRes (High Resolution Fly's Eye; Abbasi et al., 2005) have been the two major atmospheric shower experiments.

AGASA used 111 surface plastic scintillator detectors and 27 muon detectors to sample the atmospheric shower. The entire array covered 100 $km^2$ with an average distance between detectors of about 1 km. HiRes on the other hand measured the fluorescence light emitted by nitrogen atoms in the atmosphere as they interact with particles in the shower. Because of the differences in how the two experiments measured the primary cosmic rays, the two experiments claimed different results for the very-highest energies. As will be discussed later, AGASA claimed to have seen cosmic rays with energies above the GZK cutoff but this could not be verified by HiRes.

The latest large-scale atmospheric shower experiment is the Pierre Auger observatory (Watson, 2007). To overcome the discrepancies between AGASA and HiRes, the Auger observatory is a hybrid of the two types, using both surface detectors and fluorescence detectors. This way, cross calibration can be made and the accuracy of the detector array is much improved. The observatory is currently in the final construction stage and taking data.

## 2.4 Origin

The observed spectrum of cosmic rays is shown in Figure 2.2. In the very lowest energy range, the spectrum is dominated by particles created in interactions with

[6]The WiZard collaboration website is located at http://wizard.roma2.infn.it.
[7]For more information on PAMELA, see http://wizard.roma2.infn.it/pamela.

the solar wind and magnetic fields in the solar system. In the higher energy range, above $E = 10^{10}$ eV, the spectrum features two distinct kinks, known as the *knee* at about $10^{15}$ eV and the *ankle* at about $10^{18}$ eV. Overall, the spectrum can be fitted by a broken power law

$$\frac{dF}{dE} \propto E^{-\Gamma} \tag{2.2}$$

with changes in spectral index $\Gamma$ at the two kinks. At the knee the the spectrum becomes softer, the spectral index changing from $\Gamma = 2.7$ to about 3. In the very-highest energy range, above the ankle, the spectrum hardens and the spectral index becomes $\Gamma = 2.8$.

The interpretation of this spectrum provides hints to the origin of cosmic rays. Cosmic rays above the ankle are energetic enough to prevent the local Galactic magnetic fields to contain them within the Galaxy. It has been suggested that these particles are of extragalactic origin, although their exact origin is not know today. The very low rate of these ultra-high-energy cosmic rays makes it hard to detect them; poor statistics makes it difficult to accurately determine their origin. AGNs have been proposed as possible candidates for acceleration of cosmic rays to ultra-high energies.

Particles below the knee, perhaps also above the knee and all the way up to the ankle, have lower energies and are most likely produced within the Galaxy. Supernova remnants have been proposed as likely candidates and there is good reason for this. Estimates of the power needed for the production of Galactic cosmic rays and the power produced by a typical supernova suggest the SNR scenario. Another piece of evidence for this scenario comes from the fact that the observed cosmic-ray spectrum is matched fairly close by the spectrum calculated using first-order Fermi acceleration in supernovae shocks.

Recent X-ray observations of SNR RX J1713-3946 with the Chandra telescope (Uchiyama et al., 2007) show evidence for strong magnetic fields on the order of milligauss; several orders of magnitude larger than that of the interstellar medium. The observations give strong evidence for magnetic field amplification in shock fronts, as predicted by diffusive shock acceleration (DSA; Vladimirov et al., 2006) models. The milligauss magnetic-field strength is a key condition for the acceleration of cosmic rays to $10^{15}$ eV energies. According to Uchiyama et al. (2007), the TeV gamma-ray emission observed with the H.E.S.S. Cherenkov telescope array (Aharonian et al., 2004a) is more likely caused by decays of neutral pions produced by interactions of accelerated cosmic rays and interstellar matter than Compton up-scattering of low-energy photons on ultra-relativistic electrons.

## 2.5 GZK Cutoff

The Greisen-Zatsepin-Kuzmin (GZK; Greisen, 1966; Zatsepin & Kuzmin, 1966) cutoff is a theoretical threshold for cosmic-ray energies. The threshold is derived from the predicted production of pions as ultra-high-energy cosmic rays interact

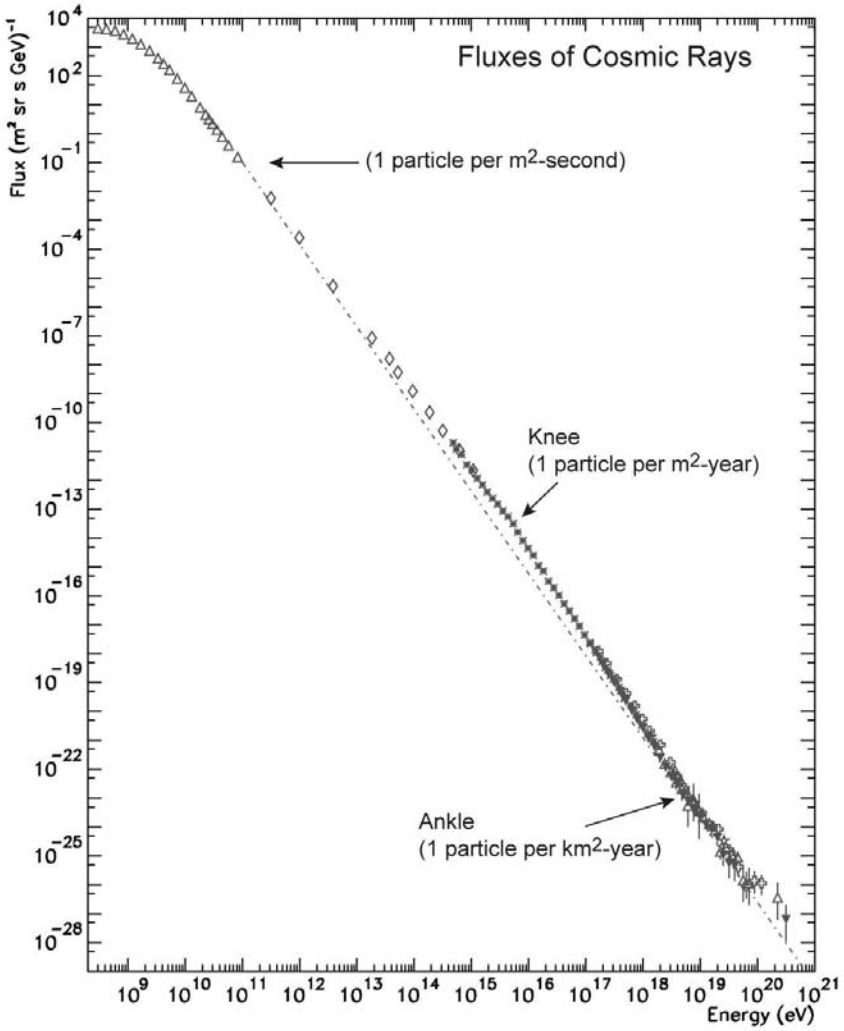


**Figure 2.2:** All particle cosmic-ray energy spectrum. The spectrum can be fitted fairly well with a broken power law, with index $\Gamma$ about 2.7 below the knee ($10^{15}$ eV), about 3.0 above it to the ankle ($10^{18}$ eV) and about 2.8 above the ankle. The different symbols represent data measured by different experiments. Figure is courtesy of S. Swordy.

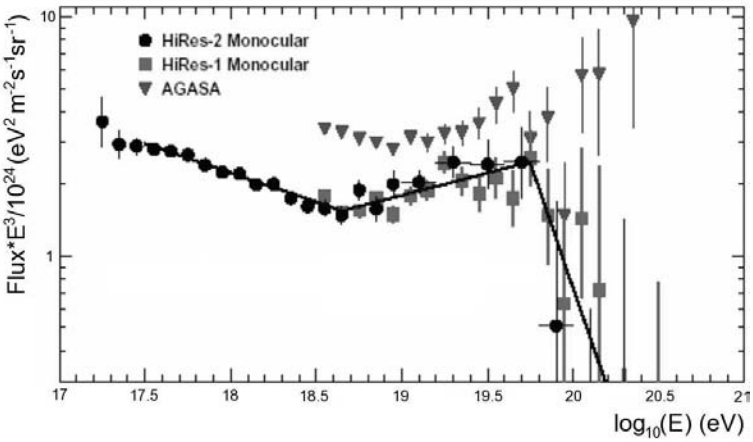


**Figure 2.3:** Cosmic-ray spectrum near the ankle as measured by the AGASA and HiRes experiments. Data points are filled triangles for AGASA, filled squares for HiRes-1 and filled circles for HiRes-2. The plot clearly shows the discrepancy between the two experiments with regards to the GZK limit at about $6 \times 10^{19}$ eV. Figure taken from Watson (2007).

with photons in the cosmic microwave background (CMB). Cosmic rays accelerated to energies above the threshold, about $6 \times 10^{19}$ eV, will suffer energy loss due to photo-pion production

$$p + \gamma \rightarrow \pi + X \tag{2.3}$$

with the CMB until the energy falls below the predicted threshold. $X$ represents any reachable state. From the mean free path of the interaction one can also derive a distance limit, such that no cosmic rays above the GZK cutoff should ever be observed from sources farther away than this distance limit. The resulting distance is of the order 50 Mpc (Lemoine & Sigl, 2001).[8]

Observations of cosmic rays with apparent energies above the GZK cutoff have been made with the AGASA experiment. This is known as the GZK paradox because the observations seem to contradict the current understanding of special relativity theory and the standard model of particle physics. The concurrent cosmic-ray experiment HiRes did not see cosmic rays above the cutoff. Figure 2.3 illustrates the cosmic ray spectrum near the ankle measured by the two experiments. The discrepancy between these two experiments is only in the 1-2 $\sigma$ range and it is likely that it is due to calibration errors rather than a true violation of the GZK cutoff.

The latest results from Auger show both the ankle in the cosmic ray spectrum and steepening of the spectrum above the ankle (Watson, 2007). It is unclear if this

[8]Parsec, symbol pc, is a unit of length and is about 3.26 ly (light years).

indicates a change from Galactic to extragalactic production of cosmic rays or if the GZK cutoff has been seen. Further data from the Auger experiment is required to verify this.

## 2.6 Acceleration Mechanisms

The cosmic ray spectrum in Figure 2.2 clearly shows that cosmic rays are somehow accelerated to ultra-high energies. The exact nature of the acceleration mechanisms is not known today. A first plausible mechanism was proposed by Fermi (1949) and later adapted for acceleration in supernova shock fronts (Bell, 1978; Blandford & Eichler, 1987).

According to Fermi's theory, a cosmic-ray spectrum with a power-law shape would arise under the assumption that charged particles are steadily injected into the accelerator, in which the energy gain is proportional to their energies, and that the process of particles escaping the accelerator is a Poisson process. Fermi proposed that the charged particles would gain energy in a stochastic process of collisions with a cloud of gas moving with velocity $U$ in which the average energy gain $\Delta E$ would be given by

$$\frac{\Delta E}{E} \propto \left(\frac{U}{c}\right)^2 \tag{2.4}$$

where $E$ is the particle energy. This is known as second order Fermi acceleration. Because the rate of acceleration is proportional to the square of the cloud velocity it is not efficient enough to produce the observed cosmic-ray energies. The acceleration is much more efficient if the collisions in the stochastic process are only head-on, i.e. in the direction of the movement of the cloud. Applying this, first order (because the energy gain is linearly proportional to the cloud velocity $U$) Fermi acceleration is obtained

$$\frac{\Delta E}{E} \propto \frac{U}{c} \tag{2.5}$$

The process of first order Fermi acceleration is illustrated in Figure 2.4. A flow of relativistic charged particles hits a gas cloud at rest which creates a shock front, indicated by the rectangles in the figure. The shock front will then move with a velocity $U$, on the order of $10^4$ km/s, much smaller than the velocities of the individual particles. The shock front is thin, the thickness of the shock front is much smaller than the gyro radii of the incident charged particles. Turbulence on both sides of the shock front causes the particles to traverse the front in either direction. The distribution of particle velocities becomes isotropic on both sides. Assuming the cloud to be an ideal gas and fully ionized, the shocked material downstream of the shock front will move with a velocity $U_{\text{down}} = 3U/4$. The shock gives rise to plasma turbulence in both the upstream and downstream region. Magnetic inhomogeneities are formed and these causes the charged particles to reflect back and forth over the shock multiple times in a stochastic process. The particles gain

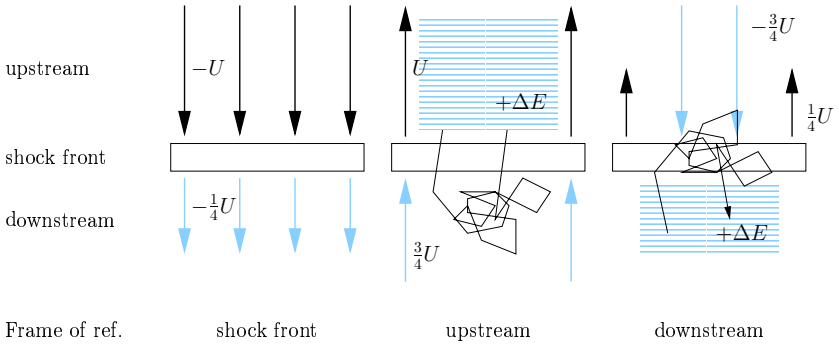


**Figure 2.4:** Illustration of first order Fermi acceleration in a shock front moving with velocity $U$ into an upstream medium. The gas is assumed to be an ideal gas. Left: In the rest frame of the shock front gas in the upstream region moves toward the front with speed $U$ and the downstream gas follows with speed $U/4$. Middle: In the rest frame of the upstream region the downstream gas hits particles at rest with speed $3U/4$. The particles scatter of the turbulence behind the shock front and gain $\Delta E$ in energy. Right: In the rest frame of the downstream region the velocity distribution downstream is isotropic. Particles diffusing from the downstream to the upstream region hit gas moving with speed $3U/4$ toward the shock front. Again, the particles gain an energy $\Delta E$ when traversing the shock front.

energy with each crossing until the particle is allowed to escape the accelerating region. The net energy gain $\Delta E$ per crossing under the ideal gas assumption is

$$\frac{\Delta E}{E} = \frac{2}{3}\frac{U}{c} \tag{2.6}$$

which is dependent on the energy $E$ of the particle. It then follows that the energy spectrum of the accelerated particles is a power law

$$\frac{dN}{dE} \propto E^{-\Gamma} \tag{2.7}$$

with a spectral index $\Gamma$ of about 2.

# Chapter 3

# Gamma-Ray Astronomy

## 3.1 Gamma-Ray Properties

Gamma rays are high-energy photons, the propagating particle of electromagnetic radiation. The corresponding wavelength is much shorter than the typical size of an atom. Because of this, a gamma ray will see the nucleus and electrons as individual particles, the atom as mostly empty space and the particle description is more compelling than the wave description. The characteristic property is energy, given by $E_\gamma = \hbar\nu$ and measured in units of eV, rather than frequency or wavelength. The wavelength of a gamma ray is shorter than the typical spacing between atoms in materials. Because of this it is virtually impossible to reflect gamma rays with mirrors and gamma-ray telescopes must rely on detection techniques different from optical and X-ray telescopes. Different methods for detection of gamma rays will be explained later in this chapter.

Photons are electrically neutral and therefore unaffected when passing through magnetic fields. They point back to their origin which makes gamma rays excellent and very important probes into high-energy processes in the Universe.

## 3.2 Production Processes

Chapter 1 mentioned the important mechanisms for production of cosmic gamma rays being bremsstrahlung, Compton up-scattering, neutral pion decay and synchrotron radiation. The diffuse emission above 100 MeV is dominated by neutral pion decays and gamma rays from point sources are commonly explained with Compton up-scattering of ambient photons on high-energy electrons. In the following sections each of these will be explained in some detail with the emphasis on neutral pion decays. For more detailed descriptions and derivations on bremsstrahlung, Compton up-scattering and synchrotron radiation, the reader is referred to textbooks by Longair (1994) and Rybicki & Lightman (2004).

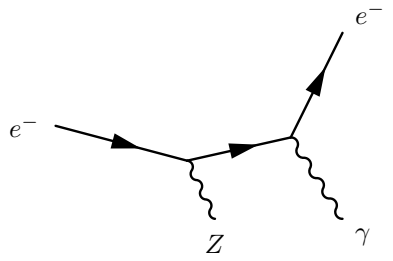


**Figure 3.1:** Feynman diagram illustrating electron bremsstrahlung in which the electron interacts with the Coulomb field of a nucleus Z and radiates a photon.

### 3.2.1 Bremsstrahlung

As charged particles pass through matter they interact with the Coulomb field of the nuclei causing energy loss and emission of radiation known as bremsstrahlung. The Feynman diagram in Figure 3.1 illustrates this process. The energy of the emitted photon is proportional to $1/m^2$, with $m$ being the rest mass of the incoming particle. In astrophysics, bremsstrahlung is mostly due to accelerated electrons and positrons. The photon spectrum due to bremsstrahlung is continuous and flat with a sharp energy cutoff (Schönfelder, 2001) at

$$E_\gamma = (\gamma - 1) m_e c^2 \tag{3.1}$$

where $\gamma$ is the Lorentz factor of the electron. The gamma-ray spectral index will be the same as for the initiating electron spectrum.

### 3.2.2 Compton Up-Scattering

Compton up-scattering is the process where low energy photons, typically cosmic microwave background (CMB) photons but infrared or optical photons in the interstellar radiation field (IRF) can also be up-scattered, interact with high-energy electrons or positrons and get boosted to higher energies. This is the "inverse" of regular Compton scattering, where energy is transfered from the photon to the charged particle. Figure 3.2 shows the corresponding Feynman diagram.

The gamma-ray energy due to inverse Compton scattering on electrons can be approximated by (Schönfelder, 2001)

$$E_\gamma \simeq \frac{1}{3} \left( \frac{E_e}{\mathrm{TeV}} \right)^2 \left( \frac{E_{\mathrm{ph}}}{2 \cdot 10^{-4} \mathrm{eV}} \right) [\mathrm{GeV}] \tag{3.2}$$

where $E_e$ is the electron energy and $E_{\mathrm{ph}}$ is the typical CMB photon energy.

In the Galactic-ridge spectrum, gamma rays due to bremsstrahlung and Compton up-scattering is expected to contribute significantly (Hayakawa, 1969; Schönfelder, 2001) in the sub-GeV to GeV range. For other sources, such as supernova remnants, the contribution depends heavily on the primary electron spectrum.

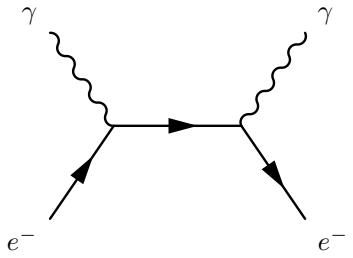


**Figure 3.2:** Feynman diagram illustrating Compton up-scattering. The low-energy photon $\gamma$ is boosted to higher energy by the electron it interacts with.

### 3.2.3 Synchrotron Radiation

Synchrotron radiation is the effect of charged particles gyrating around the field lines of strong magnetic fields, radiating as they are accelerated. The energy loss of the particle is given by

$$\frac{dW}{dt} = \frac{2c}{3} e^2 \beta^4 \left(\frac{E}{mc^2}\right)^4 \frac{1}{r^2} \tag{3.3}$$

where $m$ is the rest mass, $E$ is the energy of the particle and $r$ the gyro radius. The energy loss is proportional to $1/m^4$ and just as for bremsstrahlung, low-mass particles, such as electrons and positrons, emit synchrotron radiation much more efficiently. The energy attainable with the Large Electron-Positron collider (LEP) at CERN, which had a radius of 4.3 km, was limited to about 100 GeV because of synchrotron cooling of the accelerated electrons and positrons. The energy loss is also energy dependent, making synchrotron radiation important even for more massive particles at very-high energies. The Large Hadron Collider (LHC) will attain cms energies of about 14 TeV and the energy loss due to synchrotron radiation, which is dominated by the difference in mass between protons and electrons ($m_e/m_p \simeq 1/2000$), will be much less severe for the LHC.

An estimate of the photon energy, $E_\gamma$, due to a typical interstellar magnetic field is given by (Schönfelder, 2001)

$$E_\gamma \simeq 0.05 \left(\frac{E_e}{\mathrm{TeV}}\right)^2 \frac{B}{3\mu\mathrm{G}} [\mathrm{eV}] \tag{3.4}$$

where $E_e$ is the electron energy and $B$ is the magnetic field strength. From this equation it is clear that a higher electron energy, $E_e$, or a stronger magnetic field, $B$, increases the photon energy.

Synchrotron radiation from a population of electrons is commonly used to explain observed radio and X-ray spectra in various sources. Even though it is possible to produce gamma rays through synchrotron radiation it is less favorable because of the large magnetic field strength required. As mentioned in Chapter 1, the Synchrotron-Proton Blazar (SPB) model (Reimer et al., 2004) has been suggested

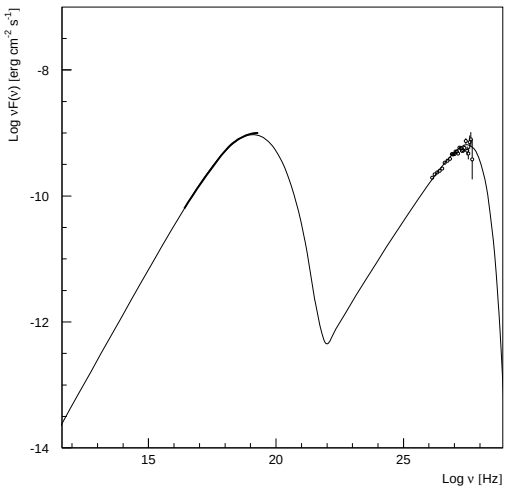


**Figure 3.3:** Observed X-ray (thick solid line) and TeV gamma-ray (open circles) spectral energy distribution (SED) of Mkn 501 together with the best-fit synchrotron self-Compton (SSC) model (thin solid). The distribution peaks in X-rays at $\nu \simeq 10^{19}$ Hz, about 10 keV in energy, and in gamma rays at $\nu \simeq 10^{27}$ Hz, about 1 TeV. Figure taken from Konopelko et al. (2003).

as an explanation of high-energy gamma-ray emission observed in some AGNs. In this model, protons instead of electrons gyrate around the magnetic field lines and emit synchrotron radiation. The drawback of this model is the requirement of very energetic protons and/or very large magnetic field strengths.

### 3.2.4 Synchrotron Self-Compton

If a population of electrons gives rise to synchrotron radiation there is a chance that the same electron population will interact with the emitted synchrotron radiation through Compton up-scattering, in a process referred to as synchrotron self-Compton (SSC). The physics processes are the same as mentioned above though the spectral energy distribution (SED) will feature two distinct peaks, both very similar to the peak of the synchrotron SED.

It is common to explain observed spectral energy distributions of blazars with SSC models and Konopelko et al. (2003) successfully fit the observed SED of both Mkn 421 and Mkn 501 in such manner. Figure 3.3 shows their best-fit SSC model for Mkn 501 together with observational data. The SED peaks in X-rays at about 10 keV and in gamma rays at about 1 TeV. The agreement is remarkably good.

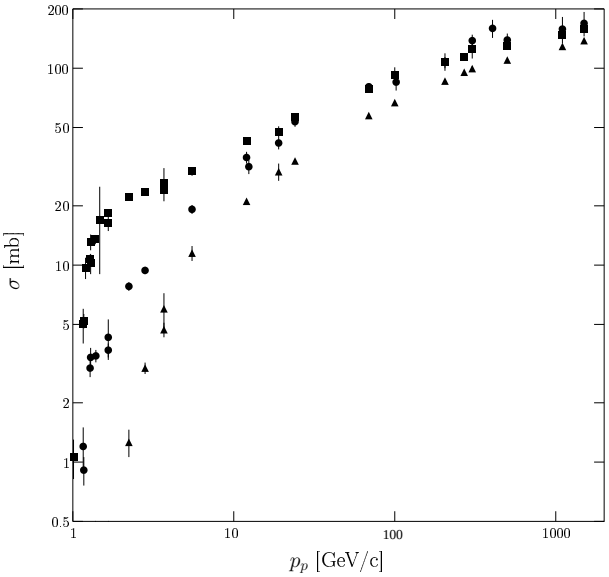


**Figure 3.4:** Inclusive cross sections for production of $\pi^0$ (circles), $\pi^+$ (squares) and $\pi^-$ (triangles) in p-p interactions as functions of proton momentum. Data are those of Table 1 in Dermer (1986b).

### 3.2.5 Pion Decay

Pions are copiously produced in hadronic interactions between cosmic-ray nuclei and interstellar matter, mostly proton-proton interactions, although there are contributions from interactions such as p-He, $\alpha$-p and $\alpha$-He;

$$p + p \rightarrow \pi + X \tag{3.5}$$

where $X$ represents any state reachable from the initial state. Pions are the lightest of the mesons, $m_{\pi^\pm} = 139$ MeV/c$^2$ and $m_{\pi^0} = 135$ MeV/c$^2$, and are most efficiently produced in these interactions. Only for high cms energies are heavier mesons and baryons, such as K-mesons, produced and these heavier particles have decay channels with pions in the final states.

The pion multiplicity is energy dependent as shown in Figure 3.4 where the inclusive cross section for production of $\pi^0$ and $\pi^\pm$ is plotted as function of proton momentum. Since the multiplicity is directly proportional to the inclusive cross section it is clear that the multiplicity increases rapidly with proton momentum around a few GeV/c.

The neutral pion ($\pi^0$) decay is predominantly

$$\pi^0 \rightarrow \gamma\gamma \tag{3.6}$$

while the charged pions ($\pi^{\pm}$) decay into electrons, positrons and neutrinos via muons;

$$\pi^+ \rightarrow \mu^+ + \nu_\mu \tag{3.7}$$
$$\pi^- \rightarrow \mu^- + \bar{\nu}_\mu \tag{3.8}$$

and

$$\mu^+ \rightarrow e^+ + \nu_e + \bar{\nu}_\mu \tag{3.9}$$
$$\mu^- \rightarrow e^- + \bar{\nu}_e + \nu_\mu \tag{3.10}$$

These secondary electrons and positrons may, if the conditions are right, contribute to the gamma-ray spectrum via bremsstrahlung or Compton up-scatterings. Kinematics of the decays are described in Appendix A. The modeling of proton-proton interactions is described in Chapters 4 and 5.

## 3.3 Brief History of Gamma-Ray Astronomy

In 1961, the first gamma-rays of cosmic origin were detected by an instrument on board the Explorer XI satellite (Kraushaar & Clark, 1962). This gamma-ray telescope was able to detect less than a hundred gamma-ray events. These appeared to be randomly spread over the sky, indicating a cosmic gamma-ray background. This discovery was the first of several major milestones in this new and exciting field of gamma-ray astronomy.

However, the birth of gamma-ray astronomy came earlier, in the 1950s, with predictions of the existence of cosmic gamma-rays (see references in Schönfelder, 2001, chapter 1). It was proposed by Hayakawa in 1952 that decays of neutral pions, produced by interactions in the interstellar medium (ISM), would produce cosmic gamma-rays. The same year, Hutchinson predicted gamma-ray emission due to bremsstrahlung. There were also papers, including one by Morrison in 1958, on the possibility of gamma-ray point sources. All these theoretical predictions opened up a new field and the quest to detect gamma-rays of cosmic origin.

Even though theoretical predictions existed, cosmic gamma-rays had never been detected on Earth because the Earth's atmosphere is opaque to high-energy gamma rays. A quantitative measure for this is the radiation length in air, which is $X_0 = 36.7$ g/cm$^2$, i.e. the atmosphere is more than 28 radiation lengths thick (Weekes, 2003b). To overcome this limitation, instruments were flown with rockets or balloons and later on even put on satellites to detect cosmic gamma rays. Detectors at the time were limited by poor statistics and high systematic uncertainties, making it difficult to measure gamma rays accurately.

With the next few satellite-borne gamma-ray observatories following the Explorer XI mission, exciting new insights into the gamma-ray sky were made. First out was the OSO-3 satellite in 1967 and it was followed by SAS-2 (1972) and COS-B (1975-1982). All three satellites confirmed the existence of the diffuse gamma-ray

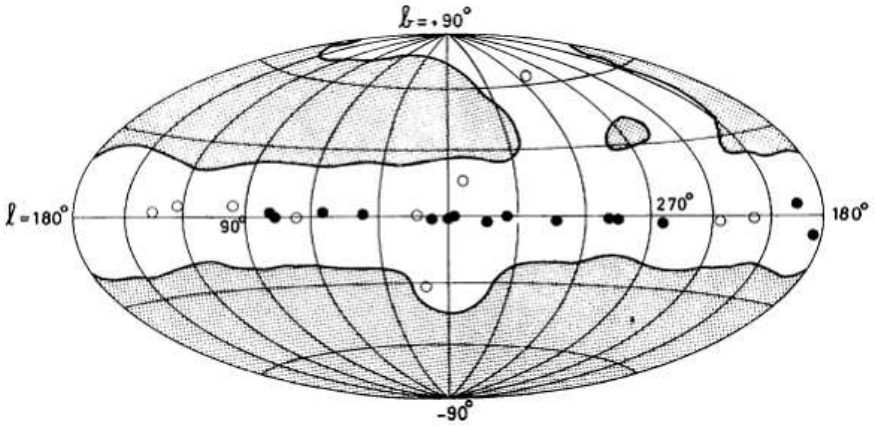


**Figure 3.5:** Second COS-B gamma-ray source catalog with the area of the sky surveyed (*unshaded*) and point sources above 100 MeV. Filled circles are point sources with fluxes larger than $1.3 \cdot 10^{-6}$ photons cm$^2$ s$^{-1}$. The sky map is in Galactic coordinates, a spherical coordinate system $(l, b)$, where Galactic latitude $b = 0$ is the Galactic plane and Galactic longitude $l = 0$ points toward the Galactic center. Figure taken from Swanenburg et al. (1981).

background and COS-B provided the first gamma-ray map of the Galaxy. With the COS-B instrument even quite a few gamma-ray point sources (Swanenburg et al., 1981) were detected. Figure 3.5 shows these sources on an all-sky map in Galactic coordinates, a spherical coordinate system $(l, b)$, where Galactic latitude $b = 0$ is the Galactic plane and Galactic longitude $l = 0$ points toward the Galactic center. The figure also shows the surveyed part of the sky.

## 3.4 The Compton Gamma-Ray Observatory

The next major milestone in gamma-ray astronomy came with the Compton Gamma-Ray Observatory (CGRO). The CGRO satellite incorporated four different instruments[1]: the Burst and Transient Source Experiment (BATSE), the Oriented Scintillation Spectrometer Experiment (OSSE), the Imaging Compton Telescope (COMPTEL) and the Energetic Gamma-Ray Experiment Telescope (EGRET). Together these instruments were designed to be sensitive to gamma rays from 30 keV to about 30 GeV.

With an energy range from 20 MeV to about 30 GeV, EGRET was the more important of the four instruments for the detection of high-energy gamma rays. Using

[1] More information on these instruments can be found on http://cossc.gsfc.nasa.gov/docs/cgro

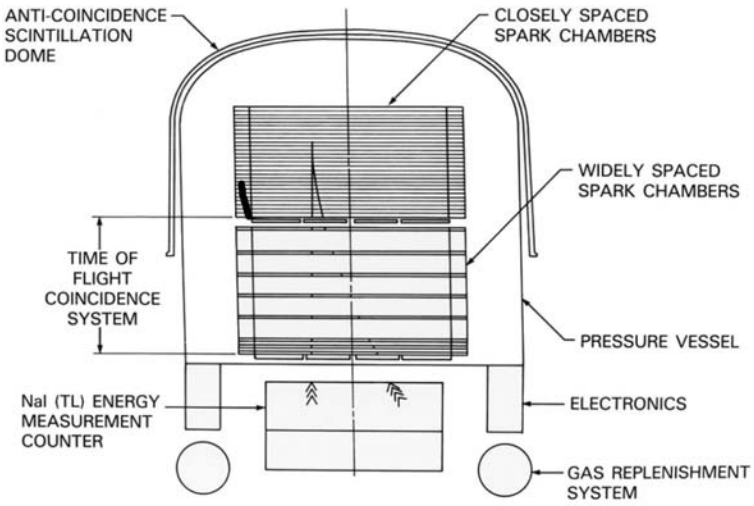


**Figure 3.6:** Schematic diagram of the Energetic Gamma-Ray Experiment Telescope (EGRET) flown on board the Compton Gamma-Ray Observatory (CGRO). The spark chambers are placed in the top of the instrument with the monolithic NaI calorimeter below them and covered by the anti-coincidence shield. The entire instrument was about 225 cm tall and 165 cm in diameter. Figure taken from Esposito et al. (1999).

high-voltage spark chambers, the direction of incident gamma rays could be determined through the tracks produced as the gamma rays pair-produce and initiate electromagnetic showers, causing sparks in the chambers. The gamma-ray energy would then be measured by the amount of energy deposited in the calorimeter[2], consisting of 36 NaI(Tl) crystal blocks optically coupled into one eight radiation lengths thick monolithic calorimeter, located below the spark chambers. The calorimeter was read out with photomultiplier tubes. A one-piece plastic scintillator covered the spark chambers and the calorimeter. Figure 3.6 shows a schematic diagram of the instrument which was about 225 cm tall and 165 cm in overall diameter.

Although the instrument was designed with an energy range up to about 30 GeV both detection efficiency and energy resolution were poor for energies above 10 GeV. Only about 2000 events were detected above 10 GeV. The detection efficiency was limited not only by weak source fluxes but also the decreasing effective area of the instrument and self-veto due to particles in the electromagnetic shower propagating backwards and hitting the anti-coincidence shield. The EGRET energy resolution was estimated to about 20% (rms) at 10 GeV and decreased rapidly with energy.

[2]For a correct measurement of the gamma-ray energy, the energy loss in the spark chamber must also be taken into account.

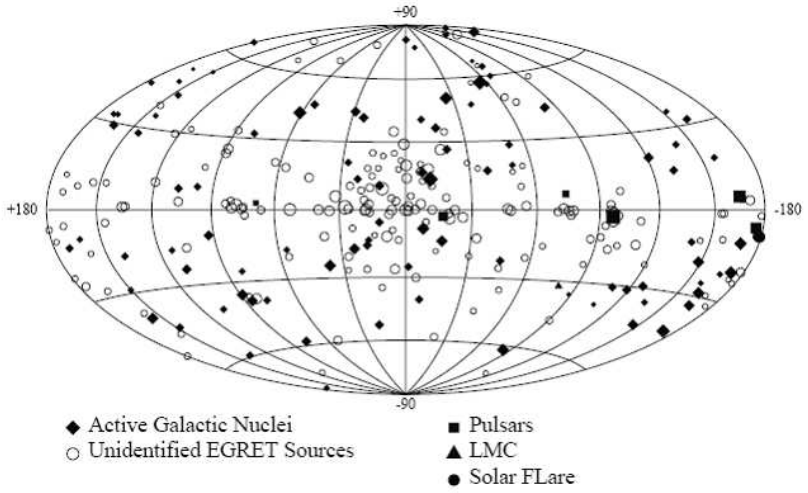


**Figure 3.7:** Third EGRET (3EG) catalog (Hartman et al., 1999) of gamma-ray source presented in Galactic coordinates for point sources with $E_\gamma > 100$ MeV. Diamonds represent AGNs, filled squares pulsars and open circles unidentified sources.

Noteworthy is also the long dead time, on the order of milliseconds due to the use of spark chambers in the tracker, for reading out event data when the instrument triggered. This limited the use of the instrument in studies of fast transient sources.

The main scientific objectives of EGRET were to survey the high-energy gamma-ray sky and to study point sources emitting high-energy gamma rays. It surpassed its predecessors COS-B and SAS-2 in both energy resolution and sensitivity and the mission was a great success. With EGRET, the discoveries of previous gamma-ray telescopes were confirmed. For the first time, a complete survey of the gamma-ray sky was made, and a large number of new point sources, many of them still unidentified, were detected. Figure 3.7 shows the third EGRET (3EG) catalog in Galactic coordinates for point sources with $E_\gamma > 100$ MeV.

Major discoveries with EGRET include the identification of blazars, a type of active galaxies known from optical and radio astronomy where the jet is pointing almost directly at the Earth, as emitters of gamma rays and the first gamma-ray pulsar, Geminga. EGRET provided the first all-sky map of the diffuse gamma-ray emission in the Galaxy, showing that most of this diffuse emission comes from the Galactic ridge, usually taken as the slice $|l| < 30°, |b| < 5°$ around the Galactic center. Hunter et al. (1997) found an excess of gamma rays in the GeV range in the EGRET Galactic diffuse spectrum compared to model predictions. This feature is now known as the "GeV excess". Many different ideas to explain this discrepancy have been put forward, including the work by Kamae et al. (2005).

Stecker et al. (2007) claims the excess is due to systematic errors caused by an incorrect instrument response function. Baughman et al. (2007), on the other hand, have shown that the excess is enhanced when previously unaccounted instrumental effects are taken into account. It is clear that the GLAST Large Area Telescope is crucial for the understanding of this excess.

## 3.5 The Gamma Ray Large Area Space Telescope

The Gamma Ray Large Area Telescope (GLAST)[3] is the next generation space-borne gamma-ray telescope scheduled for launch in early 2008. Its main instrument is the Large Area Telescope (LAT), which is designed to be sensitive to gamma rays in the 20 MeV to about 300 GeV energy range. GLAST is also equipped with a secondary instrument, the Gamma-ray Burst Monitor (GBM) for the specific purpose of monitoring gamma-ray bursts. The GBM will be sensitive to X-rays and gamma rays in the energy range between 8 keV and 25 MeV. This combination will make GLAST a very powerful gamma-ray burst detector. The GBM will not be described further in this thesis and the reader is referred to the descriptions given on the GLAST web page.

### 3.5.1 Large Area Telescope

The LAT instrument relies on the pair-conversion technique for the detection of gamma rays with energies in the MeV to multi-GeV range. A tracker, calorimeter and anti-coincidence shield work together to measure the energies and directions of incoming gamma rays. The pair-conversion technique is outlined in Figure 3.8 where an incoming gamma ray interacts in the tracker, producing an electromagnetic shower. The secondary particles in the shower leave tracks in the position sensitive detectors and then deposit their energies in the calorimeter. From the tracks the direction of the primary gamma ray can be reconstructed. The anti-coincidence shield provides veto against background charged particles.

The LAT instrument design is modular, consisting of 16 identical tower modules arranged in a $4 \times 4$ grid which are covered by a sectional anti-coincidence detector. Each detector tower consists of a silicon micro-strip tracker, a calorimeter and a data acquisition unit. A schematic view of the instrument is shown in Figure 3.9.

#### Tracker

The angular resolution of a pair-conversion telescope is limited by multiple scatterings at low-to-moderate energies and it is more preferable to have many thin layers. At high energies the angular resolution is limited by the position resolution of the detector elements in the tracker and the tracker depth. Therefore it is a trade of between number of layers and layer thickness to achieve good angular resolution

[3]GLAST Large Area Telescope, http://www-glast.stanford.edu

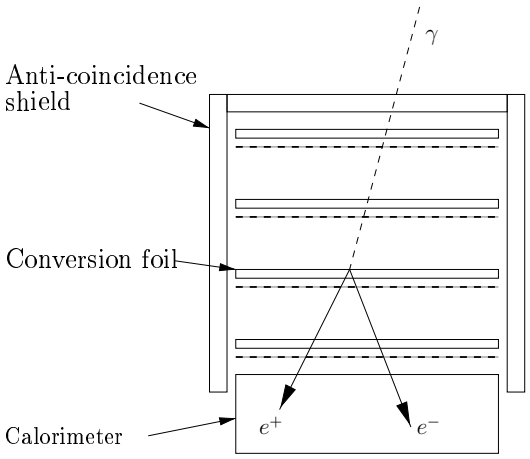


**Figure 3.8:** Outline of the pair-conversion technique used by the LAT for gamma-ray detection. An incoming gamma ray interacts in one of the conversion layers and produces an electron-positron pair. The direction of the primary gamma ray is reconstructed from the tracks of secondary charged particles in the tracker and the energy is measured by the calorimeter. The anti-coincidence shield vetoes against background charged particles.

over the entire energy range. In the LAT each tracker is composed of 19 trays (layers) of silicon micro-strip detectors. The layers are stacked with an alternating orientation of 90° to form a x-y position sensitive grid. The topmost 12 trays are light converter trays with thin, 3% radiation lengths, tungsten converter foil. The following four are thick converter trays with tungsten converter foil that is 18% radiation lengths thick and the lowermost three do not have any converter foil at all. The total radiation length of a tracker unit is $1.5X_0$.

### Calorimeter

The calorimeter must be thick enough to contain most of the electromagnetic shower. The energy resolution is limited by shower leakage out of the calorimeter and fluctuations in the shower development. The LAT calorimeter modules consist of eight layers, each with 12 CsI(Tl) detector elements. CsI(Tl) crystals were chosen in the detector elements for their high light yield. As in the tracker, the layers are stacked with alternating orientation to form a x-y grid. This way the shower development in the calorimeter can be tracked and direction measurements can be performed. This is crucial in order to correlate the calorimeter signal with tracks in the tracker and also allows for better background rejection. Each calorimeter module is $8.5X_0$ thick.

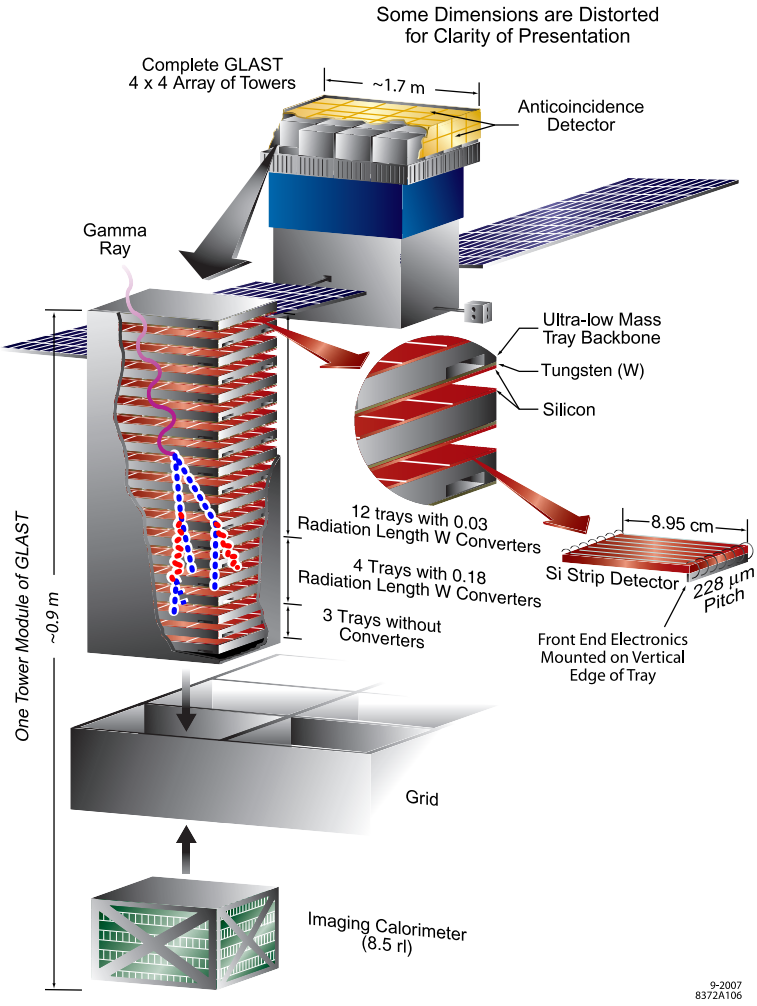


**Figure 3.9:** Conceptual layout of the Large Area Telescope. In the top of the figure the entire GLAST spacecraft is shown with the LAT sitting on top. In the middle is a blow-up of one of the 16 towers and also a view of a tracker tray. Each tracker consists of 19 trays. The 12 topmost trays have thin (0.03 radiation lengths, $X_0$, thick) tungsten converters, the following four layers have thick ($0.18X_0$ thick) tungsten converters and the last three layers have no converter at all. Each tracker is $1.5X_0$. In the bottom a calorimeter module is shown. Each calorimeter module is $8.5X_0$. Figure provided by the SLAC InfoMedia department.

**Table 3.1:** Summary of GLAST-LAT specification and performance quantities compared with those for EGRET. Data taken from the official GLAST-LAT web page: http://www-glast.stanford.edu.

| Quantity | LAT (min spec.) | EGRET |
|---|---|---|
| Energy range | 20 MeV - 300 GeV | 20 MeV - 30 GeV |
| Peak effective area[a] | $> 8000$ cm$^2$ | 1500 cm$^2$ |
| Field of view | $> 2$ sr | 0.5 sr |
| Angular resolution[b] | $< 3.5^\circ$ (100 MeV) | $5.8^\circ$ (100 MeV) |
| | $< 0.1^\circ$ ($> 10$ GeV) | |
| Energy resolution[c] | $< 10\%$ | 10% |
| Dead time per event | $< 100$ $\mu$s | 100 ms |
| Source Location Determination[d] | $0.5'$ | $15'$ |
| Point-source sensitivity[e] | $6 \times 10^{-9}$ cm$^{-2}$s$^{-1}$ | $10^{-7}$ cm$^{-2}$s$^{-1}$ |

[a] After background rejection
[b] Single photon, 68% containment, on-axis
[c] 1-$\sigma$, on-axis
[d] 1-$\sigma$ radius, flux $10^{-7}$ cm$^{-2}$s$^{-1}$ ($> 100$ MeV), high $|b|$
[e] $> 100$ MeV, at high $|b|$, for exposure of one-year all sky survey, photon spectral index -2

#### Anti-Coincidence Detector

During flight the charged particle background is on the order of $10^6$ (at 10 GeV) events for each gamma-ray event and this background has to be rejected. This is done with the anti-coincidence detector (ACD). The ACD is a sectional plastic-scintillator detector. As a charged particle interacts in the detector, electrons in the plastic polymers are excited to higher energy levels giving rise to scintillation light. The energy distribution and time behavior of the signal from the detector is used to differentiate between different particles.

One of the problems with the monolithic ACD that covered the EGRET instrument is self-veto of true gamma-ray events. As a shower develops in the tracker and/or calorimeter there is a chance of back splash into the ACD causing self-veto. By using a sectional ACD it is possible to correlate the reconstructed direction with the vetoing ACD tile and self-veto can be minimized.

### 3.5.2 Specifications

The overall design of the LAT gives great improvements over its predecessor EGRET. For example, the field of view (FOV) is more than 2 sr which is about twice as wide as that of EGRET and the on-axis effective area is larger than 8000 cm$^2$ for energies above 1 GeV which is more than seven times the effective area of EGRET. All of the LAT specification and performance quantities are tabulated in Table 3.1.

### 3.5.3 Scientific Goals

The LAT is expected to provide new insights and increased scientific understanding of all types of gamma-ray sources, from the Sun and the Moon to Galactic sources like SNRs and pulsars and extragalactic sources such as AGNs and GRBs. EGRET provided the first detailed all-sky map of the Galactic diffuse emission and the LAT will with its increased angular resolution provide an even more detailed sky-map showing the structure and distribution of the diffuse emission. The gamma-ray spectrum measured by EGRET shows an apparent excess of gamma-rays above 1 GeV over model predictions. Several ideas, including contributions from dark matter annihilation and systematic errors in the data (Stecker et al., 2007), have been put forward as explanations to this excess. With high-statistics data from the LAT it will be possible to determine if this excess is real or instrumental. The LAT will also detect, and perhaps even resolve, the extragalactic background light (EBL). It will be possible to determine whether or not the EBL is truly diffuse or if it is due to many but very faint point sources.

The 3rd EGRET catalog contains a large number of unidentified sources. The limitations of the EGRET instrument, such as its poor angular resolution, have made it impossible to match these sources with known sources in other wavebands, such as optical and X-rays. With data provided by the LAT it is very likely that most of these sources will be pinned down and matching counterparts found.

It has been estimated that GLAST will detect thousands of GeV blazars (Dermer, 2006; Stecker & Salamon, 1996; Chiang & Mukherjee, 1998; Mücke & Pohl, 2000). Most of these will be faint distant blazars which requires observations over long time to give reasonable integrated high-energy SEDs. The LAT will provide the sensitivity and life-time to achieve this.

If there are weakly interactive massive particles (WIMPs) contributing to the dark matter content of the Universe, the LAT may provide indirect detection of WIMP annihilation. A good WIMP candidate is the neutralino which is the lightest stable super-symmetric particle. The neutralino may pair-annihilate to quarks which will produce gamma-rays through neutral pion decay. It has been suggested that WIMPs may cluster together in the Galactic halo. Such clusters may be detected as dark-matter sources. Baltz et al. (2007) have found that the gamma-ray spectrum due to WIMP annihilation is nearly unique and distinguishable from other astrophysical sources. According to Bergström et al. (2007), the LAT is sensitive to a WIMP annihilation cross section times velocity, $\langle \sigma v \rangle$, on the order of $10^{-25}$ to $10^{-26}$ cm$^3$ s$^{-1}$.

There is also the possibility that that the LAT will detect gamma ray lines from WIMP annihilation into $\gamma\gamma$ or $Z^0\gamma$ final states. The energy of the gamma ray is directly related to the mass of the WIMP. For the $\gamma\gamma$ final state the gamma-ray energy is $E_\gamma = m_\chi/2$ and for the $Z^0\gamma$ final state it is

$$E_\gamma = m_\chi - \frac{m_Z^2}{4m_\chi} \tag{3.11}$$

where $m_\chi$ is the neutralino mass and $m_Z$ is the mass of the $Z^0$ boson. Edmonds et al. (2007) have shown that the GLAST sensitivity to detect gamma-ray lines from WIMP annihilation in the Milky Way is WIMP model independent but depend on the gamma-ray background model. The sensitivity is energy dependent but is typically on the order of $10^{-9}$ photons cm$^{-2}$ s$^{-1}$ sr$^{-1}$.

## 3.6 Atmospheric Cherenkov Telescopes

While traditional instruments are spacebourne to avoid the limitations of the opaque atmosphere, they are limited in size and thus limits the energy range to MeV to multi-GeV. To detect even higher-energy gamma rays, ground base atmospheric Cherenkov telescopes can be used. Such telescopes were first built in the 1960's, but the breakthrough came with the 10 m Whipple telescope located at the Fred Lawrence Whipple Observatory. Atmospheric Cherenkov Telescopes (ACTs) use the atmosphere as an active part of the detector and observe Cherenkov light produced by high-energy particles in the atmosphere. Because of the energy threshold of ground-based telescopes and the limited energy range of spacebourne instruments the two complement each other nicely.

The concept of Cherenkov radiation, named after Russian physicist Cherenkov[4], is based on super-luminal particles traversing materials. While relativity postulates a universal constant for the speed of light in vacuum, $c$, the speed of light in a given material can be significantly less than $c$. It is possible to accelerate particles to energies such that they are super-luminal in the given material. Such a particle will produce Cherenkov radiation in analogy with the sound waves of a sonic boom.

As cosmic rays and cosmic gamma rays enter the atmosphere, hadronic or electromagnetic showers of secondary particles are initiated. For electromagnetic showers, this begins with the interaction of a primary gamma ray and a heavy nucleus resulting in an electron-positron pair. As these secondary particles suffer the effects of bremsstrahlung more photons are produced which will pair-produce and a cascade of charged particles is developed in the atmosphere. When the energy of the primary gamma ray is in the GeV to TeV range, the secondary particles in the developing shower will be energetic enough to produce Cherenkov radiation as they traverse the atmosphere. The Cherenkov radiation forms a thin pool of light moving in the direction of the shower. This pool is typically a few hundred meters in diameter and a few nano-seconds in thickness, which corresponds to a few tenths of a meter. The opening angle of the Cherenkov light cone is on the order of one or a few degrees.

### 3.6.1 Detection Techniques

There are basically two types of atmospheric Cherenkov Telescopes used to detect the Cherenkov light pool: the imaging technique used by imaging atmospheric

[4]P. A. Cherenkov was awarded the 1958 Nobel prize for his work on Cherenkov radiation.

Cherenkov Telescopes (IACTs) and the wave-front-sampling technique and the two are quite different in how the primary gamma ray is detected. Imaging atmospheric Cherenkov Telescopes use a large steerable mirror to collect and focus the Cherenkov light onto a camera taking an actual picture. Even though the collecting mirror is quite large, the Whipple mirror was 10 m across, the telescope can only capture a fraction of the entire Cherenkov pool. This affects the energy threshold which is on the order of a few hundred GeV. The advantage of the direct imaging is good background rejection. Gamma-ray events cause electromagnetic showers, whereas most cosmic rays (protons and heavier nuclei) initiate hadronic showers. The two have distinct differences which makes it possible to separate hadronic cosmic-ray events from true gamma-ray events based on the image of the shower. Figure 3.10 illustrates the differences in the longitudinal shower development between a photon-induced electromagnetic shower (simulated 300 GeV gamma ray) and a proton-induced hadronic shower (simulated 1 TeV proton).

The electromagnetic shower develops mainly through three-particle interactions such as bremsstrahlung and pair production, whereas hadronic showers involve complex hadronic interactions as well as secondary electromagnetic showers. The proton-induced hadronic shower is initiated by the interaction of the proton with a proton or heavy nucleus in the atmosphere which produces nucleons, pions and other heavier hadrons if the proton energy is sufficient enough. The neutral pion decays into two gammas which initiate a secondary electromagnetic shower. The charged pions decay into muons and then electrons and positrons which also can initiate secondary electromagnetic showers. The produced nucleons can induce secondary hadronic showers. As a consequence, hadronic showers will have much larger longitudinal extent and a lateral density profile which is much more irregular and fluctuates more as shown in Figure 3.10.

Detectors using the wave-front-sampling technique cover a large area with small detectors that sample a much larger portion of the Cherenkov light pool. The much greater area compared with IACTs enables the energy threshold of the detector to be pushed down to energies below 100 GeV. The lack of direct imaging makes it much harder to reject hadronic showers initiated by cosmic rays.

In recent years, telescopes combining the direct imaging with wavefront sampling have been constructed. Both the H.E.S.S. Cherenkov telescope array and VERITAS (Very Energetic Radiation Imaging Telescope Array System) now use an array of four imaging telescopes. Each telescope takes a direct image of the Cherenkov light pool and together they sample the entire shower over a larger area. The direct imaging enables good background rejection and the energy threshold is as low as 50 GeV.

### 3.6.2 Scientific Achievements

The first observations of cosmic gamma rays in TeV energies were made with the 10m Whipple imaging Cherenkov telescope located at the Fred Lawrence Whipple Observatory. Early detections include the Crab Nebula (Weekes et al., 1989) and

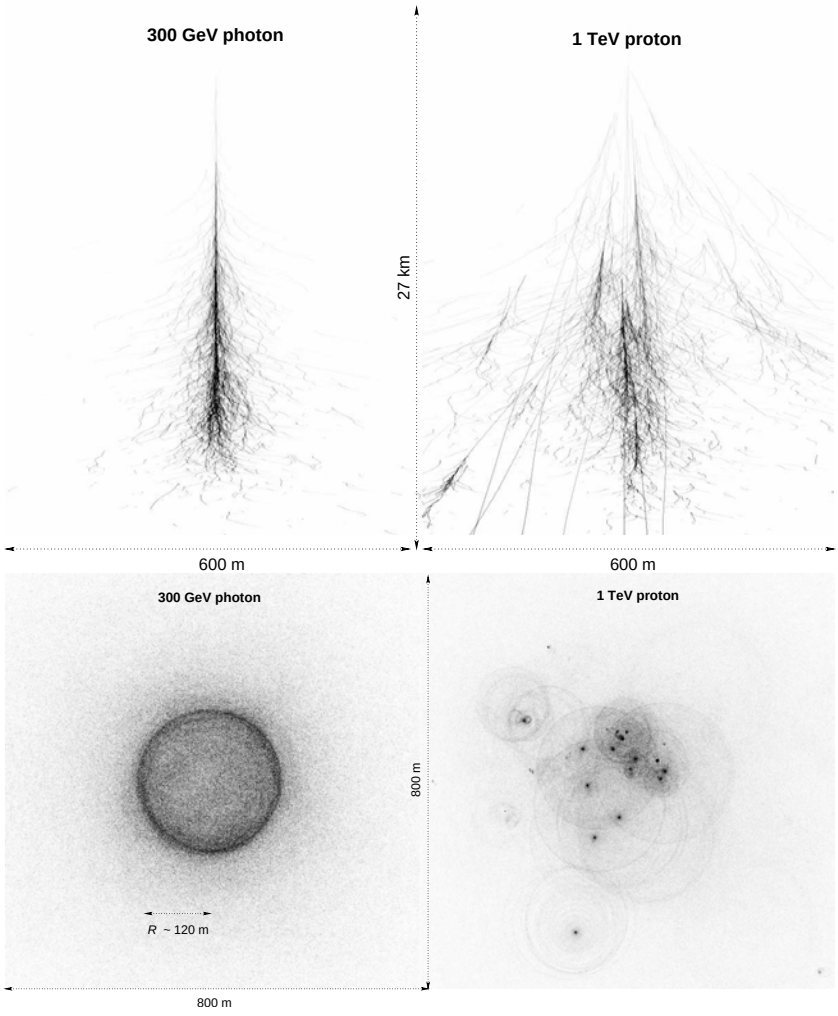


**Figure 3.10:** Top: Longitudinal air-shower development (particle trajectories) for a simulated 300 GeV gamma ray (left) and a simulated 1 TeV proton (right). Bottom: lateral Cherenkov radiation density for the same showers. Figures provided by Funk (2005) and are courtesy of K. Bernlöhr (see http://www.mpi-hd.mpg.de/hfm/∼bernlohr/HESS).

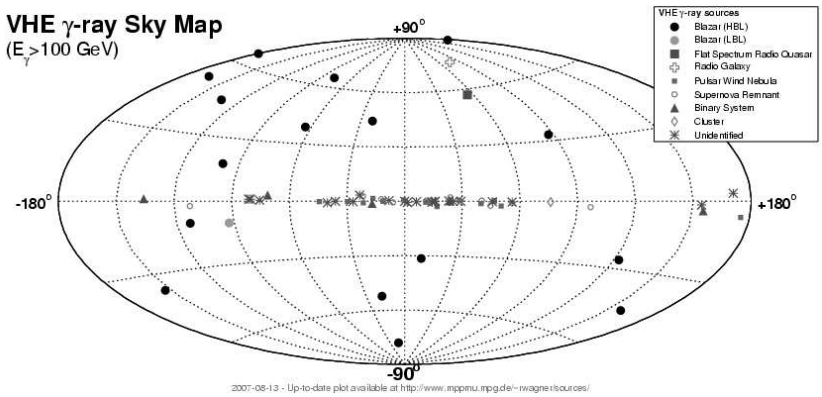


**Figure 3.11:** Catalog of TeV gamma-ray sources (as of 2007) presented in Galactic coordinates. The point sources are those detected with $E > 100$ GeV and include blazars (filled circles), flat spectrum radio quasars (large filled square), pulsar wind nebulae (small filled square), supernova remnants (open circles), radio galaxies (open plus), binary systems (filled triangle), clusters (open diamond) and unidentified sources (star). Figure taken from http://www.mppmu.mpg.de/$\sim$ rwagner/sources/index.html.

blazars Mkn 421 (Punch et al., 1992), which was the first detection of an extra-galactic very-high-energy gamma-ray source, and Mkn 501 (Quinn et al., 1996). As more telescopes have been constructed and the imaging Cherenkov technique has been improved, more and more objects have been observed in TeV energies. As of 2005, the catalog of very-high-energy gamma-ray sources contained about 30 sources (Ong, 2005) and by 2007 the number has more than doubled to over 75 sources. The catalog of TeV gamma-ray sources is shown in Figure 3.11.

Blazars Mkn 421 and Mkn 501 have been detected with high-statistical significance by the MAGIC (Major Atmospheric Gamma Imaging Cherenkov) telescope. The observations of both of these blazars show strong flux variations, between 0.5 and 2 times the flux of the Crab nebula for Mkn 421 and between 0.4 and 4 times the Crab flux for Mkn 501 (Bigongiari, 2006).

Several supernova remnants have been observed in TeV energies with ACTs, including the shell-type SNRs RX J1713.7-3946 and RX J0852.0-4622 (Aharonian et al., 2004a,b, 2005). Observations in the X-ray band from both RX J1713.7-3946 (Koyama et al., 1997; Slane et al., 1999; Uchiyama et al., 2003) and RX J0852.0-4622 (Tsunemi et al., 2000; Iyudin et al., 2005) show a smooth, featurless spectrum; an indication of synchrotron X-ray emission due to a population of TeV electrons. The same electron population might also produce gamma rays through Compton up-scattering, but the measured gamma-ray fluxes and spectra do not fully match the predicted ones (see, e.g., the analysis in Uchiyama et al., 2003), and it has

been suggested that there might also be a significant component due to hadronic interactions with the surrounding ISM (Berezhko & Volk, 2000; Enomoto et al., 2002; Aharonian, 2004; Katagiri et al., 2005). Recent X-ray observations with the Chandra telescope (Uchiyama et al., 2007) give further support for the hadronic scenario. The observations show evidence for the strong magnetic fields in the shock fronts required to accelerate cosmic rays to $10^{15}$ eV.

# Chapter 4

# Proton-Proton Interaction Modeling

The first attempts at modeling cosmic gamma-ray emission due to $\pi^0$ decays were made in the 1960's by Ginzburg (1967), Hayakawa (1969) and others. The observational data available at the time was limited and of poor quality which severely limited their accuracy. Further work was made in the late 1970's and the 1980's by Strong et al. (1978), Stephens & Badhwar (1981), Dermer (1986a) and Stecker (1989). At this point, accelerator-based experiments provided high-statistics data on pion production from proton-proton interactions and this laid the foundation for cosmic gamma-ray emission models. Because particle accelerators were not powerful enough, there was a lack of data in the very high-energy regime and all models relied on the Feynman-scaling hypothesis (described in more detail in Section 4.2) to extend the available accelerator data to higher energies. These models also assumed the non-diffractive inelastic proton-proton cross section to be constant, about 25 mb, at higher energies, when in fact it is known to rise with energy.

Detailed studies of $pp$ and $\bar{p}p$ interactions at cms energies above 10 GeV have shown that the Feynman-scaling hypothesis is not valid. Still models used in astrophysical context for $\pi^0$ production from proton-proton interactions assume Feynman scaling to hold. This was noted by Kamae et al. (2005). They also noted a few other short-comings, such as the use of the constant non-diffractive inelastic proton-proton cross section and the diffractive process not being included. In the diffractive interaction, either or both of the two protons transition to an excited state, which then decays to a nucleon and pions. Including the above, the gamma-ray spectrum is expected to change in the following manner: 1) the diffractive process adds either high-energy or low-energy gamma rays, depending on which of the protons is excited, and 2) the violation of scaling and a rising inelastic cross section increase the overall gamma-ray yield.

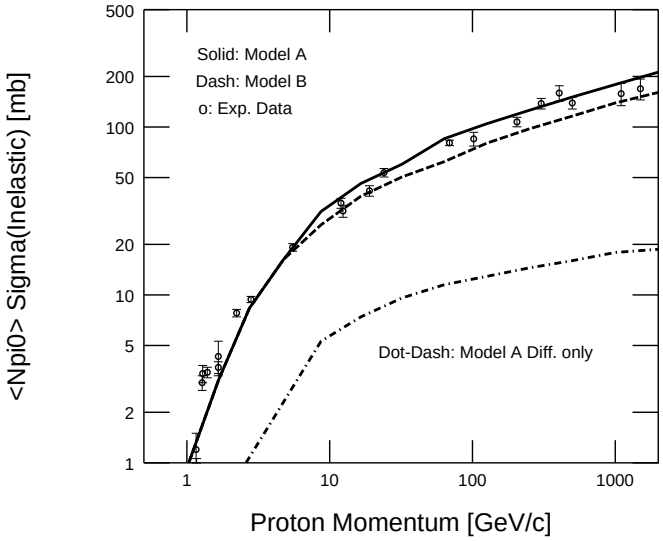


**Figure 4.1:** $\pi^0$ inclusive cross section, $\langle n_{\pi^0} \rangle \sigma_{\text{inel}}$, according to the model of Kamae et al. (2005). Model A (solid line) includes non-diffractive and diffractive interaction, and model B (dashed line) is their reference model where Feynman scaling is not violated. Experimental data (open circles) are from Dermer (1986b). The models are clearly not in agreement with experimental data points for proton momenta of a few GeV.

A model for the proton-proton interaction with the above features of the inelastic interaction included was proposed by Kamae et al. (2005). It was primarily aimed at studying the Galactic ridge and concerned proton kinetic energies well above 1 GeV. It is not accurate near the pion production threshold as seen in Figure 4.1, where the $\pi^0$ inclusive cross section, $\langle n_{\pi^0} \rangle \sigma_{\text{inel}}$, is plotted versus the proton laboratory momentum. To improve accuracy for lower energies, the proton-proton interaction model has been adjusted (Kamae et al., 2006) with the addition of two baryon resonances, $\Delta(1232)$ and res(1600). The term baryon resonance is used here to represent both nucleon resonances (isospin 1/2) and $\Delta$ resonances (isospin 3/2). The $\Delta(1232)$ represents a physical resonance, with a mass of 1232 MeV/c$^2$ and width of about 120 MeV/c$^2$, and the res(1600) represents several resonances with masses around 1600 MeV/c$^2$. This addition increases the average $\pi^0$ multiplicity for proton momenta about 2 GeV/c.

The model for the proton-proton interaction presented here has been divided into four different parts; non-diffractive interaction, diffractive interaction, and the

two baryon resonances, corresponding to the interaction processes mentioned above. The Pythia framework (version 6.2; Sjöstrand et al., 2001a) for simulations of hadronic interactions, is used to simulate the non-diffractive interaction at high proton kinetic energies, together with the scaling models by Badhwar et al. (1977) and Stephens & Badhwar (1981) as parameterized by Blattnig et al. (2000) at low energies. Where the transition is taken will be explained later. Modeling of the diffractive process is based on the formula given in Goulianos (1983, 1995) and Goulianos & Montanha (1999). The baryon resonances have been modeled under the assumption of one pion exchange model. Each of these parts will be described in detail in the following sections.

## 4.1 Experimental Data from a Historical Perspective

Early proton accelerators, such as the Bevatron at the Lawrence Berkeley National Laboratory and the Cosmotron at the Brookhaven National Laboratory, were all used in fixed target experiments. They were synchrotrons that could accelerate protons to laboratory energies of about 5 GeV. The Bevatron was specifically designed for the search of the antiproton, which was discovered with it in 1955 (Chamberlain et al., 1955).[1]

With these early machines, the total proton-proton cross section was measured up to a few GeV in laboratory energy. The data indicated a total cross section levelling off to a constant value of about 40 mb. In the light of this asymptotic behavior, the hypothesis of Feynman scaling was proposed (Feynman, 1969). The concept of Feynman scaling is discussed in the next section.

In 1971, the Intersecting Storage Rings (ISR) were built at CERN. This was the world's first proton-proton collider machine. With the ISR, the center-of-mass energy was increased to 63 GeV and the previously assumed asymptotic behavior was found to be incorrect. The total cross section was no longer constant but increased as

$$\sigma_{\mathrm{tot}} \propto \ln^2 s \tag{4.1}$$

and the ratio between the elastic and total cross sections was constant

$$\frac{\sigma_{\mathrm{el}}}{\sigma_{\mathrm{tot}}} \simeq 0.175 \tag{4.2}$$

in the high-energy regime (Carlson, 1986).

With the CERN antiproton collider, center-of-mass energies reached 900 GeV and history repeated itself. The asymptotic conditions had to be given up again. The ratio of elastic to total cross sections, $\sigma_{\mathrm{el}}/\sigma_{\mathrm{tot}}$, was no longer constant but increased with energy. The $\ln^2 s$ dependence of the total cross section was confirmed up to $\sqrt{s} = 900$ GeV. It also became clear that the difference in cross sections

[1] O. Chamberlain and E. Sergè were awarded the Nobel prize in 1959 for the discovery.

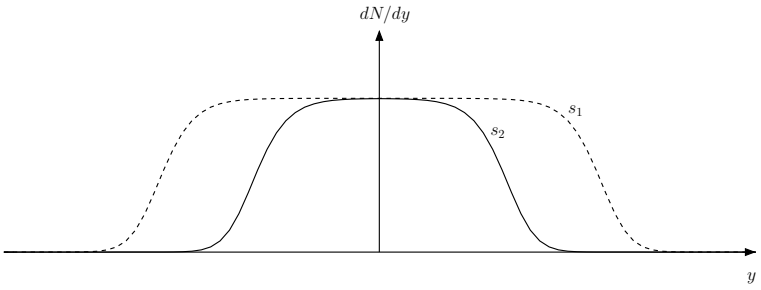


**Figure 4.2:** Rapidity distributions, $dN/dy$, in the cms for two different cms energies squared, $s_1$ and $s_2$, such that $s_1 > s_2$, as predicted by the Feynman-scaling hypothesis. As the cms energy is increased the distribution maximum stays constant and the plateau grows along $y$, proportional to $\ln(s)$.

between proton-proton and proton-antiproton approaches zero, as was expected from models.

## 4.2 Feynman-Scaling Hypothesis

In the late 1960's, Feynman (1969) proposed a scaling hypothesis for the high-energy regime. Generally, a scaling law is such that a certain quantity only depends on the scaling variable or variables. In Feynman scaling, which was suggested to hold for non-diffractive interactions at high energies (proton kinetic energy above 10 GeV), the scaling law states that the invariant cross sections

$$E\frac{d^3\sigma}{dp^3} = f(p_t, x_\parallel^*) \tag{4.3}$$

depend only on the Feynman scaling variable $x_\parallel^*$ (star indicates center-of-mass variables), defined as (Perl, 1974)

$$x_\parallel^* = \frac{2p_\parallel^*}{\sqrt{s}} \tag{4.4}$$

and the transverse momentum $p_t$. Here, $p_\parallel^*$ is the momentum component parallel to the relative motion between target and projectile in the cms and $\sqrt{s}$ is the total cms energy. The parton model by Feynman (1972) and its extension the quark-parton model, were the first physical models built upon the Feynman-scaling hypothesis.

With the detailed studies of $pp$ and $\bar{p}p$ interactions around 1980 it became clear that the Feynman scaling hypothesis is not valid (Alpgard et al., 1983; Alner et al., 1984; Breakstone et al., 1984). Strong evidence for the violation of Feynman scaling

can be seen in the rapidity distribution $dN/dy$, where $N$ is the particle multiplicity and $y$ is the rapidity defined as

$$y = \ln \frac{E + p_{\parallel}}{E - p_{\parallel}} \tag{4.5}$$

where $p_{\parallel}$ is the longitudinal momentum. The Feynman scaling law predicts the rapidity density $dN/dy$ to have an energy-independent plateau which has a length increasing logarithmically with energy, as shown in Figure 4.2. In reality $dN/dy$ also rises logarithmically

$$\frac{dN}{dy} \sim \ln(s) \tag{4.6}$$

This causes the multiplicity to increase as $\ln^2(s)$ and Feynman scaling is violated. Figure 4.3 shows experimental data for the pseudo-rapidity distributions at beam energies $\sqrt{s} = 53$ (from the ISR collider), 200, 546 and 900 GeV measured by the UA5 collaboration with the CERN SPS collider (Alner et al., 1986). The data clearly show the increase in multiplicity with energy.

## 4.3 Inelastic pp Cross Section

The total and elastic cross sections for $pp$ interactions have been accurately measured with accelerator based experiments (see compilation by Hagiwara et al., 2002). Figure 4.4 shows the experimental data points[2] for the total and the elastic cross sections for $pp$ as well as for $\bar{p}p$ at high momenta. The data clearly show a logarithmic rise of the total and the elastic cross sections. The figure also shows the model fits to the total and elastic cross sections used in this work.

The inelastic $pp$ cross section is, by definition, given by

$$\sigma_{\text{tot}} = \sigma_{\text{el}} + \sigma_{\text{inel}} \tag{4.7}$$

The empirical inelastic cross section is then defined as the difference between the model fits for the total and elastic cross sections. Errors for the empirical inelastic cross section are about 20% for proton kinetic energies below 3 GeV and about 10% above 3 GeV. The inelastic cross section is the sum of the cross sections of the four components

$$\sigma_{\text{inel}} = \sigma_{\text{nd}} + \sigma_{\text{diff}} + \sigma_{\Delta(1232)} + \sigma_{\text{res}(1600)} \tag{4.8}$$

and the empirical inelastic cross section constrains the non-diffractive, diffractive and resonance components. There is an uncertainty in how the total inelastic cross section should be distributed between the four components for $T_p < 20$ GeV, but as long as one makes sure that the total inelastic cross section is not exceeded and that the resulting total inclusive cross section for secondary particles agrees with

[2] Experimental data for the total and elastic cross sections are available at http://pdg.lbl.gov/2002/contentsplots.html

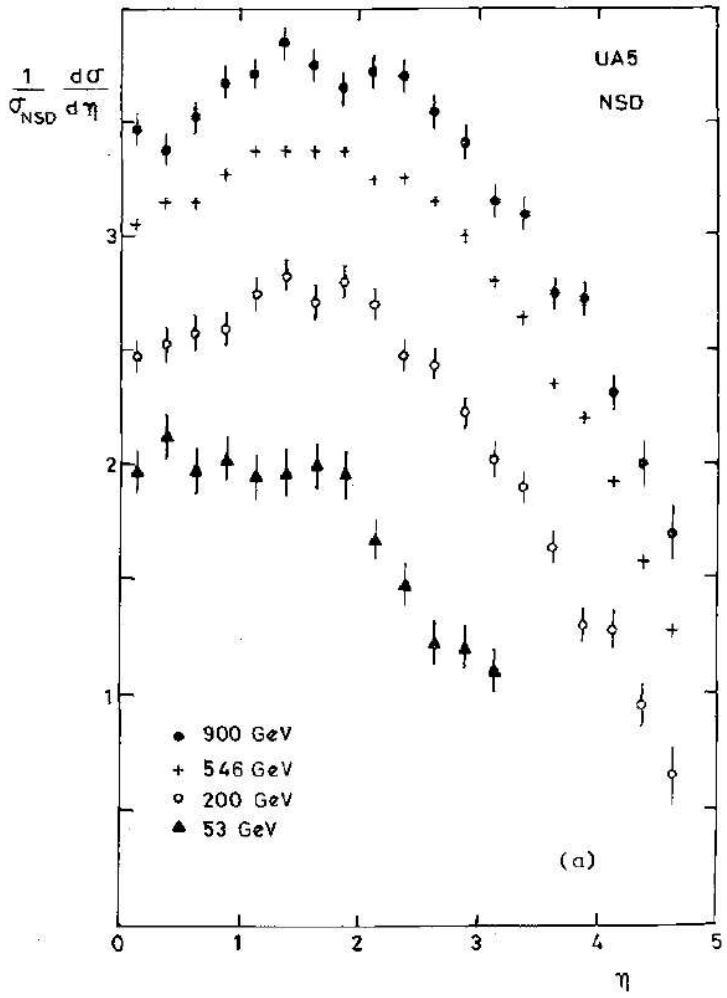


**Figure 4.3:** Experimental pseudorapidity distributions, $(1/\sigma_{\rm NSD})d\sigma/d\eta$, for non-single diffractive (NSD) events measured by the UA5 collaboration at the CERN-SPS collider for beam energies $\sqrt{s} = 53, 200, 546$ and 900 GeV. The data points for $\sqrt{s} = 53$ GeV are from the ISR collider. As the cms energy is increased the multiplicity increases proportional to $\ln^2(s)$. Figure taken from Alner et al. (1986).

experimental data, this uncertainty does not change the secondary particle fluxes to any significant amount.

The total and elastic cross sections are known to rise with increasing proton momentum (Eggert et al., 1975; Baksay et al., 1988; Amaldi et al., 1978). In the high-momentum region, the ratio $\sigma_{\rm el}/\sigma_{\rm tot}$ is approximately constant and the total inelastic cross section also increases. The increase is shared by the non-diffractive and diffractive components.

The total diffractive cross section is

$$\sigma_{\rm diff} = 2\sigma_{sd} + \sigma_{dd} \tag{4.9}$$

where single-diffraction cross section follows that of Goulianos (1983) and the double-diffraction cross section is taken from Affolder et al. (2001) with a suppression for lower energies according to Givernaud et al. (1979), as described in section 4.6.

The cross sections for the two baryon resonances follow the modeling of Stecker (1970), but were modified to have less prominent tails toward higher energies, since the diffraction interaction process sets in at proton kinetic energy of about 2 GeV. Before the two baryon resonances were added, the inelastic non-diffractive cross section was calculated from equation 4.7 and

$$\sigma_{\rm inel} = \sigma_{\rm nd} + \sigma_{\rm diff} \tag{4.10}$$

It was then adjusted with $\sigma_{\Delta(1232)}$ and $\sigma_{\rm res(1600)}$ while making sure the total empirical inelastic cross section was not exceeded.

Given in eqs. 4.11, 4.12, 4.13 and 4.14 below are algebraic forms for the above mentioned cross sections, which are also shown in Figure 4.4. The algebraic forms were attained by piece-wise fitting of the cross sections.

$$\sigma^{pp}_{\rm nd}(x) = \begin{cases} 0 & p_p < 1 \\ a_0(x/a_1)^{1.2}(a_3 + a_4x^2 + a_5x^3 + \\ \quad +a_6\exp(-a_7(x+a_8)^2)) & 1 \le p_p \le 1.3 \\ (b_0|a_2 - x| + b_1|a_1 - x|)/(a_2 - a_1) & 1.3 \le p_p \le 2.4 \\ a_3 + a_4x^2 + a_5x^3 + a_6\exp(-a_7(x+a_8)^2) & 2.4 \le p_p \le 10 \\ c_0 + c_1x + c_2x^2 & p_p > 10 \end{cases} \tag{4.11}$$

$$\sigma^{pp}_{\rm diff}(x) = \begin{cases} 0 & p_p < 2.25 \\ \sqrt{(x-d_0)/d_1}(d_2 + d_3\log(d_4(x-0.25)) + \\ \quad +d_5x^2 - d_6x^3) & 2.25 \le p_p \le 3.2 \\ d_2 + d_3\log(d_4(x-0.25)) + d_5x^2 - d_6x^3 & 3.2 \le p_p \le 100 \\ e_0 + e_1x & p_p > 100 \end{cases} \tag{4.12}$$

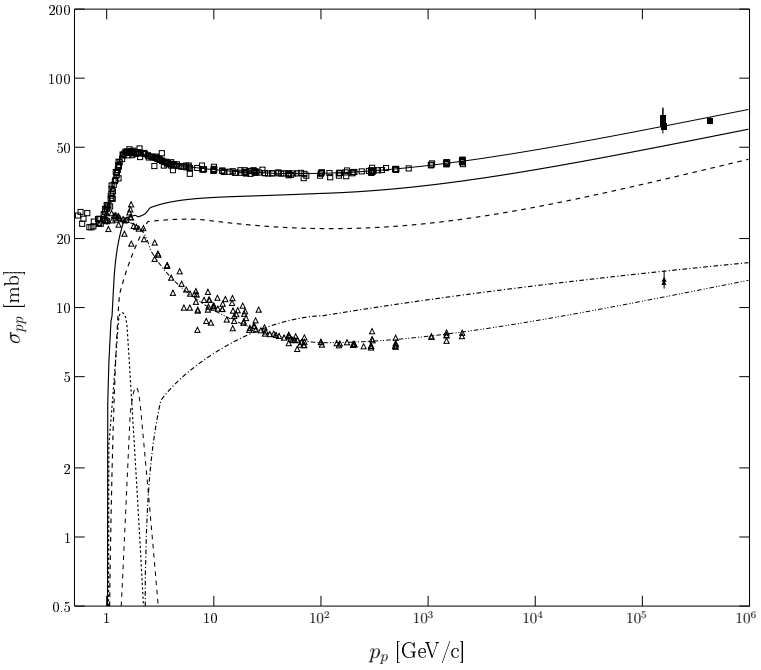


**Figure 4.4:** Experimental $pp$ cross sections, total (open squares) and elastic (open triangles), as functions of proton laboratory momentum, and our model fits to them, total (thin solid) and elastic (thin dot-dot-dashed). Error bars have been omitted for clarity in the figure. Included are also the experimental $\bar{p}p$ total (filled squares) and elastic (filled triangles) cross sections at high proton momenta. The total inelastic (thick solid) is taken as the difference between total and elastic cross sections and is also the sum of the four components: non-diffractive (dashed), diffractive (dot-dashed), $\Delta(1232)$ (dotted) and res(1600) (thin dashed).

**Table 4.1:** Coefficients for the inelastic proton-proton cross sections

| $a$ | $b$ | $c$ | $d$ |
|---|---|---|---|
| $a_0 = 0.57$ | $b_0 = 11.34$ | $c_0 = 28.5$ | $d_0 = 0.3522$ |
| $a_1 = 0.1176$ | $b_1 = 23.72$ | $c_1 = -6.133$ | $d_0 = 0.1530$ |
| $a_2 = 0.3829$ | | $c_2 = 1.464$ | $d_2 = 1.498$ |
| $a_3 = 23.10$ | | | $d_3 = 2.0$ |
| $a_4 = 6.454$ | | | $d_4 = 30.0$ |
| $a_5 = -5.764$ | | | $d_5 = 3.155$ |
| $a_6 = -23.63$ | | | $d_6 = 1.042$ |
| $a_7 = 94.75$ | | | |
| $a_8 = 0.02667$ | | | |
| $e$ | $f$ | $g$ | |
| $e_0 = 5.922$ | $f_0 = 0.08341$ | $g_0 = 0.005547$ | |
| $e_1 = 1.632$ | $f_1 = 9.5$ | $g_1 = 4.5$ | |
| | $f_2 = -5.5$ | $g_2 = -7.0$ | |
| | $f_3 = 1.68$ | $g_3 = 2.1$ | |
| | $f_4 = 3134$ | $g_4 = 14089$ | |

$$\sigma^{pp}_{\Delta(1232)}(x) = \begin{cases} 0 & E_p < 1.4 \\ f_0 E_p^{10} & 1.4 \leq E_p \leq 1.6 \\ f_1 \exp\left(-f_2(E_p - f_3)^2\right) & 1.6 \leq E_p \leq 1.8 \\ f_4 E_p^{-10} & 1.8 \leq E_p \leq 10 \\ 0 & E_p > 10 \end{cases} \tag{4.13}$$

$$\sigma^{pp}_{\mathrm{res}(1600)}(x) = \begin{cases} 0 & E_p < 1.6 \\ g_0 E_p^{14} & 1.6 \leq E_p \leq 1.9 \\ g_1 \exp\left(-g_2 * (E_p - g_3)^2\right) & 1.9 \leq E_p \leq 2.3 \\ g_4 E_p^{-6} & 2.3 \leq E_p \leq 20 \\ 0 & E_p > 20 \end{cases} \tag{4.14}$$

with $x = \log(p_p)$ and the proton momentum, $E_p$, in units of GeV. The coefficients are listed in Table 4.1.

## 4.4 Non-Diffractive Interaction

In the 1970's, the perturbative theory of quantum chromodynamics (QCD) arose as the fundamental theory describing hadronic interactions and replaced the quark-parton model (see, e.g., Altarelli & Parisi, 1977). QCD is, just like quantum electro-

dynamics (QED), a gauge theory[3] in which interactions are mediated by massless gauge bosons of spin-1 coupling to conserved charges. In the case of QED, the gauge boson is the photon which couples to electric charge. In QCD there are several gauge bosons, known as gluons, coupling to the color charge carried by both quarks and gluons. The theory of QCD will not be explained in further detail here, instead the reader is referred to other excellent textbooks on the subject (see, e.g., Dissertori et al., 2003; Greiner et al., 2002).

### 4.4.1 Pythia

The Pythia simulation framework has become a widespread tool for the simulation of hadronic interactions and calculation of complex final states based on the perturbative QCD theory. The first steps toward such a framework was taken in the late 1970's, when Andersson and collaborators at the University of Lund built a numerical simulation code aimed at $e^+e^-$ collider experiments, which became known as the Lund model (Andersson et al., 1979, 1980; Andersson, 1998). The Lund model was extended to $pp$ and $p\bar{p}$ interactions at high energies resulting in Pythia.

In QCD, Feynman scaling is violated in hard parton-parton interactions and many other parton diagrams, such as the multiple interaction terms. The latest versions of Pythia include all these features (Sjöstrand et al., 2001a).

In this work Pythia (version 6.2), with the parameter set labeled "tune A" (Field, 2002; Sjöstrand & Skands, 2004), from the CDF collaboration at Fermilab (see Appendix B) has been used to simulate events for the non-diffractive part of the proton-proton interaction. Due to inaccuracy of QCD at lower energies this had to be complemented with the scaling models by Badhwar et al. (1977) and Stephens & Badhwar (1981) in the parametric form by Blattnig et al. (2000) in the low-energy regime. Already at 50 GeV the inaccuracy is noticeable and because events are generated for proton kinetic energies in steps of $\sqrt{2}$ (see section 5.1), the transition between Pythia and the scaling models is taken at 52.6 GeV.

Late year 2006 a new version of Pythia was released. Among many changes, this release has been further tuned to the latest available high-energy data from the CDF collaboration. The current parameter set used by the CDF collaboration is labeled "tune DWT" (Field, 2002). Pythia version 6.4 provides subroutines for the selection of parameter sets, which elimiate the need to set parameters individually. The fortran code for proton-proton interactions was updated and compiled with version 6.4. The version 6.2 runs were repeated with version 6.4 using both the A and DWT parameter sets for comparison of results. Four extra runs for CDF energies were made using "tune DWT": proton kinetic energies $T_p = 724$, 1023, 1447 and 2047 TeV.

Runs of version 6.4 with parameter set A are consistent with the previous results as expected. Parameter set DWT was run to investigate the improvements over

[3]Named so because they feature the symmetry of gauge invariance.

"tune A" for the highest CDF energies. When comparing results with experimental data it was noticed that the DWT runs did not reproduce ISR data; for example the average transverse momentum, $\langle p_t \rangle$ of charged particles was about 0.1 GeV/c larger than that of experimental data. It was suggested that the culprit is the primordial $kT$ parameter, which is set to be independent of scattering subsystem and the cms energy (T. Sjöstrand 2007, private communications). In "tune DWT", primordial $kT$ is set to 2.1 GeV, compared to 1.0 GeV in "tune A". The parameter was manually reset to 1.0 GeV and fair agreement with ISR data was recovered. As expected, "tune DWT" reproduces CDF data better than "tune A". The average transverse momentum will be discussed in more detail later in this chapter.

### 4.4.2 Low-Energy Events in Non-Diffractive Interactions

Inclusive production cross sections, i.e. interactions on the form

$$p + p \rightarrow \pi + X \tag{4.15}$$

where $X$ represents any reachable state, for neutral and charged pions in proton-proton interactions have been parameterized by Blattnig et al. (2000). They give both the energy differential cross sections, $(d\sigma/dE)_{\rm lab}$, (spectral distributions) and the total cross sections, $\sigma_\pi$, in algebraic form as functions of the kinetic energy in the lab frame of the incident proton, $T_p$, and the kinetic energy of the produced pion, $T_\pi$, also in the lab frame. For charged pions, they calculated the spectral distributions by integrating over the Lorentz invariant differential cross sections (LIDCS) from Badhwar et al. (1977), and for neutral pions they used cross sections from Stephens & Badhwar (1981) as well as their own calculation of the invariant cross section (see equation 7 in Blattnig et al., 2000).

A very important aspect when using two different methods for the non-diffractive simulations is the transition between them. Simulations with Pythia were used as guidance for the parametric model. For the case of gamma rays, two different parameterizations are given for the spectral distribution. Here the one based on the Stephens & Badhwar (1981) LIDCS is referred to as version A and the one based on LIDCS by Blattnig et al. (2000) as version B. Figure 4.5 shows the gamma-ray spectrum calculated using both of these two spectral distributions for proton kinetic energy $T_p = 62.5$ GeV and compared with the gamma-ray spectrum from Pythia simulations at the same proton kinetic energy. The parameterizations given are valid from 0.3 GeV up to 50 GeV and it is noted that this is above the validity region, resulting in a difference of about 10% for version A. It over-estimates the gamma-ray spectrum for energies below 1 GeV and under-estimates it above 1 GeV. Version B reproduces well the results from Pythia for gamma-ray energies below about 0.2 GeV. For higher energies it does not match at all. To achieve better agreement with Pythia overall, a mix of the two versions has been chosen, with 85% A and 15% B. This is shown in the lower panel in Figure 4.5. The peak is slightly lower than that from Pythia but overall the error between the two is smaller than for just version A.

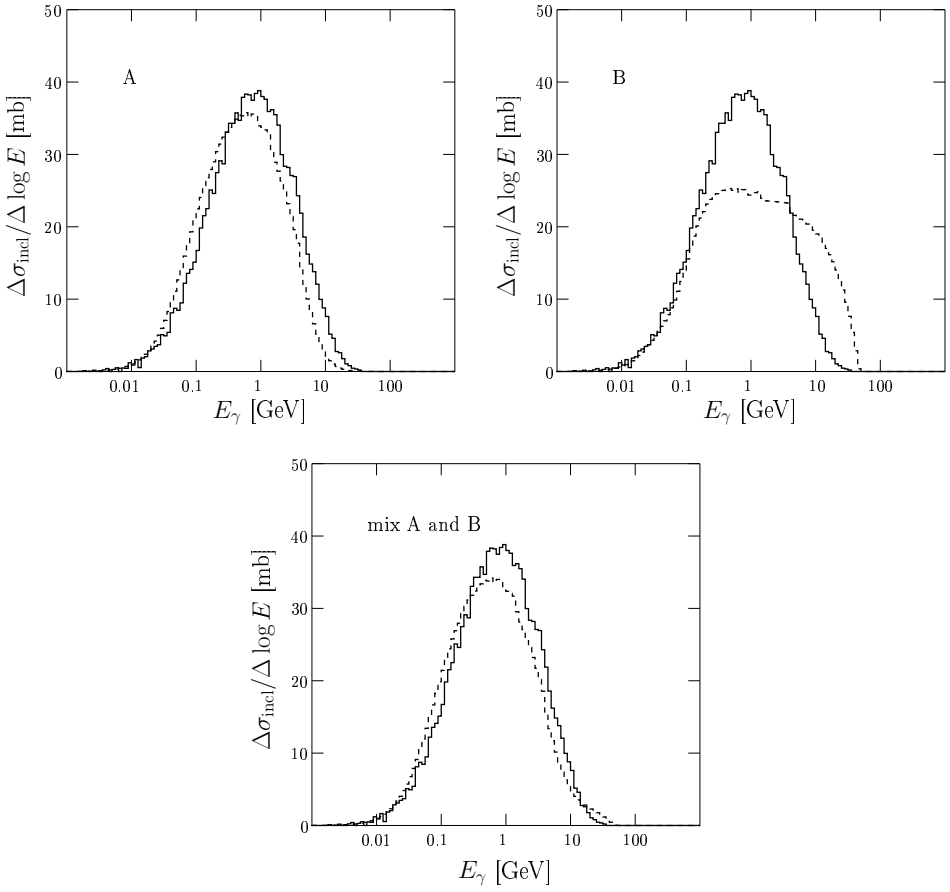


**Figure 4.5:** Gamma-ray spectra as functions of energy calculated from the two different parameterizations of the $\pi^0$ spectral distribution given in Blattnig et al. (2000). Solid histogram is that of Pythia for proton kinetic energy $T_p = 62.5$ GeV and the dotted histogram is that calculated using the parametric model at the same energy. Upper-left panel is for parameterization version A (based on LIDCS given in Badhwar et al., 1977) and upper-right is that of version B (based on LIDCS given in Blattnig et al., 2000)). Lower panel is a mix of the two, 85% of A and 15% of B. The difference of about 10% is partly due to the use of the parametric model above its validity region, 0.3 to 50 GeV.

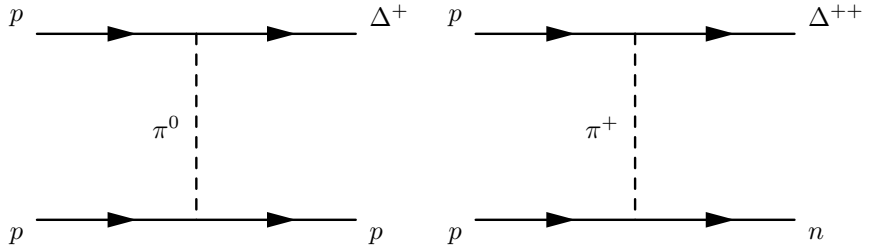


**Figure 4.6:** Feynman diagrams illustrating the one-pion exchange hypothesis. One of the two interacting protons is excited to a $\Delta(1232)$ resonance. Charge conservation limits the excitation to $\Delta^+$ and $\Delta^{++}$.

## 4.5 Resonance Excitation Processes

In an inelastic pp interaction involving proton energies near the pion production threshold there is a possibility that either of the involved protons is excited to a resonant state. This resonant state can be either a nucleon or $\Delta$ resonance, collectivly named baryon resonances in this work. The interaction involves exchange of quantum numbers and can be modeled using the one-pion exchange hypothesis.

The most prominent of these resonant states is the $\Delta(1232)$ ($\Delta^+$ and $\Delta^{++}$ because of charge conservation), and it decays predominantly (99% branching ratio) to a nucleon and a pion. The res(1600) resonance decays to a nucleon and two pions. The average pion multiplicity near the pion production threshold is increased with the addition of these resonances.

In 1970, Stecker proposed a model (Stecker, 1970) for gamma-ray production through $\pi^0$ decays in which pions are produced only from the decay of $\Delta(1232)$ for proton kinetic energies below 2.2 GeV and a fireball process for higher energies. Stephens & Badhwar (1981), on the other hand, suggested a scaling model. Both of these models were checked against experimental data on the $\pi^0$ kinetic energy distributions in the cms by Dermer (1986a). Dermer concluded that the resonance production model gave better reproduction of the data for $T_p < 3$ GeV and proposed a connected model of the two.

In this work, the calculation of final states from baryon resonances is based on the Stecker model and the one-pion exchange hypothesis assumption. The Feynman diagrams are shown in Figure 4.6. The expected pion multiplicity ratios

$$n(\pi^+) : n(\pi^0) : n(\pi^-)$$

for $\Delta(1232)$ decays are, from considerations of isospin Clebsch-Gordan coefficients, 0.73:0.27:0. The $\Delta(1232)$ resonance alone is not enough to reproduce the experimental data and a higher-mass resonance, res(1600), is introduced to fill in the discrepancy. The res(1600) is not a physical resonant state, but rather a representation of several states with masses around 1600 MeV/c$^2$. It is assumed to decay to a nucleon and two pions. The pion multiplicity ratios for the res(1600) are 1.0:0.8:0.2, again from considerations of isospin Clebsch-Gordan coefficients. There

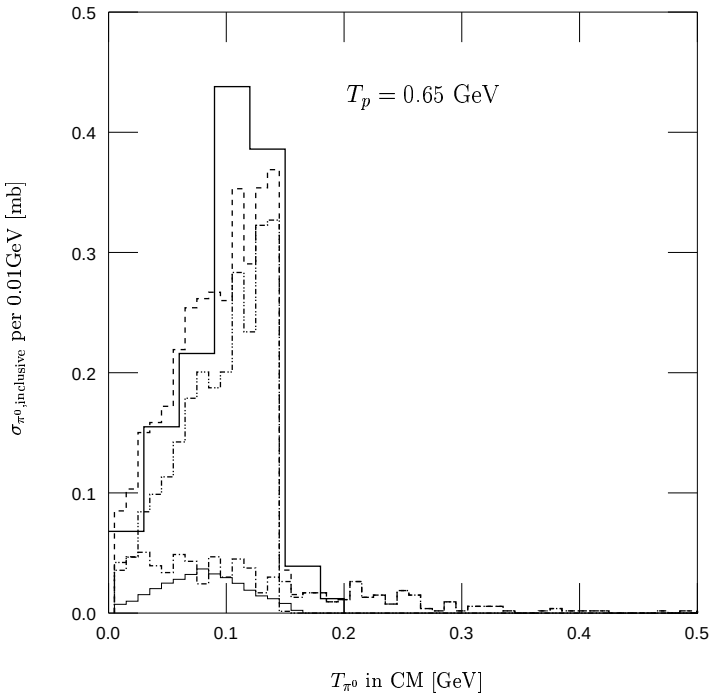


**Figure 4.7:** Experimental (thick solid; Guzhavin et al., 1964), compiled by Dermer (1986a), and simulated $\pi^0$ kinetic energy distributions in the cms for $T_p = 0.65$ GeV. The simulated data are: sum of all components (dashed), non-diffractive component (dash-dot), $\Delta(1232)$ contribution (dotted) and res(1600) (thin solid). The experimental data are old with large error bars up to 25%.

are no experimental data on the two-pion isospin available to verify this assumption. It is seen that $\pi^+$ is favored over $\pi^0$ and that $\pi^-$ production is strongly suppressed for both of these states. In the simulations, pions are produced with $(\theta^*, \phi^*)$ taken randomly on the unit sphere, i.e. phase space element $\sin\theta d\theta d\phi$, in the cms of the resonance, while conserving linear momentum and without any correlation between individual pions created within the same event. The latter is justified in astronomical environments because the probability of detecting two gamma rays from the same interaction event is almost zero.

The $\pi^0$ kinetic energy distributions in the cms from simulations have been compared with experimental data at proton energies $T_p = 0.65$, 0.97 and 2.0 GeV, shown in Figures 4.7, 4.8 and 4.9. The experimental data is well reproduced at $T_p = 0.65$ GeV and as one moves to higher proton kinetic energy the peak of the simulated distributions is shifted toward zero. It must be stated that the experimental data are old with large error bars up to 25%.

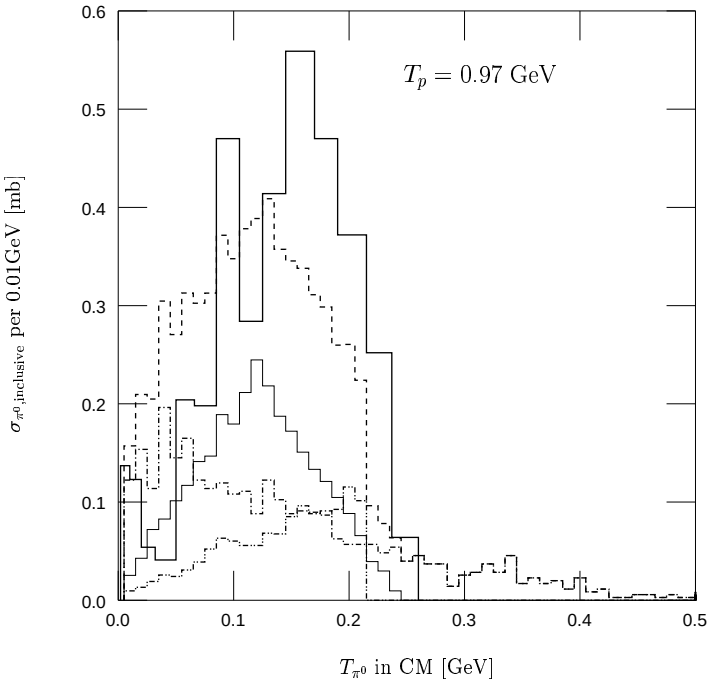


**Figure 4.8:** Experimental (thick solid; Bugg et al., 1964), compiled by Dermer (1986a), and simulated $\pi^0$ kinetic energy distributions in the cms for $T_p = 0.97$ GeV. The simulated data are: sum of all components (dashed), non-diffractive component (dash-dot), $\Delta(1232)$ contribution (dotted) and res(1600) (thin solid). The experimental data are old with large error bars up to 25%.

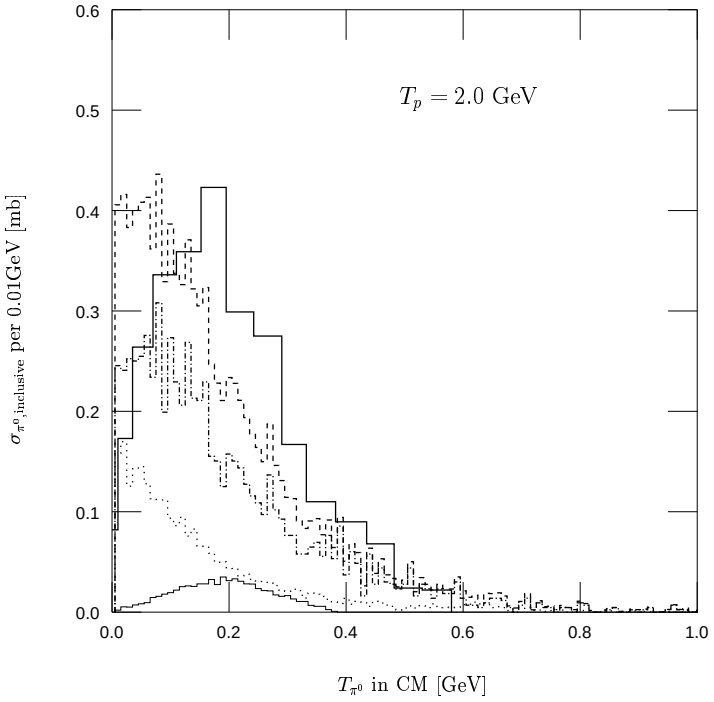


**Figure 4.9:** Experimental (thick solid; Fickinger et al., 1962; Pickup et al., 1962), compiled by Dermer (1986a), and simulated $\pi^0$ kinetic energy distributions in the cms for $T_p = 2.0$ GeV. The simulated data are: sum of all components (dashed), non-diffractive component (dash-dot), $\Delta(1232)$ contribution (dotted) and res(1600) (thin solid). The experimental data are old with large error bars up to 25%.

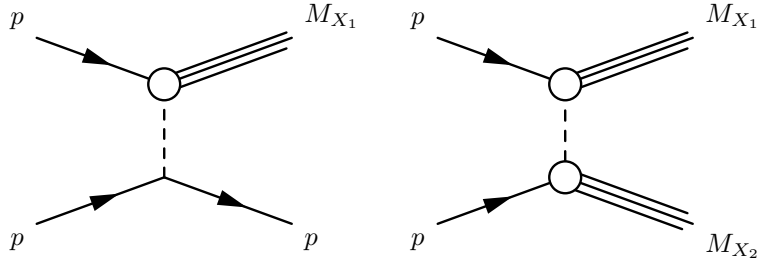


**Figure 4.10:** Feynman diagram illustrating single diffraction formation of mass state $M_{X_1}$ (left) and double diffraction (right) formation of mass states $M_{X_1}$ and $M_{X_2}$ in interactions where no quantum numbers are exchanged.

## 4.6 Diffractive Interaction

The diffractive interaction refers to inelastic interactions in which either or both of the projectile and target proton is excited to a higher-mass state. This state can be either a discrete nucleon resonance or a continuum. If only one proton is excited one has single diffraction and double diffraction if both protons are excited. In the case of single diffraction one differentiates projectile diffraction from target diffraction depending on which of the projectile and target that is excited.

The inelastic diffractive interaction between nucleons was proposed in the late 1950's and early 1960's by, among others, Good & Walker (1960). They suggested the possibility for a particle of mass $m$ to be excited to a state with mass $M_X$ in an interaction with another particle where the interaction would involve no exchange of quantum numbers. The single diffraction interaction is illustrated by the Feynman diagram in Figure 4.10. The mass $M_X$ is limited by the coherence condition

$$\frac{M_X^2}{s} \leq \frac{1}{m_p R} \tag{4.16}$$

where $s$ is the cms energy squared and $R$ is the interaction radius. For the coherence condition it is required that the non-excited nucleon does not emit any pions and the mass limit is obtained with $R = 1/m_\pi$ (Geich-Gimbel, 1987)

$$\frac{M_X^2}{s} \leq \frac{m_\pi}{m_p} \simeq 0.15 \tag{4.17}$$

Two different models were put forward for the decay of the mass state $M_X$; an isotropic fireball process and a $p_t$ limited, cylindrical phase space (CPS) model. The pseudo-rapidity distributions for the two decay models are illustrated in Figure 4.11 for a mass state $M_X \simeq 10$ GeV/c$^2$ which is produced with with a pseudo rapidity $\eta \simeq \ln(\sqrt{s}/M_X)$. The distribution for the isotropic model is approximately a Gaussian with a mass independent width of $< 1$ unit. In the CPS model the width of the distribution is approximately $\ln(M_X/\mu)$ where $\mu^2 = p_t^2 + m_\pi^2$.

With early data from the ISR ($\sqrt{s} < 60$ GeV) it was not possible to distinguish between the two models. Further data from the CERN SPS and other collider

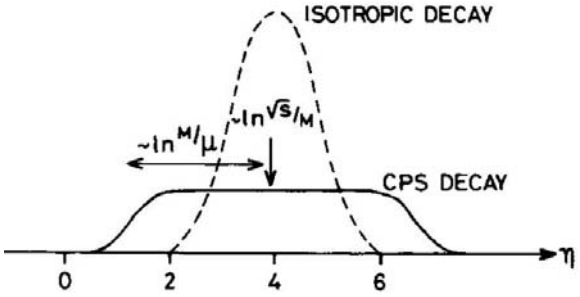


**Figure 4.11:** Illustration of the spread of rapidities from the decay of the mass state $M_X \simeq 10$ GeV/c$^2$ produced in a single diffraction event. The y axis without scale is $dN/d\eta$. The state is produced with a pseudo rapitity $\eta \simeq \ln(\sqrt{s}/M_X)$. The decay can be either isotropic (dashed line) or with limited $p_t$ (solid line). In the isotropic decay the rapidity distribution is approximately Gaussian with a width $< 1$ unit, independent of $M_X$. In a $p_t$ limited decay (CPS; cylindrical phase space) the width of the distribution is approximately $\ln(M_X/\mu)$ where $\mu^2 = p_t^2 + m_\pi^2$. Figure taken from Alner et al. (1987).

experiments favor the $p_t$ limited decay model. The isotropic model has no support in QCD and cannot explain structures observed at high cms energies for large masses $M_X$.

Both single and double diffraction were observed in the mid 1960's (Alberi & Goggi, 1981). This theory is adopted as the basis for simulations in this work, in which a proton is excited to a mass state $M_X$ and subsequently dissociates to a nucleon and one or more pions (the multiplicity depends on the incident proton energy). The difference in mass, $M_X - m_p$, is smaller than the total cms energy, $\sqrt{s}$, and for simplification the momentum transfer, $q$, is assumed to be small and parallel to the direction of the incident proton

$$q_{\parallel} = \frac{M_X^2 - m_p^2}{2p_p} \tag{4.18}$$

where $p_p$ is the momentum of the incident proton and $m_p$ is the proton mass.

The diffractive interaction is simulated in the following way[4]. Step one is to select from projectile, target or double diffraction, according to the diffraction cross sections. The single-diffraction cross section is taken from Goulianos (1995) and the double-diffraction cross section is taken from Affolder et al. (2001) with a suppression of the double-diffraction process below 31 GeV according to Givernaud et al. (1979). Due to the difficulties involved in measuring the diffractive cross sections only a few data points are available. The probabilities of projectile and

[4]The simulation program is written in Python and is available upon request.

target diffraction are equal. The mass distribution of $M_X$ is taken as a combination of two nucleon resonances, N(1400) and N(1688), and a continuum contribution proportional to $1/M_X^2$ (Goulianos, 1983). The two resonances are not two physical resonances but rather collections of nucleon resonances around those masses. Figures 4.12 and 4.13 show the $M_X^2$ distributions for single and double diffraction interaction for proton kinetic energy $T_p = 21.3$ TeV, which corresponds to cms energy $\sqrt{s} = 200$ GeV. The contributions of the two nucleon resonances clearly stand out from the continuum tail.

The charged pion multiplicity is taken to follow a normal distribution with average

$$n_0 = 2\sqrt{M_X - m_p} \tag{4.19}$$

and rms of $n_0/2$ (Cool et al., 1982; Goulianos, 1983). By applying charge conservation the charge multiplicity is converted into numbers of pions, $n(\pi^+)$ and $n(\pi^-)$. Figure 4.14 shows the charged pion multiplicity distribution, for projectile and target single diffraction and double diffraction. For even multiplicity $n(\pi^+) = n(\pi^-)$ and for odd multiplicity $n(\pi^+) = 1 + n(\pi^-)$, because the associated baryon is a proton. The $\pi^0$ multiplicity is also taken to follow a normal distribution. The average is $n_0/2$ with a rms of $n_0/4$.

The pions will share the available energy, given by $M_X - m_p - nm_\pi$, where $n$ is the number of pions created. The kinetic energy carried by the nucleon created in the dissociation can be neglected above, since $m_p \gg m_\pi$ in the cms of the excited state. By applying energy-momentum conservation the momenta of the excited state, $\boldsymbol{p}_{M_X}$, and the produced pions are calculated in the cms and then transformed to the laboratory system. The momentum distribution for the excited state is shown in Figure 4.15. For projectile diffraction it peaks at the momentum of the projectile and it peaks at zero for target diffraction, i.e. a stationary target.

As a final remark, it is noted that the latest versions of Pythia (Sjöstrand et al., 2001a,b) include implementations of the diffractive interaction, and that the modeling here and the implementation in Pythia give similar results.

## 4.7 Average $\pi^0$ Multiplicity

To investigate the accuracy of the proton-proton interaction model adjusted with the two baryon resonances, the average $\pi^0$ multiplicity, $\langle N_{\pi^0} \rangle$, has been calculated and compared it with experimental data. The multiplicity is equivalent to the total $\pi^0$ inclusive cross section, i.e. the cross section for the reaction

$$p + p \rightarrow \pi^0 + X \tag{4.20}$$

where $X$ is any reachable state, because the two are connected through

$$\langle N_{\pi^0} \rangle = \frac{\sigma_{\pi^0}}{\sigma_{pp}} \tag{4.21}$$

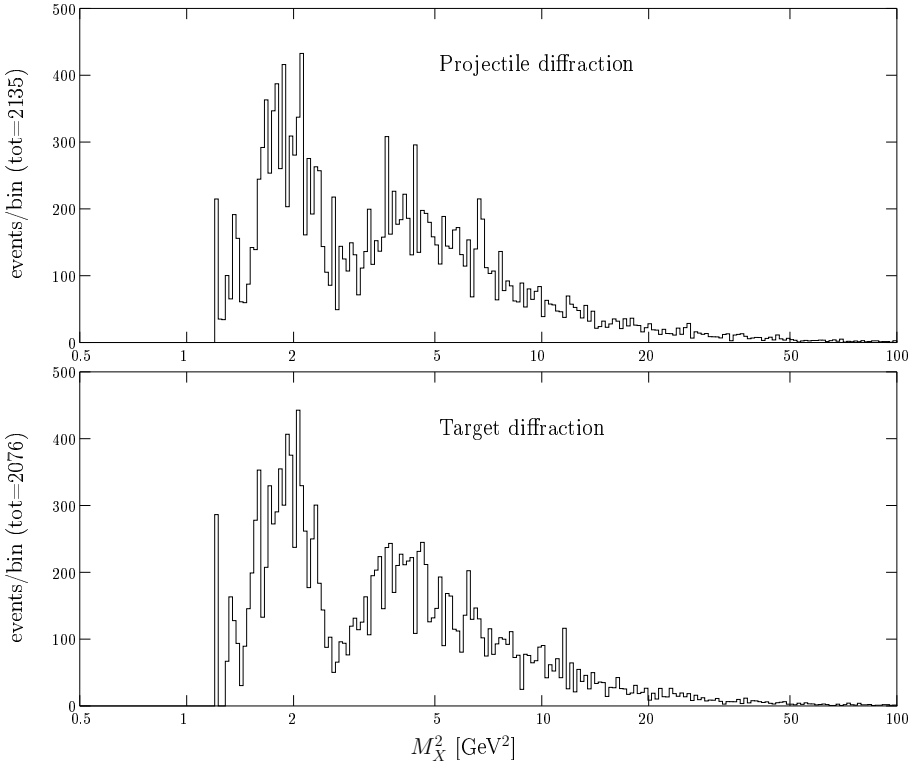


**Figure 4.12:** $M_X^2$ distributions from single diffractive interaction for proton kinetic energy 21.3 TeV. Top panel is for projectile diffraction and bottom panel is for target diffraction. The peaks at about $M_X^2 = 2$ GeV/c$^2$ and $M_X^2 = 5$ GeV/c$^2$ are from the contributions of the two nucleon resonances N(1400) and N(1688) and the tail extending to high masses comes from the continuum contribution. The sharp peak at $M_X^2 = 1.2$ GeV$^2$ is an artifact of the simulations.

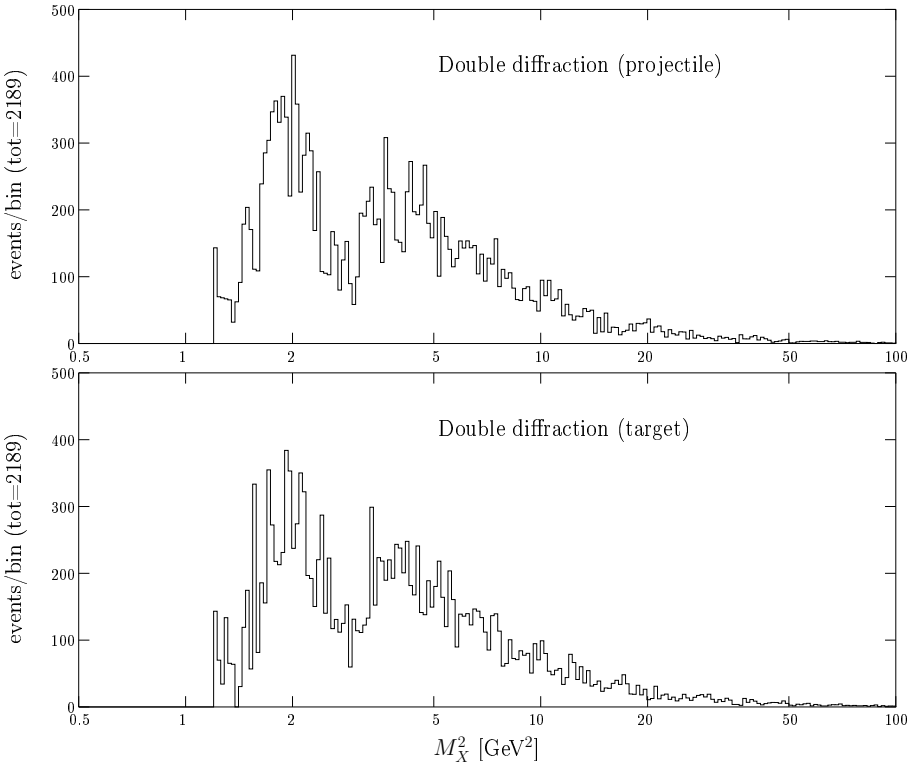


**Figure 4.13:** $M_X^2$ distributions from double diffractive interaction for proton kinetic energy 21.3 TeV. Top panel is for projectile diffraction and bottom panel is for target diffraction. The peaks at about $M_X^2 = 2$ GeV/c$^2$ and $M_X^2 = 5$ GeV/c$^2$ are from the contributions of the two nucleon resonances N(1400) and N(1688) and the tail extending to high masses comes from the continuum contribution. The sharp peak at $M_X^2 = 1.2$ GeV$^2$ is an artifact of the simulations.

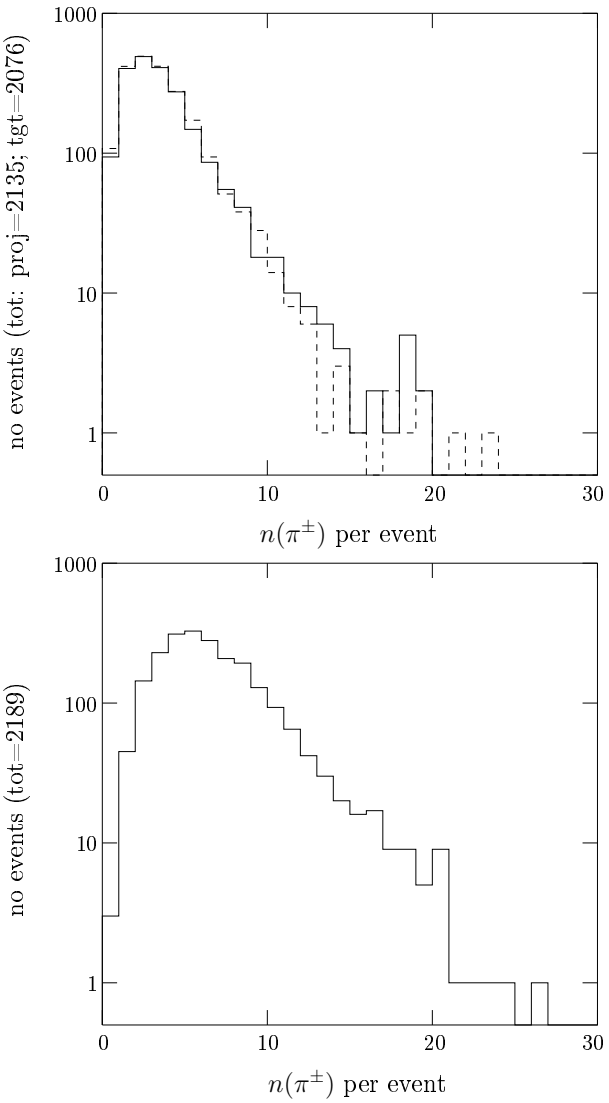


**Figure 4.14:** Charged pion multiplicity, i.e. number of produced charged pions per event, from simulations of the diffractive interaction for a proton kinetic energy of 21.3 TeV. The upper panel is for single diffraction, target (solid) and projectile (dashed), the bottom panel is for double diffraction. The histograms for single diffraction show that the charge multiplicity was taken from a normal distribution. The histogram for double diffraction is expected to have a maximum at a slightly higher $n(\pi^{\pm})$ than singel diffraction and a distribution deviating from the normal distribution.

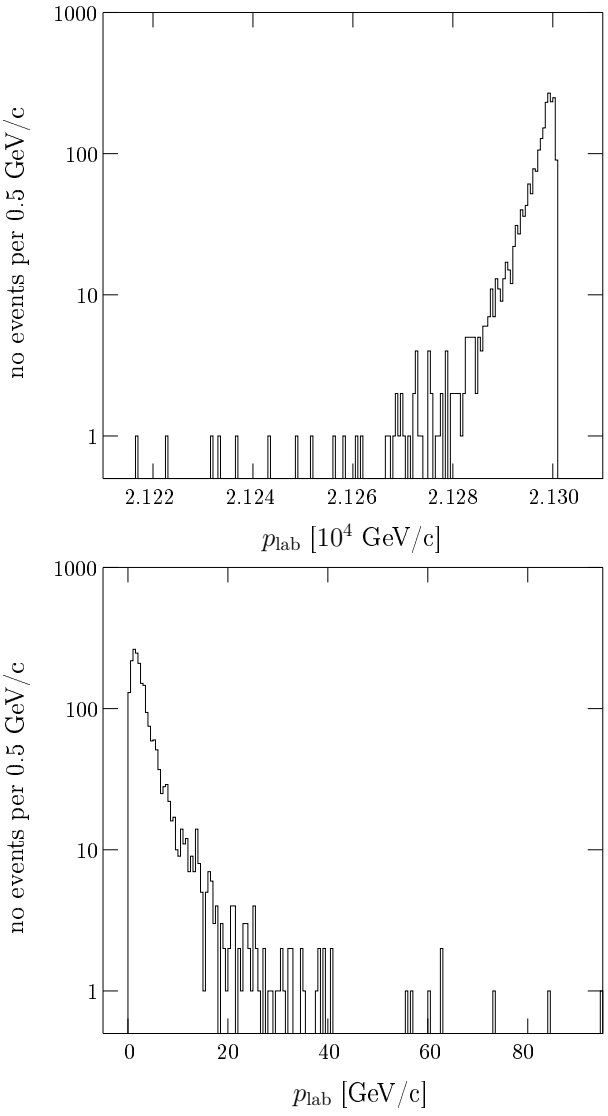


**Figure 4.15:** Momentum distributions of the excited state from simulations of the diffractive interaction at proton kinetic energy 21.3 TeV. Top panel is for projectile diffraction and bottom panel is for target diffraction. For projectile diffraction, the momentum distribution peaks at the projectile momentum, and for target diffraction, the momentum distribution peaks at zero, i.e. a stationary target.

where $\sigma_{\pi^0}$ is the total inclusive $\pi^0$ cross section and $\sigma_{pp}$ is the proton-proton cross section. For diffractive simulations, non-diffractive simulations with Pythia and the baryon resonances, $\langle N_{\pi^0} \rangle$ is calculated as the number of $\pi^0$ created divided by the number of simulated proton-proton interaction events. For the low energy non-diffractive simulation, the total inclusive $\pi^0$ cross section is directly used. Blattnig et al. (2000) gives the inclusive cross sections in algebraic forms, but because the two baryon resonances were included, they had to be slightly reduced. The data were adjusted and then fitted to an algebraic form. The form taken was based on equation 29 of Blattnig et al. (2000), resulting in

$$\sigma_{\pi^0} = \left(0.00831 + 0.103\frac{\ln(T_{\text{lab}})}{T_{\text{lab}}} + \frac{0.388}{T_{\text{lab}}}\right)^{-1} + \sqrt{T_{\text{lab}} - 0.488} - 0.68 \qquad (4.22)$$

where $T_{\text{lab}}$, the proton kinetic energy in the laboratory system, is in units of GeV. The total cross sections for charged pions is also given in Blattnig et al. (2000). Due to lack of data on these cross sections, they were adjusted in the following way

$$\sigma_{\pi^\pm} = \sigma_{\pi^0} R \qquad (4.23)$$

where $R = \sigma_{\pi^\pm}/\sigma_{\pi^0}$ is the ratio of the cross sections given in Blattnig et al. (2000). Note that this is not an exact representation, but accurate enough for this work.

Figure 4.16 shows the calculated total inclusive $\pi^0$ cross section and the contribution from the different components and compare it with experimental data compiled by Stecker (1970) and Dermer (1986a). It can be concluded that the contributions of the baryon resonances $\Delta(1232)$ and res(1600) are needed to make the model accurate over the full momentum range.

## 4.8 Pion Transverse Momentum

The angular distribution of gamma rays depends on the $\pi^0$ transverse momentum distribution. To verify that the above described proton-proton interaction model produces correct gamma-ray angular distribution, the $\pi^0$ transverse momentum distribution has been compared with experimental data. Figure 4.17 shows the calculated invariant $\pi^0$ cross section, $Ed^3\sigma/dp^3$, at production angle $\theta^* = 90°$ for proton kinetic energies $T_p = 1.41$ TeV ($\sqrt{s} = 51.5$ GeV) and $T_p = 181$ TeV ($\sqrt{s} = 582$ GeV) together with experimental data for $\pi^\pm$ and $\pi^0$ measured at the ISR at $\sqrt{s} = 53$ GeV (Alper et al., 1975) and by the UA2 collaboration at $\sqrt{s} = 540$ GeV (Banner et al., 1982, 1983). One must note that the ISR was a $pp$ collider and that UA2 was a $\bar{p}p$ collider experiment at the SPS. There are slight differences between in the expected distributions from $pp$ and $\bar{p}p$ interactions. This explains parts of the differences between the data points and model curve. The $\pi^0$ transverse momentum distributions follow the expected exponential form for $p_t < 1.5$ GeV/c.

In addition, the energy dependence of the $\pi^0$ average transverse momentum, $\langle p_t \rangle$, from the model has been compared with experimental data from ISR experiments. In accelerator experiments it is difficult to measure $\pi^0$ directly but one

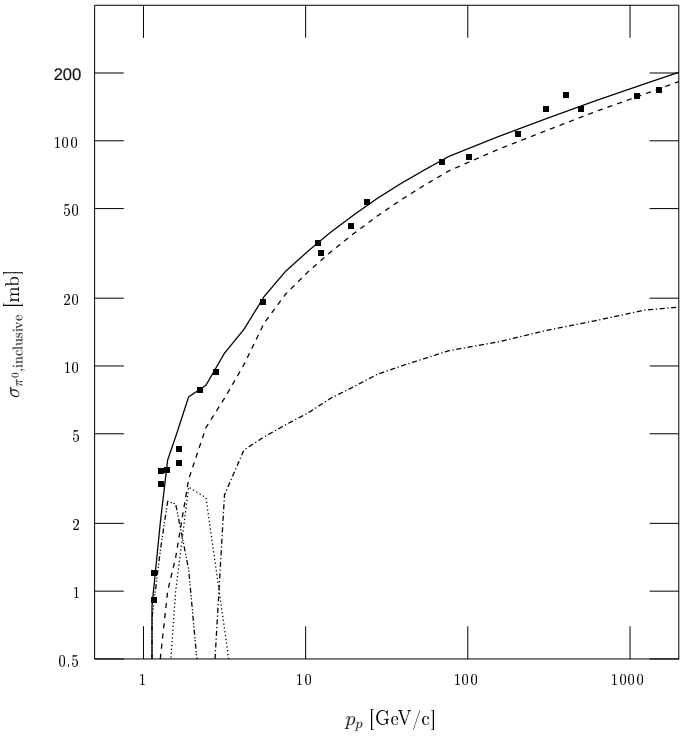


**Figure 4.16:** Experimental and simulated total $\pi^0$ inclusive cross section as function of proton laboratory momentum. Data points are those compiled by Stecker (1970) and Dermer (1986b) and the lines are total (solid), non-diffractive (dashed), diffractive (dot-dashed), $\Delta(1232)$ (dotted) and res(1600) (dot-dot-dash).

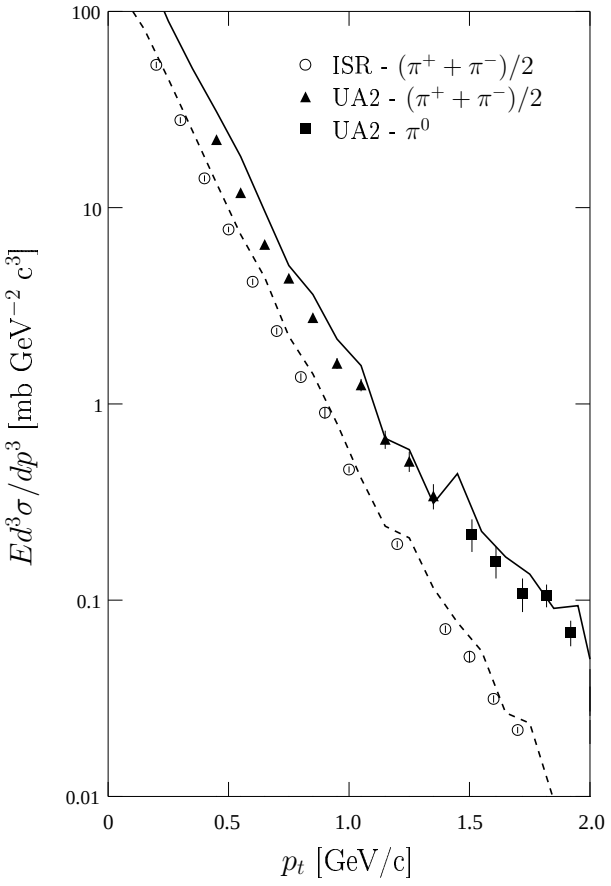


**Figure 4.17:** Experimental invariant cross section $Ed^3\sigma/dp^3$ at production angle $\theta_{\rm cms} = 90^\circ$ and beam energy $\sqrt{s} = 540$ GeV for $(\pi^+ + \pi^-)/2$ (filled triangles) and $\pi^0$ (filled squares) measured by the UA2 collaboration ($\bar{p}p$ collider experiment; Banner et al., 1982, 1983) and beam energy $\sqrt{s} = 53$ GeV for $(\pi^+ + \pi^-)/2$ (open circles) measured at the ISR ($pp$ collider; Alper et al., 1975) together with the $\pi^0$ invariant cross section calculated from Monte Carlo simulations in this work at $T_p = 181$ TeV ($\sqrt{s} = 582$ GeV, solid line) and $T_p = 1.41$ TeV ($\sqrt{s} = 51.5$ GeV, dashed line). The kinks in the lines are due to limited event statistics and finite sized bins.

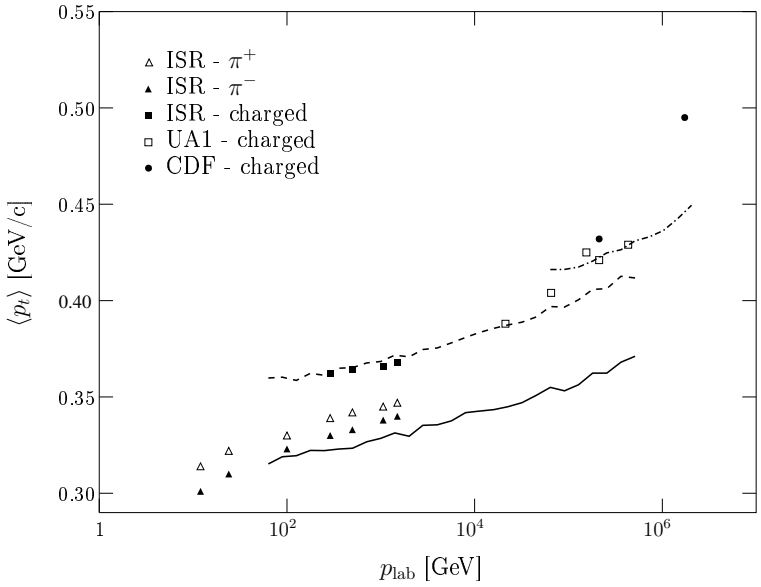


**Figure 4.18:** Average transverse momentum, $\langle p_t \rangle$, for production of pions and all charged particles ($\pi^{\pm}$, $K^{\pm}$ and protons) versus the laboratory momentum. Data points are for $\pi^+$ (open triangles), $\pi^-$ (filled triangles) and all charged particles (filled squares) from ISR, all charged particles (filled diamonds) from UA1 and all charged particles (filled circles) from CDF. ISR data are from $pp$ collider experiments and are taken from Rossi et al. (1975) and UA1 and CDF data are from $\bar{p}p$ collider experiments and are taken from Abe et al. (1988). Lines are for $\pi^0$ (solid line), all charged particles (dashed line) and all charged particles from Pythia 6.4 (dot-dashed line) calculated from the Monte Carlo simulations in this work.

can expect that $\langle p_t[\pi^0] \rangle \simeq \langle p_t[\pi^{\pm}] \rangle$ (Alner et al., 1987). Figure 4.18 shows the calculated $\langle p_t[\pi^0] \rangle$ as a function of the proton momentum in the laboratory frame together with experimental data for $\pi^{\pm}$. The calculation of $\langle p_t \rangle$ was done without any model fitting. Rossi et al. (1975) estimated the error on $\langle p_t[\pi^{\pm}] \rangle$ to be about 10% and $\langle p_t[\pi^0] \rangle$ calculated here is within this error margin.

At very high proton momenta experimental data is in general limited to the average transverse momentum of charged particles, $\langle p_t[\text{charged}] \rangle$, where charged particles include charged pions, charged kaons and protons. Again, without fitting, $\langle p_t[\text{charged}] \rangle$ was calculated from Monte Carlo event data and compared with experimental data measured at the ISR and by the UA1 and CDF collaborations.[5] As can been seen in Figure 4.18 the difference is on the order of a few percent except at very high energies. The discrepancy in average transverse momentum at

[5]Note again that ISR was a $pp$ collider and that UA1 and CDF are $\bar{p}p$ collider experiments.

high proton momentum is inherent to Pythia 6.2 and the parameter set "tune A" which has not been fine-tuned to the highest energy data available from the CDF collaboration (T. Sjöstrand 2007, private communications).

The averagee $p_t$ has also been calculated for all charged particles from Monte Carlo simulations with Pythia 6.4 and parameter set "tune DWT" at CDF energies; shown in the Figure 4.18. The agreement is much better with data from the UA1 collaboration and the CDF data point for $\sqrt{s} = 630$ GeV. The highest data point from CDF is still not well reproduced. It is also clear that $\langle p_t \rangle$ attains a much to high value for lower energies as discussed in Chapter 4.

# Chapter 5

# Parametric Model for Stable Secondary Particles

The spectra of gamma rays and neutrinos due to pion decays in astronomical environments depend strongly on the source spectrum of protons involved in the proton-proton interactions. Such source spectra can not be measured directly because protons are electrically charged. Electrically charged particles interact with Galactic magnetic fields and protons measured at Earth cannot be associated with any specific source. The proton spectrum has to be derived, usually from the observed gamma-ray spectrum, which requires iterative calculations where one inputs trial proton spectra and compares the resulting gamma-ray spectra with the observed one.

Running Monte Carlo simulations in every iteration of such calculations is much too time consuming. Having a parametric model which replaces simulations simplifies the calculations. To meet the needs of an improved model for proton-proton interactions in astronomical environments, proton-proton interactions have been simulated and the resulting yields and spectra of stable secondary particles, gamma rays, electrons, positrons, $\nu_e$, $\bar{\nu}_e$, $\nu_\mu$, and $\bar{\nu}_\mu$, have been parameterized as functions of the incident proton kinetic energy and the total energy of the secondary particle.

Not all astrophysical sources with possible proton acceleration are expected to have an isotropic distribution of protons. When there are anisotropies the gamma-ray spectrum will also be anisotropic and the observed flux and spectrum will be dependent on the angle of the proton beam relative to the line of sight. For accurate calculations it is necessary to have a model which includes the angular dependencies. The angular dependence is directly related to the transverse momentum distribution of the secondary particle. The presented model includes a parameterization of the gamma-ray transverse momentum distribution. With this formalism, the gamma-ray spectrum can be calculated for any given distribution of protons, including angular dependent ones.

Parameterization of the angular distributions of other stable secondary particles, i.e. electrons, positrons and neutrinos, has been deferred due to observational limitations. When high-statistics neutrino data becomes available (Halzen, 2005) it may be worthwhile to extend the parameterization to include the angular distribution of neutrinos.

The results presented in this chapter are those of Kamae et al. (2006) and Karlsson & Kamae (2007). The focus here is on gamma rays. For the interested, other figures and data are available upon request from the author.

## 5.1 Monte Carlo Event Generation

Based on the proton-proton interaction model described in Chapter 4, event data were generated for all the stable secondary particles; gamma rays, electrons, positrons and two neutrino species, $\nu_e$, $\nu_\mu$, and their anti-particles, $\bar{\nu}_e$, $\bar{\nu}_\mu$. Events were generated at discrete proton kinetic energies following a geometric series

$$T_p = 1000 \cdot 2^{(i-22)/2} \text{ GeV}, \ \text{i} = 0, \ldots, 40 \tag{5.1}$$

i.e. from 488 MeV to 512 TeV. Each proton kinetic energy represents a bin centered at $T_p$ and with width $\Delta \log T_p = \log \sqrt{2}$. The kinetic energies were chosen in this manner to achieve equally spaced bins in logarithmic scale. This was done separately for the non-diffractive, the diffractive, and each of the baryon resonance components. Events were not generated for kinetic energies where the component of the inelastic cross section is very small or zero, i.e. the diffractive process was simulated for proton kinetic energies 1.95 GeV and above and baryon resonances in the interval 0.488 GeV to 2.76 GeV. In addition, the two baryon resonances required an increased sampling frequency near the pion production threshold and events were also generated for $T_p = 0.58$ GeV and 0.82 GeV.

The particle distributions from simulations of events in this manner are referred to as *exclusive* distributions. The inclusive secondary particle distributions are then obtained by collecting all secondary particles produced in exclusive proton-proton events. Simulations of the high-energy non-diffractive process with Pythia and simulations of the diffractive process and resonance excitations outputs data on total energy $E$ and three-momentum $\boldsymbol{p}$, with components $p_x$, $p_y$ and $p_z$, for each produced secondary particle. The parametric model by Blattnig et al. (2000) on the other hand only gives the pion multiplicities at a given total energy. To obtain the angular distribution for $\pi^0$ events, i.e. data on momentum components $p_x$, $p_y$ and $p_z$, another simulation code[1] was written.

### 5.1.1 Pion Decay

The Monte Carlo simulations of all components, except the simulations with Pythia, where all unstable particles were forced to decay instantly, resulted in pion events.

[1]The code that simulates $\pi^0$ angular distribution is available upon request from the author.

These had to be decayed to the stable secondary particles of interest. This was done using the quasi V-A decay kinematics implemented within Geant4[2]. Part of the discrepancy when matching the scaling model and Pythia may be explained by differences in the implementation of the V-A matrix elements in Geant4 and Pythia. It also noted that Pythia includes radiative corrections to QED and direct gamma-ray production from QCD and the number of gamma rays from Pythia simulations is a few percent higher than twice the number of neutral pions.

In the scaling model for low-energy non-diffractive interactions, the spectral distributions give the number of pions for a given proton kinetic energy and pion kinetic energy in the laboratory frame. To generate stable secondary particle events the following scheme was used. For gamma rays, the number of $\pi^0$ were calculated in 240 bins of $T_\pi$ between 1 MeV and 1 TeV, with $T_\pi$ being the central value of the bin and the bin width is $\Delta \log(T_\pi) = 0.025$, for each $T_p$. It is assumed that no pions are produced with kinetic energy above 1 TeV. The $\pi^0$ were then instantly decayed to gamma rays. The resulting histograms were re-binned to match the 180 bins from the other components of the model. Mixing was also included, according to Section 4.4.2.

For charged pions, a list of pions was generated such that there were 100 pions in each bin of $T_\pi$ of width $\Delta \log(T_\pi) = 0.05$. The binning region covered from $T_\pi = 1$ MeV to $T_\pi = 1$ TeV. The pions were decayed and binned in histograms on a per bin basis, i.e. 120 histograms with 100 events in each histogram. The per-bin histograms were then normalized to each other using the spectral distribution from Blattnig et al. (2000) and summed together to form the final histogram of stable secondaries. Again, it was assumed that no pions were produced with kinetic energy above 1 TeV and mixing was included.

### 5.1.2 Neutron $\beta$-decay

All of the processes in the inelastic proton-proton interaction produces two nucleons and one or more pions according to

$$p + p \rightarrow p + N + n\pi \tag{5.2}$$

where the nucleon $N$ can be either a proton or a neutron (neutron production limited by charge conservation) and $n$ is the pion multiplicity. Free neutrons are unstable with a mean lifetime of about 886 s and $\beta$-decay

$$n \rightarrow p + e^- + \bar{\nu}_e \tag{5.3}$$

To a first approximation, the electron is assumed to get total energy

$$E_e = \frac{m_e}{m_n} E_n \tag{5.4}$$

where $E_n$ is the energy of the neutron. Electrons from neutron events are then collected from the Monte Carlo simulations and binnes in histograms $\Delta N / \Delta \log(E)$

[2]This Geant4 program was written by T. Koi, coauthor of Kamae et al. (2005), and is available upon request from the author.

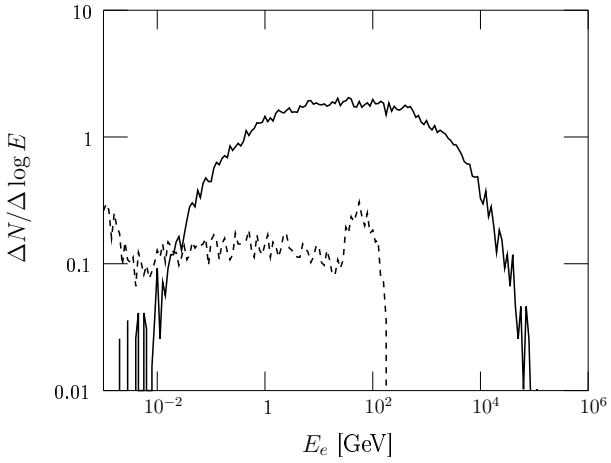


**Figure 5.1:** The contribution of electrons from neutron $\beta$-decay (dashed line) versus the electron spectrum from $\pi^-$ decays (solid line) for $T_p = 512$ TeV. Both spectra are normalized to be per proton-proton interaction. To a first approximation, the electron carries only a small amount of the neutron energy. The electron spectrum from neutron decays is shifted toward lower energies and the overall contribution is only about 10%. The peaks at 1 MeV and 100 GeV are due to kinematics under the assumption that the electron only carries a small fraction of the energy.

in the same manner as above. Figure 5.1 shows the obtained electron spectrum due to neutron $\beta$-decay and compares it to the overall electron spectrum for the non-diffractive interaction at 512 TeV. The spectrum is shifted toward lower energies, because the electron carries only a small fraction of the neutron energy and the contribution to the overall electron spectrum from neutron $\beta$-decay is small and has been neglected in further analysis. This also means that the contribution to the $\bar{\nu}_e$ spectrum has been neglected.

## 5.2 Inclusive Cross Sections

The differential inclusive cross section for each secondary particle was calculated using above mentioned histograms, $\Delta N/\Delta \log(E)$, and

$$\frac{\Delta\sigma_{\text{incl}}(E)}{\Delta \log(E)} = \frac{1}{N_{pp}} \frac{\Delta N}{\Delta \log(E)} \sigma_{pp} \tag{5.5}$$

where $E$ is the secondary particle total energy, $N_{pp}$ is the number of proton-proton interaction events simulated (typically 6400 events, but for Pythia at very-high

proton kinetic energies, 3200 or 1600 events) and $\sigma_{pp}$ is the cross section for proton-proton interactions at given proton kinetic energy, calculated using equations 4.11, 4.12, 4.13 and 4.14. Figure 5.2 shows the obtained inclusive gamma-ray cross sections from non-diffractive and diffractive simulations for a few proton kinetic energies.

The differential inclusive cross sections, given by equation 5.5, were then fitted to an algebraic form $F(x)$, with $x = \log(E)$ and $E$ in GeV. The differential inclusive cross section is taken to be

$$\frac{\Delta\sigma_{\mathrm{incl}}(E)}{\Delta \log(E)} = F(x)F_{\mathrm{kl}}(x) \tag{5.6}$$

where $F_{\mathrm{kl}}(x)$ is a cutoff function that approximately enforces the energy-momentum conservation.

The form $F(x)$ is different for each of the components. The non-diffractive cross section was fitted to

$$\begin{aligned} F_{\mathrm{nd}}(x) &= a_0 \exp(-a_1(x - a_3 + a_2(x-a_3)^2)^2) + \\ &\quad a_4 \exp(-a_5(x - a_8 + a_6(x-a_8)^2 + a_7(x-a_8)^3)^2) \end{aligned} \tag{5.7}$$

with cutoff function

$$F_{\mathrm{kl,nd}}(x) = \frac{1}{(\exp(W_{\mathrm{nd,l}}(L_{\min} - x)) + 1)} \frac{1}{(\exp(W_{\mathrm{nd,h}}(x - L_{\max})) + 1)} \tag{5.8}$$

Here $L_{\min}$ and $L_{\max}$ are the lower and upper kinematic cutoff limits and $W_{\mathrm{nd,l}}$ and $W_{\mathrm{nd,h}}$ are the widths. For gamma rays these values are

$$\begin{aligned} L_{\min} &= -2.6 \\ L_{\max} &= 0.96 \log(T_p) \\ W_{\mathrm{nd,l}} &= 15 \\ W_{\mathrm{nd,h}} &= 44 \end{aligned}$$

Table C.1 summarizes the values for these parameters for all secondary particles.

The diffractive cross section was fitted to

$$\begin{aligned} F_{\mathrm{diff}}(x) &= b_0 \exp(-b_1((x - b_2)/(x + b_3(x - b_2)))^2) + \\ &\quad b_4 \exp(-b_5((x - b_6)/(x + b_7(x - b_6)))^2) \end{aligned} \tag{5.9}$$

and the baryon resonance cross sections to

$$F_{\Delta}(x) = c_0 \exp(-c_1((c - c_2)/(1 + c_3(x - c_2) + c_4(x - c_2)^2))^2) \tag{5.10}$$

and

$$F_{\mathrm{res}}(x) = d_0 \exp(-d_1((c - d_2)/(1 + d_3(x - d_2) + d_4(x - d_2)^2))^2) \tag{5.11}$$

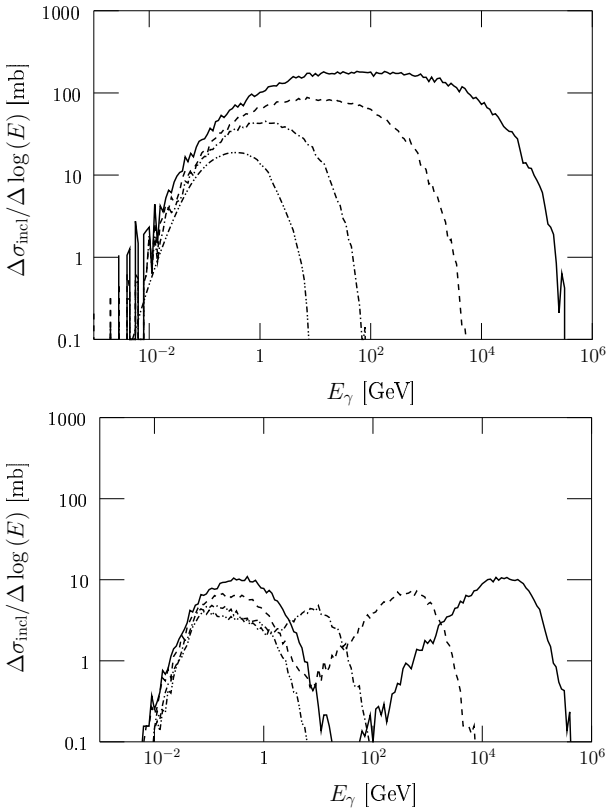


**Figure 5.2:** Gamma-ray inclusive cross sections for four proton kinetic energies: the non-diffractive process (upper) and the diffractive process (lower). The four proton kinetic energies are $T_p = 512$ TeV (solid), 8 TeV (dashed), 125 GeV (dot-dashed) and 11.1 GeV (dotted). The bin width is $\Delta\log(E) = 0.05$. The fluctuations in the histograms at the highest and lowest ends are due to statistics in the simulations.

all with the cutoff function

$$F_{\mathrm{kl}}(x) = \frac{1}{\exp\left(W(x - L_{\max})\right) + 1} \tag{5.12}$$

with $L_{\max} = \log(T_p)$, $T_p$ in GeV, and $W = 75$.

The parameterized gamma-ray inclusive cross section is compared with the simulate one for a few proton kinetic energies in Figure 5.3 for the non-diffractive and diffractive processes, and Figure 5.4 for the baryon resonances. The agreement is generally good, except near the kinematic limits, where the difference can be as much as 10-20%.

### 5.2.1 Representation of Parameters

The fitting of simulated inclusive cross sections results in a set of parameters, $a_0, \ldots, a_8$, $b_0, \ldots, b_7$, $c_0, \ldots, c_4$ and $d_0, \ldots, d_4$, for each proton kinetic energy. The final step toward a parametric model of the inclusive cross sections is to find algebraic forms for these parameters, e.g.

$$a_i = f_i(\log(T_p)) \tag{5.13}$$

Here $T_p$ is in TeV, not GeV. These functions were determined by fitting the parameters. For gamma rays, the fitted functions are listed in Table C.2. Some manual adjustments have sometimes been necessary to control artifacts near the kinematic limits.

### 5.2.2 Renormalization of Inclusive Cross Section

To ensure that the parametric model for gamma-rays reproduces the experimental $\pi^0$ inclusive cross section (Figure 4.16), the parameterized inclusive cross section has been renormalized to that from Monte Carlo simulations. By calculating the integrated gamma-ray yield for the parameterized model and the Monte Carlo data, the renormalization is the ratio between them as a function of proton kinetic energy $r(T_p)$ resulting in our best fit

$$r(y) = 3.05 \exp\left(-107((y + 3.25)/(1 + 8.08(y + 3.25)))^2\right) \tag{5.14}$$

to the ratio, where $y = \log(T_p)$, for $T_p < 1.95$ GeV. Above 1.95 GeV, the ratio is constant and $r(y) \simeq 1.01$. Note that this adjustment did not affect the diffractive process or the resonance excitation processes. For all other secondary particles, $r(y = \log(T_p))$, is listed in the tables in Appendix C.2.

### 5.2.3 Gamma-Ray Spectrum

As an example on how this parametric model can be used, the gamma-ray spectra from protons with power-law indices 2 and 2.7 have been calculated. This is shown

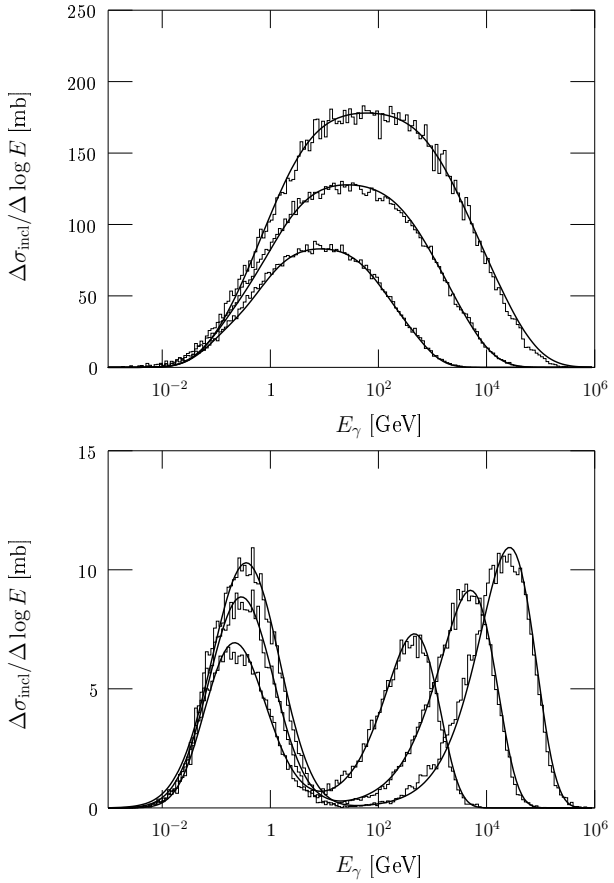


**Figure 5.3:** Parameterized (solid line) and simulated (histograms) inclusive gamma-ray cross sections for non-diffractive (upper panel) and diffractive (lower panel) process. The inclusive gamma-ray cross sections are shown for proton kinetic energies $T_p = 8$ (lower), 64 (middle) and 512 TeV (top). The parameterized cross sections are those defined by equations 5.7 and 5.9 with parameters in Table C.2.

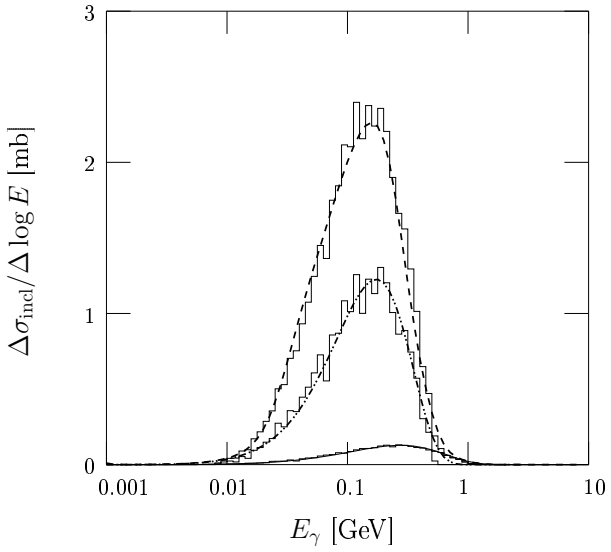


**Figure 5.4:** Parameterized (solid line) and simulated (histograms) inclusive gamma-ray cross sections for the baryon resonance excitation processes at proton kinetic energy $T_p = 0.69$ GeV. The lines are: $\Delta(1232)$ resonance (dotted), res(1600) resonance (thin solid) and total (dashed), i.e. the sum of all model contributions. The parameterized cross sections are those defined by equations 5.10 and 5.11 with parameters in Table C.2.

in Figure 5.5 where the model calculations are compared with the corresponding spectra from simulations.

The differential gamma-ray flux due to a given proton spectrum $J_p$ is calculated using

$$\frac{dF}{dE} = \int dT_p J_p(T_p) \frac{d\sigma(T_p, E)}{dE} \tag{5.15}$$

where $T_p$ is the proton kinetic energy and $E$ is the gamma-ray energy. For protons following a power-law spectrum

$$J_p(T_p) = n_0 T_p^{-\Gamma} \tag{5.16}$$

where $n_0$ is the flux normalization and $\Gamma$ is the power-law index. For simplicity, $n_0 = 1.0$ in the calculations here. The integral in equation 5.15 is approximated as a sum over proton kinetic energies from 488 MeV to 512 TeV. The inclusive cross section $d\sigma/dE$ is the sum of the cross sections from the four contributing components. The spectra shown in Figure 5.5 for $\Gamma = 2.0$ and $\Gamma = 2.7$, are plotted as $E^2 dF/dE$ to better show the power-law shapes of the spectra. As seen in Figure 5.5, both spectra are reproduced within 10%, except near the higher kinematical limit where the error can be as much as 20%. The asymptotic power law to these spectra have also been calculated and have index 1.95 for power-law protons of index 2.0 and 2.68 for proton index 2.7.

### 5.2.4 Electrons, Positrons and Neutrinos

The parameterization procedure has been applied to all the other stable secondary particles, i.e. electrons, positrons, $\nu_e$, $\bar{\nu}_e$, $\nu_\mu$, and $\bar{\nu}_\mu$ as well. The resulting functions for the parameters are tabulated in Appendix C.2. Because of how the $\Delta(1232)$ resonance was modeled, no $\pi^-$ were produced in that process and thus, no electrons or $\bar{\nu}_e$ either.

It is noted that more positrons than electrons are produced in the simulations and hence, also in the parametric model. This difference can be explained by charge conservation and the exclusion of neutron $\beta$-decays. In the simulations, the number of electrons and number of positrons is matched when including electrons from neutron $\beta$-decay.

The electron and positron spectra due to protons following power laws with index $\Gamma = 2$ and $\Gamma = 2.7$ have been calculated using equation 5.15 in the same way as for gamma rays. Figure 5.6 shows thus obtained spectra. Superimposed in the plots is the contribution of electrons coming from decays of neutrons. As can be seen in the figure, this contribution is negliable, except at very-low energies.

## 5.3 Transverse Momentum Distributions

The Monte Carlo simulations described earlier generate data on three-momentum, $\mathbf{p} = (p_x, p_y, p_z)$, and total energy, $E$, for each gamma-ray photon. Since the incident

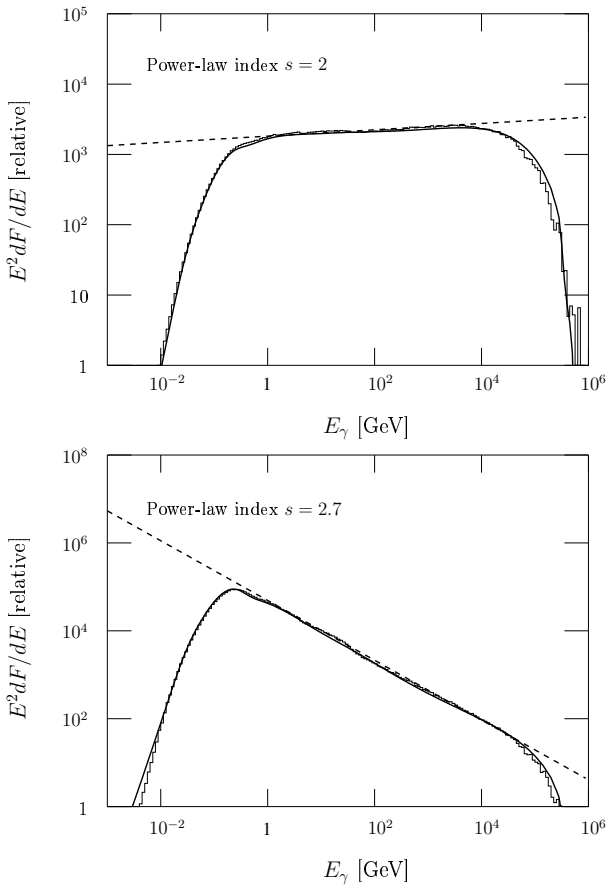


**Figure 5.5:** Gamma-ray spectrum produced by protons with a power-law spectrum cutoff at $T_p = 512$ TeV. The upper panel is for index $\Gamma = 2$ and lower panel is for index $\Gamma = 2.7$. The histograms are those from simulations and the solid lines are calculated using the parametric model. The dashed lines are the asymptotic power laws with index $\Gamma = 1.95$ and $\Gamma = 2.68$ respectively.

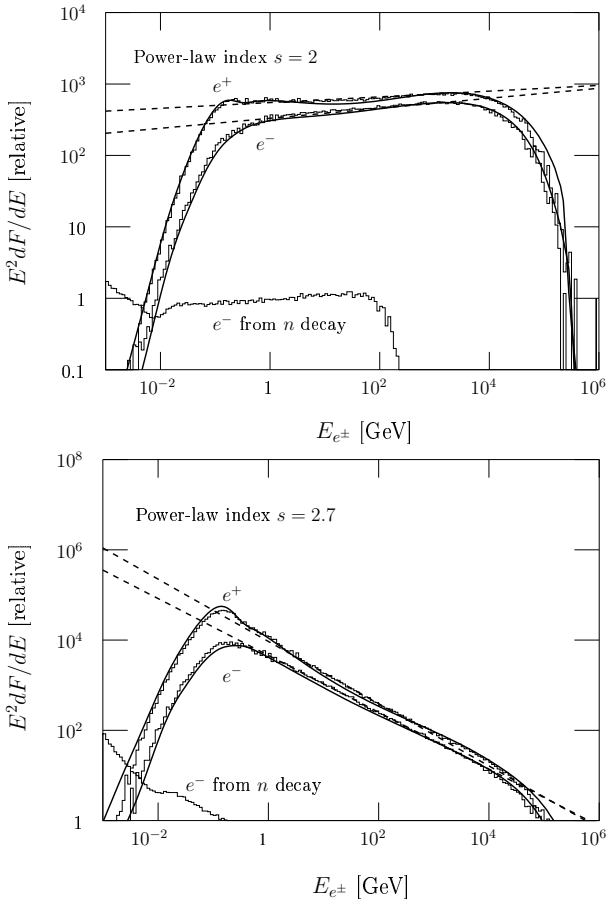


**Figure 5.6:** Electron and positron spectra produced by protons with a power-law spectrum cutoff at $T_p = 512$ TeV. The upper panel is for index $\Gamma = 2$ and lower panel is for index $\Gamma = 2.7$. The histograms are those from simulations and the solid lines are calculated using the parametric model. The dashed lines are the asymptotic power laws: for electrons with index $\Gamma = 1.93$ and $\Gamma = 2.63$, respectively, and for positrons with index $\Gamma = 1.96$ and $\Gamma = 2.69$, respectively. The histogram in the lower left corner in both show the electron spectrum produced by the decay of neutrons. As can be seen the contribution is small except at the very lowest energies.

proton direction in the simulations is along the z-axis, the transverse momentum, $p_t$, is simply

$$p_t = \sqrt{p_x^2 + p_y^2} \tag{5.17}$$

and this was calculated for each simulated event. Events were then binned in 2D histograms

$$\frac{\Delta^2 N}{\Delta \log(E) \Delta p_t} \tag{5.18}$$

over total energy, $E$, and transverse momentum, $p_t$, with one histogram per proton kinetic energy. Bins widths were taken to be $\Delta \log(E) = 0.05$ and $\Delta p_t = 10$ MeV/c.

Normalization to the proton-proton inelastic cross section, $\sigma_{pp}$ given by eqs. 4.11 through 4.14, and per proton-proton interaction gives the differential cross section

$$\frac{\Delta^2 \sigma}{\Delta \log(E) \Delta p_t} = \frac{\sigma_{pp}}{N_{pp}} \frac{\Delta^2 N}{\Delta \log(E) \Delta p_t} \tag{5.19}$$

where $N_{pp}$ is the number of proton-proton events simulated and $\Delta N$ is the number of gamma rays in a given bin. This differential cross section is a representation of the angular distribution of gamma rays.

For each proton kinetic energy, $T_p$, the transverse momentum distribution is parameterized as

$$\frac{\Delta^2 \sigma}{\Delta \log(E) \Delta p_t} = p_t F(p_t, x) F_{\mathrm{kl}}(p_t, x) \tag{5.20}$$

where $x = \log(E[\mathrm{GeV}])$, $F(p_t, x)$ is the function representing the differential cross section $\Delta\sigma/\Delta p_t^2$ and $F_{\mathrm{kl}}(p_t, x)$ is used to approximately enforce the energy-momentum conservation. Assuming axial symmetry around the $p_{\parallel}$ axis, phase space is proportional to $dp_t^2 dp_{\parallel} = 2 p_t dp_t dp_{\parallel}$, which gives the extra factor of $p_t$ in equation (5.20).

The function $F_{\mathrm{kl}}(p_t, x)$ enforcing the energy-momentum conservation is taken to be

$$F_{\mathrm{kl}}(p_t, x) = \frac{1}{\exp(W(p_t - L_p)) + 1} \tag{5.21}$$

where $W = 75$ and

$$L_p = \begin{cases} 0.0976 + 0.670 \exp(1.81x) & x < -1 \\ -0.793 + \exp(0.271(x+1) + 0.363(x+1)^2) & -1 \le x < 0.5 \\ 2.5 & x \ge 0.5 \end{cases} \tag{5.22}$$

with $x = \log(E[\mathrm{GeV}])$.

In contrast to the parameterization of inclusive cross sections, where the non-diffractive and the diffraction contribution were treated separately, the two are here merged to one contributing component. This is well justified in astrophysical contexts. The new component is from here on referred to as the non-resonance component.

The $p_t$ distribution is given by 2D histograms, one histogram per proton kinetic energy, $T_p$, and component: non-resonance, $\Delta(1232)$, and res(1600). Each

histogram is fitted in slices along $p_t$, i.e. each slice $\Delta\sigma/\Delta p_t^2$ covers one bin of $\Delta\log(E)$. Note that $\Delta\sigma/\Delta p_t^2$ does not imply integrating over $\log(E)$.

For the non-resonance component $\Delta\sigma/\Delta p_t^2$ is expected to follow an exponential form

$$F_{\rm nr}(p_t, x) = a_0 \exp\left(-\frac{p_t}{a_1}\right) \tag{5.23}$$

Parameter $a_1$ gives the shape of the differential cross section and $a_0$ gives the absolute normalization. When integrating over $p_t$ one should recover the inclusive cross section $\Delta\sigma/\Delta\log(E)$, i.e.

$$\int_0^\infty \frac{\Delta\sigma}{\Delta p_t^2} dp_t = \frac{\Delta\sigma}{\Delta\log(E)} \tag{5.24}$$

Thus, $a_0$ is taken such that

$$a_0 \int_0^\infty p_t \exp\left(-\frac{p_t}{a_1}\right) dp_t = \frac{\Delta\sigma}{\Delta\log(E)} \tag{5.25}$$

which gives

$$a_0 = \frac{1}{a_1^2} \frac{\Delta\sigma}{\Delta\log(E)} \tag{5.26}$$

and $\Delta\sigma/\Delta\log(E)$ is calculated using the parameterization of the inclusive cross section.

Parameter $a_1$ is a function of both the gamma-ray energy, $E$, and the proton kinetic energy, $T_p$. It is first fitted as a function of $x = \log(E[\mathrm{GeV}])$ for each simulated proton kinetic energy. The formula describing $a_1$ is

$$a_1(x) = \begin{cases} a_{10} \exp\left(-a_{11}(x + a_{12})^2\right) & x \leq -0.75 \\ a_{13}(x + 0.75) + a_{14} & x > -0.75 \end{cases} \tag{5.27}$$

The parameters $a_{1i}$ $(i = 0, \ldots, 4)$ are then given by functions of the proton kinetic energy, which are listed in Table C.9.

For the baryon resonance components $\Delta\sigma/\Delta p_t^2$ will not follow the exponential form. Instead, $F(p_t, x)$ is fitted to a Gaussian form

$$F_{\Delta(1232)}(p_t, x) = b_0 \exp\left(-\frac{(p_t - b_1)^2}{b_2}\right) \tag{5.28}$$

and

$$F_{\rm res(1600)}(p_t, x) = c_0 \exp\left(-\frac{(p_t - c_1)^2}{c_2}\right) \tag{5.29}$$

With the requirement that the integral over $p_t$ should recover the inclusive cross section (eq. 5.24)

$$b_0 = 2(b_1\sqrt{\pi b_2}(\mathrm{erf}(b_1/\sqrt{b_2}) + 1) + b_2 \exp(-b_1^2/b_2))^{-1} \frac{\Delta\sigma}{\Delta\log(E)} \tag{5.30}$$

and

$$c_0 = 2(c_1\sqrt{\pi c_2}(\mathrm{erf}(c_1/\sqrt{c_2}) + 1) + c_2 \exp(-c_1^2/c_2))^{-1} \frac{\Delta\sigma}{\Delta \log(E)} \tag{5.31}$$

Again, the parameters $b_i$ and $c_i$ $(i = 1, 2)$ are functions of both $E$ and $T_p$ and the same procedure is followed for them, with

$$b_i(x) = b_{i0} \exp\left(-b_{i1}\left(\frac{x - b_{i2}}{1.0 + b_{i3}(x - b_{i2})}\right)^2\right) \tag{5.32}$$

and

$$c_i(x) = c_{i0} \exp\left(-c_{i1}\left(\frac{x - c_{i2}}{1.0 + c_{i3}(x - c_{i2})}\right)^2\right) \tag{5.33}$$

for $x < 0.5$ and $b_i(x) = 0$ for $x \geq x_b$ and $c_i(x) = 0$ for $x \geq x_c$, with

$$x_b = 0.81(y + 3.32) - 0.5 \tag{5.34}$$

$$x_c = 0.82(y + 3.17) - 0.25 \tag{5.35}$$

where $y = \log(T_p[\mathrm{TeV}])$. These limits of $b_i$ and $c_i$ were introduced to control artifacts near the kinematics limits. The parameters $b_{ij}$ and $c_{ij}$ $(j = 0, \ldots, 4)$ are listed in Table C.9 as functions of the proton kinetic energy.

Figures 5.7, 5.8 and 5.9 show the gamma-ray differential cross section $\Delta\sigma/\Delta p_t$ for the non-resonance contribution calculated using the above described parameterization for proton kinetic energies $T_p = 64$ TeV and 8 TeV and gamma-ray energies $E = 1$ GeV, 100 GeV and 1 TeV. The plots show how the average transverse momentum, $\langle p_t \rangle$, increases with increasing gamma-ray energy. Figure 5.10 shows $\Delta\sigma/\Delta p_t$ for the two resonance contributions, $\Delta(1232)$ and res(1600), calculated at proton kinetic energy $T_p = 0.82$ GeV and gamma-ray energy $E = 0.3$ GeV. Superimposed in all figures are the differential cross sections from the Monte Carlo simulations. The agreement is in general good except near the higher and lower kinematics limits where low statistics in the Monte Carlo simulations limits accuracy of the fit.

### 5.3.1 Pencil Beam Gamma-Ray Spectra

The gamma-ray spectra due to a beam of protons along the z-axis with no spatial extension in the x-y plane, i.e. a pencil beam, have been calculated using the parameterized model. The differential gamma-ray flux is given by

$$\frac{dF}{dE} = \int J_p(T_p) dT_p \int \frac{d\sigma(T_p, E, \theta)}{dE} d\theta \tag{5.36}$$

where $J_p$ is the proton spectrum in the beam and $\theta$ is the angle between the observer and the proton beam. The spectra are integrated over the annular portion

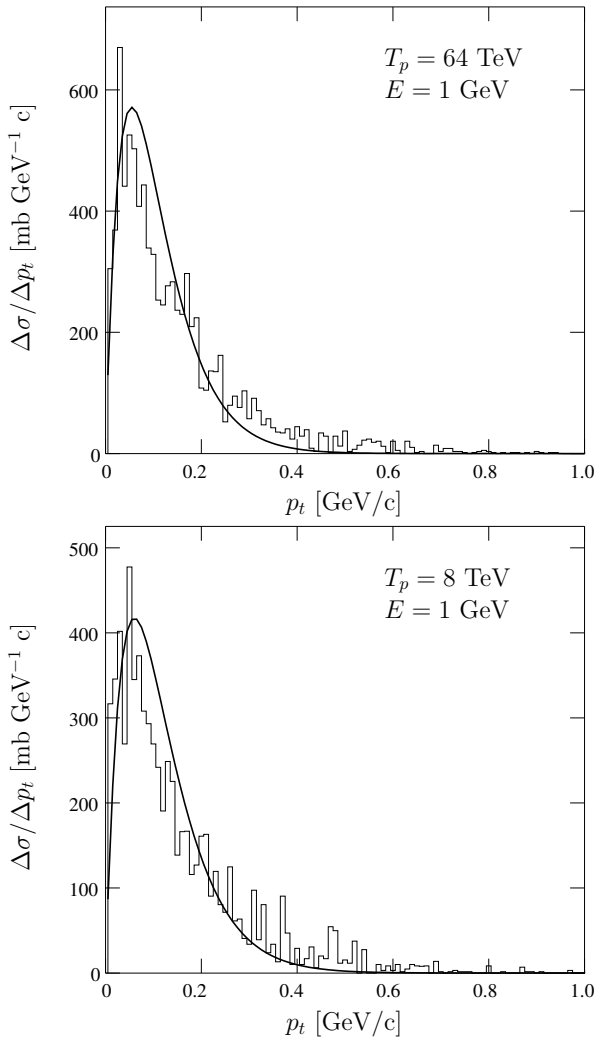


**Figure 5.7:** Gamma-ray differential cross section $\Delta\sigma/\Delta p_t$ for the non-resonance contribution at $E = 1$ GeV calculated using the parameterization (thick solid line) and superimposed with the Monte Carlo simulated cross section (thin histogram). Upper panel is for proton kinetic energy $T_p = 64$ TeV and bottom panel is for $T_p = 8$ TeV.

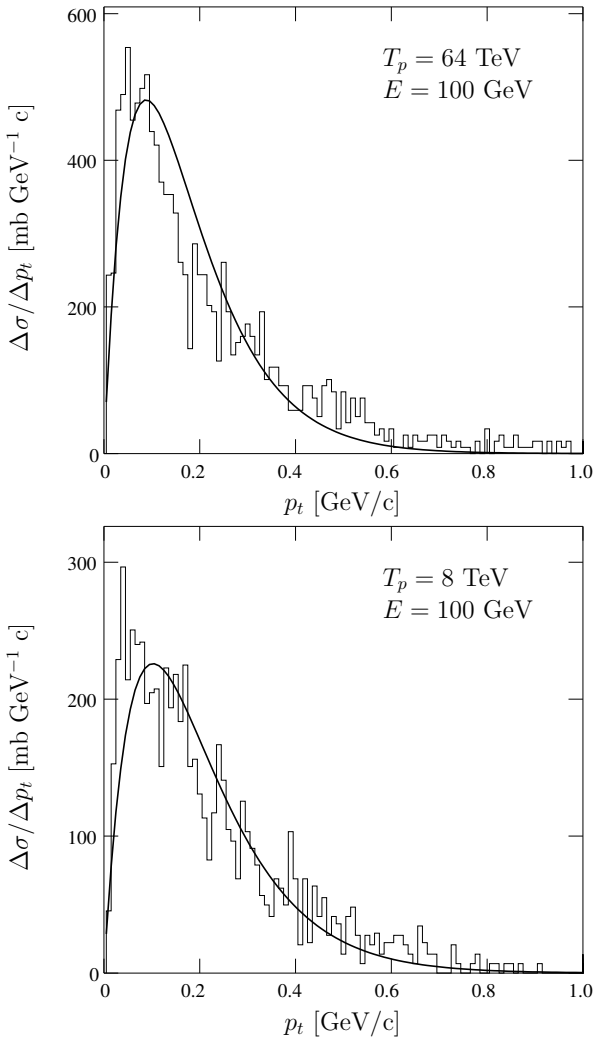


**Figure 5.8:** Gamma-ray differential cross section $\Delta\sigma/\Delta p_t$ for the non-resonance contribution at $E = 100$ GeV calculated using the parameterization (thick solid line) and superimposed with the Monte Carlo simulated cross section (thin histogram). Upper panel is for proton kinetic energy $T_p = 64$ TeV and bottom panel is for $T_p = 8$ TeV.

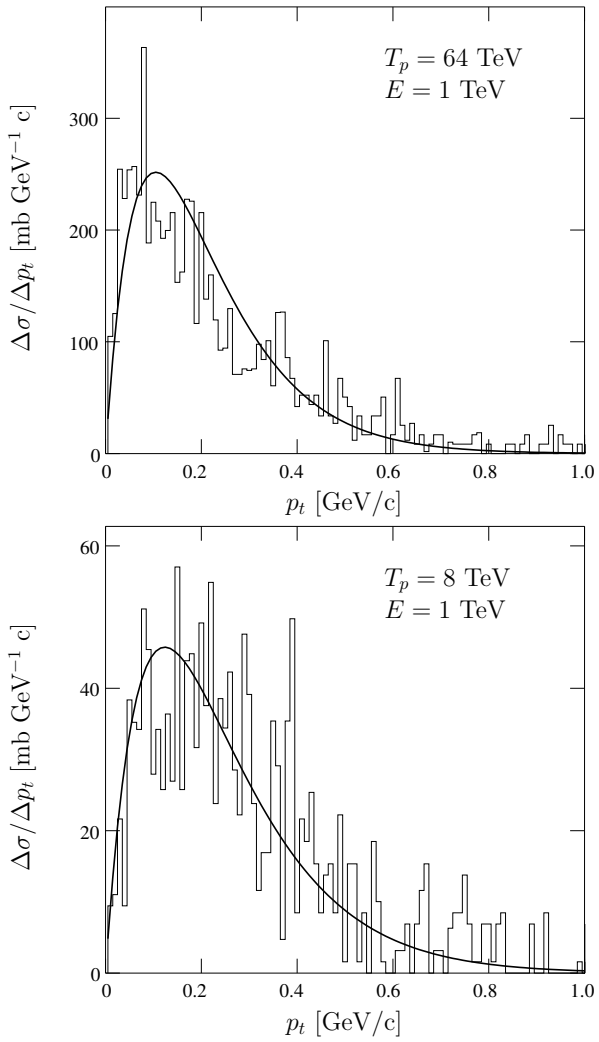


**Figure 5.9:** Gamma-ray differential cross section $\Delta\sigma/\Delta p_t$ for the non-resonance contribution at $E = 1$ TeV calculated using the parameterization (thick solid line) and superimposed with the Monte Carlo simulated cross section (thin histogram). Upper panel is for proton kinetic energy $T_p = 64$ TeV and bottom panel is for $T_p = 8$ TeV.

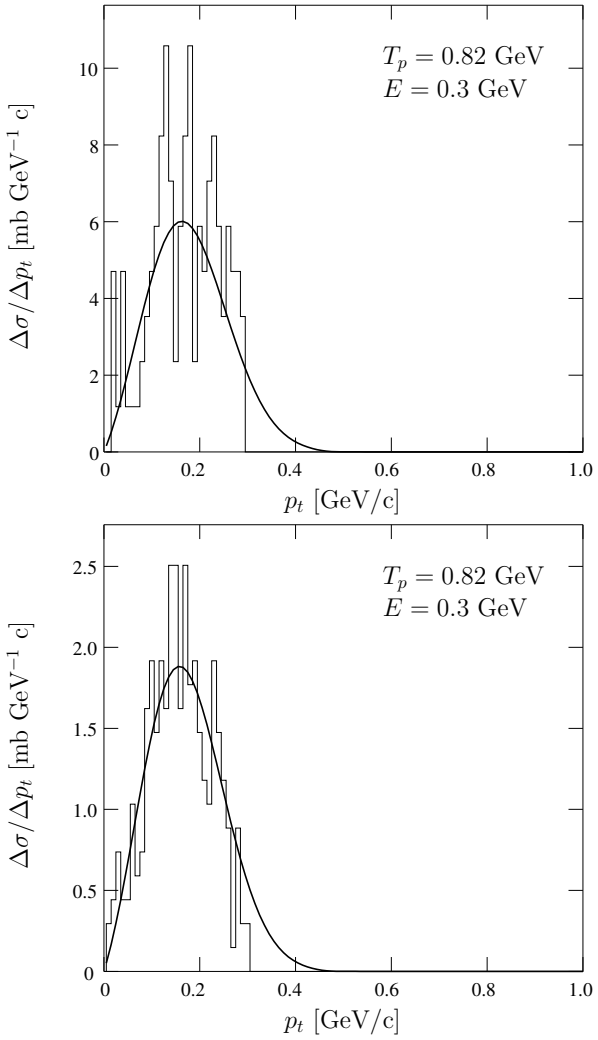


**Figure 5.10:** Gamma-ray differential cross section $\Delta\sigma/\Delta p_t$ for the two resonance contributions, $\Delta(1232)$ and res(1600), calculated using the parameterization (thick solid line) and superimposed with the Monte Carlo simulated cross section (thin histogram) for proton kinetic energy $T_p = 0.82$ GeV and $E = 0.3$ GeV. The top panel is for for the $\Delta(1232)$ resonance and the bottom panel is for the res(1600) resonance.

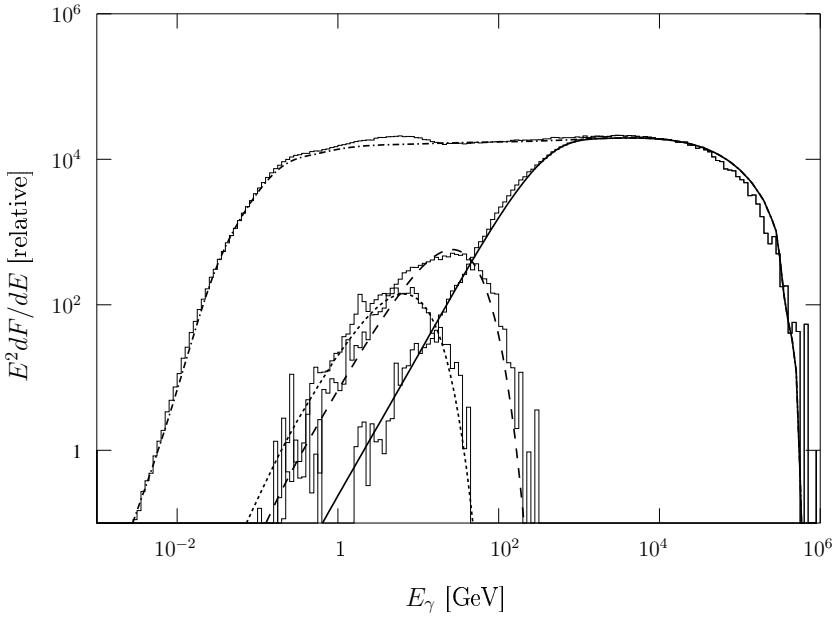


**Figure 5.11:** Gamma-ray spectra from a pencil beam of protons observed from three different angles, $\theta = 0^\circ$ (solid), $0^\circ\!.5$ (dashed), and $2^\circ$ (dotted) calculated using the parametric model. The spectra are integrated over the annular portion $(\theta, \theta + \Delta\theta)$ of width $\Delta\theta = 2'$. Included is also the spectrum integrated over the entire phase space (dash-dotted). Histograms are the corresponding Monte Carlo spectra. The protons in the beam are assumed to follow a power law in kinetic energy, $T_p$, with index 2.0 and extending up to $T_p = 512$ TeV. Fluctuations in the histograms are due to low event statistics

$(\theta, \theta + \Delta\theta)$ of width $\Delta\theta = 2'$. The energy distribution of protons in the beam is assumed to be a power law

$$J_p(T_p) = T_p^{-s} \tag{5.37}$$

with index $\Gamma = 2.0$ and extending up to $T_p = 512$ TeV. The resulting spectra are shown in Figure 5.11. The gamma-ray spectrum, $E^2dF/dE$, has been calculated for three different observation angles $\theta = 0^\circ$ (head on), $0^\circ\!.5$, and $2^\circ$ relative to the beam axis. The absolute normalization is relative to the density and distribution of target protons. For comparison the spectrum integrated over the entire phase space is also plotted in the figure. As can be seen in the figure, the gamma-ray emission is peaked in the very forward direction. When the viewing angle is increased, the peak of the spectrum is shifted to lower gamma-ray energies and the the flux decreases rapidly. Fluctuations in the histograms are due to low event statistics.

# Chapter 6

# Applications in Astrophysics

A parametric model for the inclusive cross sections of all stable secondary particles - gamma rays, $e^{\pm}, \nu_e, \bar{\nu}_e, \nu_\mu$ and $\bar{\nu}_\mu$ - and the transverse momentum distributions of gamma rays was presented in the previous chapter. This model is based on Monte Carlo simulations of the proton-proton interaction model described in Chapter 4. This interaction model addresses several short-comings of previously proposed and widely accepted models. It includes violation of the Feynman-scaling hypothesis, diffraction dissociation and a logarithmically increasing inelastic cross section. The parameterization provides an accurate description of the underlying interaction model and facilitates accurate and fast calculations in astrophysical applications.

The astrophysical applications of the presented model are plentiful and the model will be very valuable for analysis of gamma-ray sources such as active galactic nucleus (AGN) jets, gamma-ray bursts (GRB), supernova remnants (SNRs), local galaxies and molecular clouds. The inclusive cross sections are applicable in cases where the distribution of protons is expected to be isotropic. The Galactic diffuse background and extended sources, such as local galaxies and supernova remnants, are typical examples. Conversely, if the proton distribution is anisotropic, the gamma-ray flux and spectrum depends on the angle of the proton direction relative to the line of sight. Objects that fall into this category include AGN jets and GRBs, but some SNRs may also fall into this category depending on the morphology of the remnant. The highest-energy cosmic rays (CRs) escape the forward shock almost unidirectionally, resulting in a beaming effect in SNRs.

In this chapter, the use of this model is demonstrated with three different example applications of the above mentioned scenarios. In the first example, the pion-decay component of the Galactic diffuse emission is investigated with the proposed proton-proton interaction model. The second example is the study of an extended source, the Large Magellanic Cloud (LMC). The cosmic-ray flux and spectrum is estimated using the model together with EGRET observations of gamma rays and current HI and CO column densities in the LMC. The third and final example shows the gamma-ray spectrum for a toy model proton jet. The protons accelerated by

the jet have anisotropic momentum distributions; the jet is fanned with a Gaussian intensity profile centered on the jet axis. Gamma-ray spectra have been calculated for different viewing angles relative to the jet axis.

## 6.1 Galactic Diffuse Emission

The Galactic diffuse emission is dominated by gamma rays from decays of neutral pions produced in interactions between cosmic rays and interstellar matter (ISM; Stecker, 1973, 1989; Strong et al., 1978, 1982, 2000, 2004; Stephens & Badhwar, 1981; Dermer, 1986a; Hunter et al., 1997) and Compton up-scattering of low-energy photons on ultra-relativistic electrons (Murthy & Wolfendale, 1986; Schönfelder, 2001; Strong et al., 2000, 2004). There is also a non-negligable contribution from electron and positron bremsstrahlung in the interstellar matter. Each of these processes dominates in different parts of the spectrum and in different regions in the sky. Therefore, the observed gamma-ray spectrum can provide information about both the spectrum of cosmic rays and the matter distribution in the Galaxy.

The EGRET instrument on board the CGRO satellite provided the first all-sky gamma-ray survey. The observed diffuse gamma-ray spectrum shows an excess over model predictions above 1 GeV (Hunter et al., 1997), as illustrated in Figure 6.1 for three different regions of the Galaxy. The excess has long been a topic of great debate and several attempts at explaining it have been made; including re-evaluation of the neutral pion production component and the underlying proton-proton interactions, redefining the spectra of cosmic rays and electrons and also exotic new physics such as dark matter.

The effects on the gamma-ray spectrum due to incorrect modeling of the proton-proton interaction were investigated by Kamae et al. (2005). They claimed to be able to reproduce about 50% of the excess with the new proton-proton interaction model that includes violation of Feynman scaling, diffraction dissociation and a logarithmically increasing inelastic proton-proton cross section. This claim is contingent on the normalization between the different models and between models and EGRET data. The new pion decay model was normalized to the Galprop model in the energy range $E < 300$ MeV, where the gamma-ray spectrum due to $\pi^0$ decays becomes insensitive to the incident proton spectrum. The EGRET data were normalized such that the average of the two bins covering 150-300 MeV and 300-500 MeV agreed with the new model predictions. Figure 6.2 shows their model spectrum compared with the EGRET data, normalized as described. The spectrum calculated based on the local interstellar proton spectrum (LIS) explains about 50% of the excess and the spectrum calculated with their broken power-law proton spectrum (the spectrum has break at 20 GeV and the spectral index changes from 2.2 to 2.5 at the break) is consistent with the EGRET spectrum.

When including contributions from two baryon resonances, Kamae et al. (2006) noted that the normalization used above was no longer valid. Instead they normalized the spectra in the peak region, $E = 0.7 - 0.8$ GeV, which is illustrated in Figure

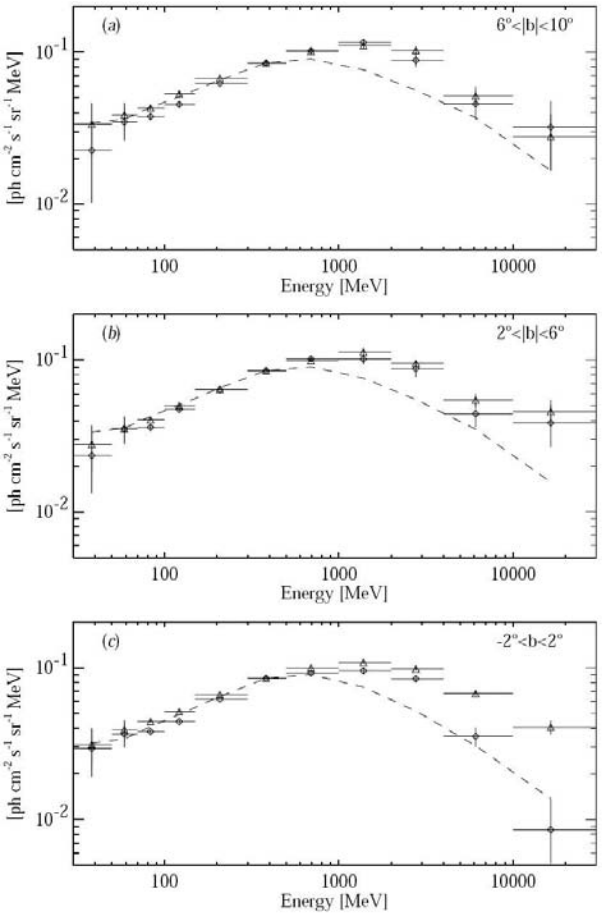


**Figure 6.1:** Comparison of average EGRET diffuse emission (contribution of point sources and the isotropic extragalactic background have been subtracted) spectra for the inner Galaxy ($315^\circ < l < 45^\circ$, triangles) and for the outer Galaxy ($135^\circ < l < 225^\circ$, diamonds). The different panels show the spectra averaged over different latitude ranges: (a) $6^\circ < |b| < 10^\circ$, (b) $2^\circ < |b| < 6^\circ$ and (c) $|b| < 2^\circ$. The dashed line is the corresponding model prediction. Figure taken from Hunter et al. (1997).

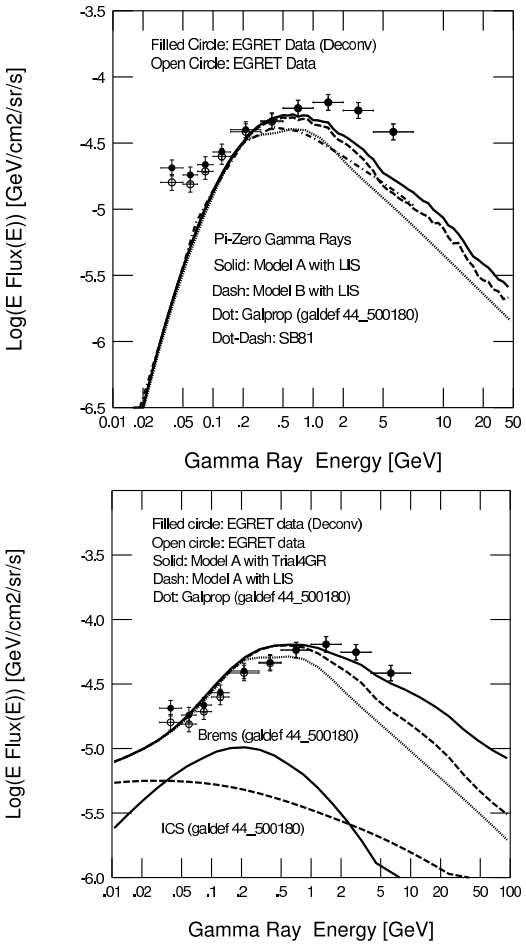


**Figure 6.2:** Diffuse emission model spectra calculated by Kamae et al. (2005) together with their point-source subtracted EGRET spectra, averaged over the Galactic ridge ($|l| < 30°$, $|b| < 6°$). The upper panel is for $\pi^0$ contribution only and bottom panel is for the total gamma-ray spectrum including bremsstrahlung and Compton up-scattering (IC) contributions. The mutal normalization described in the text is shown in the upper panel. LIS is the local interstellar proton spectrum, Trial4GR is a broken power-law spectrum (break at 20 GeV and the spectral index changes from 2.2 to 2.5 at the break) and SB81 is the model by Stephens & Badhwar (1981). Data points are for point spread function (PSF) deconvolved EGRET spectrum (filled circles) and EGRET spectrum (open circles). The PSF deconvolution is described in and figures taken from Kamae et al. (2005).

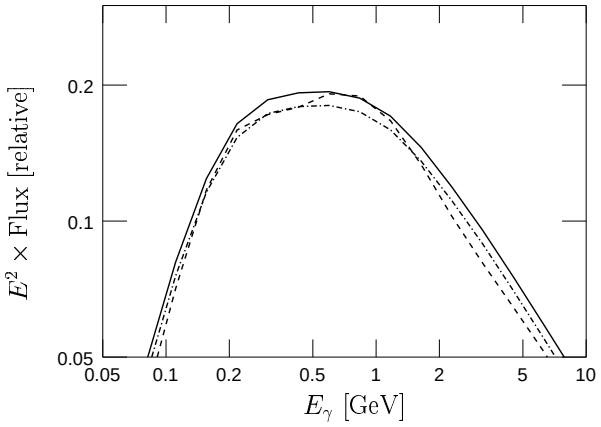


**Figure 6.3:** Pion decay gamma-ray spectra calculated with Galprop using both the built-in proton-proton interaction model (dashed) and the present parametric model (dash-dotted). The solid line is the dash-dotted line normalized to the dashed one in the energy band $E = 0.7 - 0.8$ GeV. Figure taken from Kamae et al. (2006).

6.3. With this normalization the new model gives about 20% higher gamma-ray yield than the Galprop scaling model, which is substantially lower than the 50% claimed by Kamae et al. (2005).

### 6.1.1 Galprop

Galprop, developed by Strong and Moskalenko (Strong & Moskalenko, 1998; Strong et al., 2000, 2004, 2007)[1], is a numerical simulation code for cosmic-ray acceleration and propagation in a model galaxy. It solves the transport equation in either 2D or full 3D for given source distribution and boundary conditions for all cosmic-ray species, nucleonic and leptonic. In doing this it takes into account convection in Galactic winds, diffusive reacceleration in the interstellar medium, energy losses and nuclear fragmentation and decays. Therefore it is possible to calculate the spatial distribution and spectrum of any given secondary particle, including gamma rays and radio isotopes.

Galprop provides two major models for calculating the diffuse gamma-ray emission. The conventional model (Strong et al., 2004) assumes the spectra of protons, He and electrons to match the locally observed ones. It is the same model as in Strong et al. (2000), but with updated nucleon spectra. The model includes secondary electrons and positrons and uses improved gas distribution data. The discrepancy in GeV energies between EGRET data and the conventional model is

[1] For more on Galprop, see http://galprop.stanford.edu/web_galprop/galprop_home.html

very clear and the excess can be seen in any direction of the sky. Strong et al. (2004) found that a simple rescaling of the $\pi^0$ component cannot be used to reproduce the excess consistently.

They also proposed Galprop models where the injection spectrum of nucleons and electrons are adjusted independently to reproduce the observed gamma-ray spectrum. It was concluded that a model with a much harder electron spectrum alone is not tenable. In the light of this, Strong et al. (2004) used the observed diffuse gamma-rays themselves to obtain an optimized model. The optimized model adjusts the electron injection spectrum enough to explain the observed gamma-ray spectrum. The optimized electron spectrum has a break at 20 GeV where the power-law index changes from 1.50 to 2.42; the conventional electron spectrum has a break at 10 GeV and the index changes from 1.60 to 2.54. This adjustment of the spectral shape also requires adjustments of the normalization of both the electron and proton injection spectra. The electron spectrum is normalized upward by a factor 4 and the proton spectrum is normalized upward by a factor of 1.8. Figures 6.4 and 6.5 show the difference between the conventional and optimized injection spectra for protons and electrons respectively and also compares them with data for the local cosmic-ray spectra from several cosmic-ray experiments. For a complete description of the two models, the reader is referred to Strong et al. (2004).

### 6.1.2 EGRET Observations

The EGRET data from observation cycles 1-4 are publically available for download at NASA's High Energy Astrophysics Science Archive Research Center (HEASARC)[2] as photon count, instrument exposure and intensity maps. Each of them is divided into 10 energy bands, from 30 MeV to 10 GeV, with a pixel size of $0.5^\circ \times 0.5^\circ$. The gamma-ray intensity in a given pixel is the photon count divided by the exposure.

The photon count and intensity maps available contain all point sources of the third EGRET (3EG) catalog (Hartman et al., 1999). For analysis of the diffuse emission those point sources have to be subtracted from the photon count map. This has been done using the EGRET point-spread function (PSF) for each energy band (Cillis & Hartman, 2005). The flux of each point source was determined using EGRET likelihood programs. To minimize the photon statistical noise the maps were smoothed with a Gaussian. The intensity maps for the diffuse emission are also publically available in the EGRET archive at HEASARC.

The gamma-ray spectrum has been calculated from the diffuse maps in three different regions of the Galaxy; the inner Galaxy, the Galactic plane excluding the inner Galaxy and the outer Galaxy, as described in Table 6.1. The intensity of gamma rays in each energy band is the sum over the pixels in each region normalized to per unit solid angle and they are tabulated in Table 6.2. Based on the photon counts in each energy band, the statistical error is estimated to about 5%. The systematic error associated with the EGRET spectra is assumed to be $\pm 15\%$

[2]See http://cossc.gsfc.nasa.gov/docs/cgro/egret

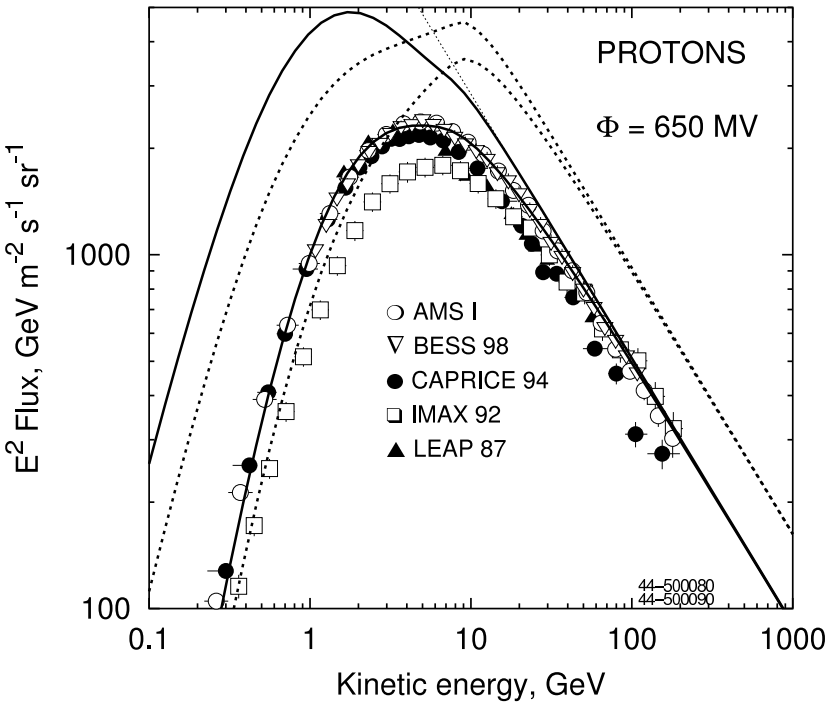


**Figure 6.4:** Proton injection spectra obtained with Galprop for the conventional (solid) and optimized (dashed) models. The upper curves are for the local interstellar spectrum (LIS) and the lower curve is modulated to $\Phi = 650$ MV. The thin dotted line is the LIS spectrum best fit to the data above 20 GeV (Moskalenko et al., 2002). Data points are: AMS (Alcaraz et al., 2000a), BESS 98 (Sanuki et al., 2000), CAPRICE 94 (Boetzio et al., 1999), IMAX 92 (Menn et al., 2000), LEAP 87 (Seo et al., 1991). Figure taken from Strong et al. (2004).

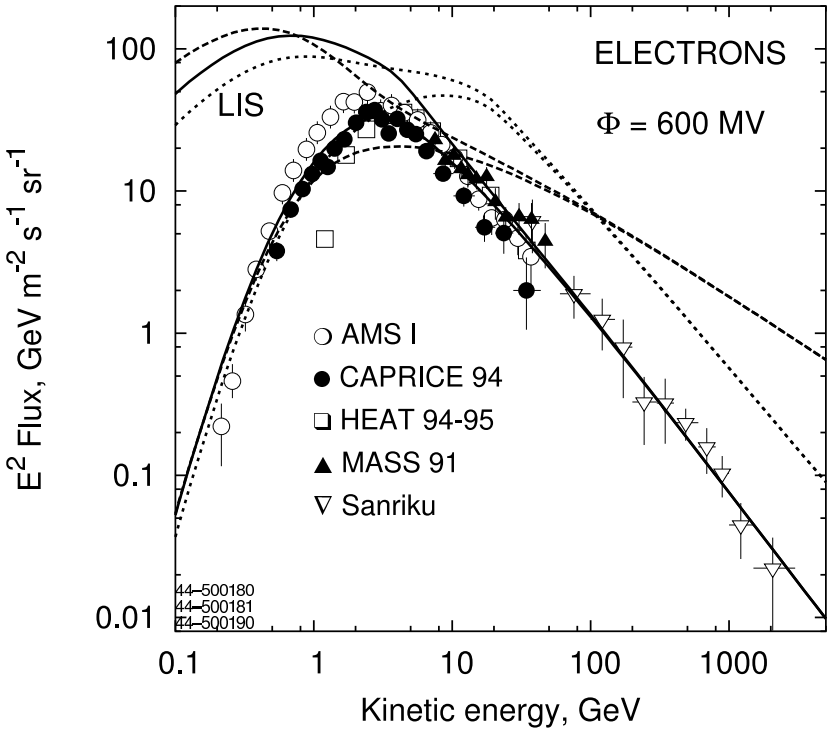


**Figure 6.5:** Electron injection spectra obtained with Galprop for the conventional (solid), hard electron spectrum (dashed) and optimized (dotted) model. The upper curves are for the local interstellar spectrum (LIS) and the lower curve is modulated to $\Phi = 600$ MV. Data points are: AMS (Alcaraz et al., 2000b), CAPRICE 98 (Boetzio et al., 2000), HEAT 94-95 (DuVernois et al., 2001), MASS 91 (Grimani et al., 2002) and Sanriku (Kobayashi et al., 1999). Figure taken from Strong et al. (2004).

**Table 6.1:** Definitions of Galaxy regions for the Galactic diffuse emission analysis

| Region | $l$ deg[a] | $\|b\|$ deg[b] |
|---|---|---|
| Inner Galaxy | 300-30 | 0-5 |
| Galactic plane (avoiding the inner Galaxy) | 30-330 | 0-5 |
| Outer Galaxy | 90-270 | 0-10 |

[a] Galactic longitude, $0 \leq l \leq 360$

[b] Galactic latitude, $-90 \leq b \leq 90$

(Kamae et al., 2005; Strong et al., 2000). The diffuse gamma-ray spectrum has been verified to be consistent with those of Strong et al. (2004) and Kamae et al. (2005).

### 6.1.3 Gamma-ray Spectra

For this work, the parametric model for inclusive cross sections of gamma-rays, electrons and positrons given in the previous chapter has been incorporated into the Galprop code. Galprop was used to calculate model spectra of diffuse emission in the same regions of the Galaxy as mentioned above; see Table 6.1. The calculations were made for both the conventional and the optimized Galprop model and with both the scaling model and the present *pp* interaction model, i.e. in total four calculations per region. The Galprop model spectra were then compared with each other as well as with the corresponding spectra calculated from EGRET diffuse maps. Figure 6.6, 6.7 and 6.8 show the Galprop model spectra together with the EGRET spectra for the inner Galaxy, Galactic plane and outer Galaxy respectively.

The optimized model is clearly a better fit to the EGRET data, both with the present *pp* interaction model and the Galprop scaling model, than the conventional model. The optimized model only barely matches the EGRET data point at 7 GeV in all regions. The intensity at this energy calculated using the public EGRET diffuse maps is slightly higher than that calculated by Strong et al. (2004), but the error bar is large enough to allow consitancy between the two values.

The present model gives a smoother and flatter spectral energy distribution between $E = 0.3 - 2$ GeV and a slightly higher gamma-ray yield above $E = 1.5$ GeV. The difference in pion-decay spectrum between the scaling model and the present model is here even smaller than predicted by Kamae et al. (2006). It is on the order of 5%. Since both models are properly implemented in the Galprop code, no normalization between the models has been made. The difference of 20% claimed by Kamae et al. (2006) can be attributed to their normalization between the models. Even though the difference has been reduce significantly, the *pp* interaction model proposed here is still valuable.

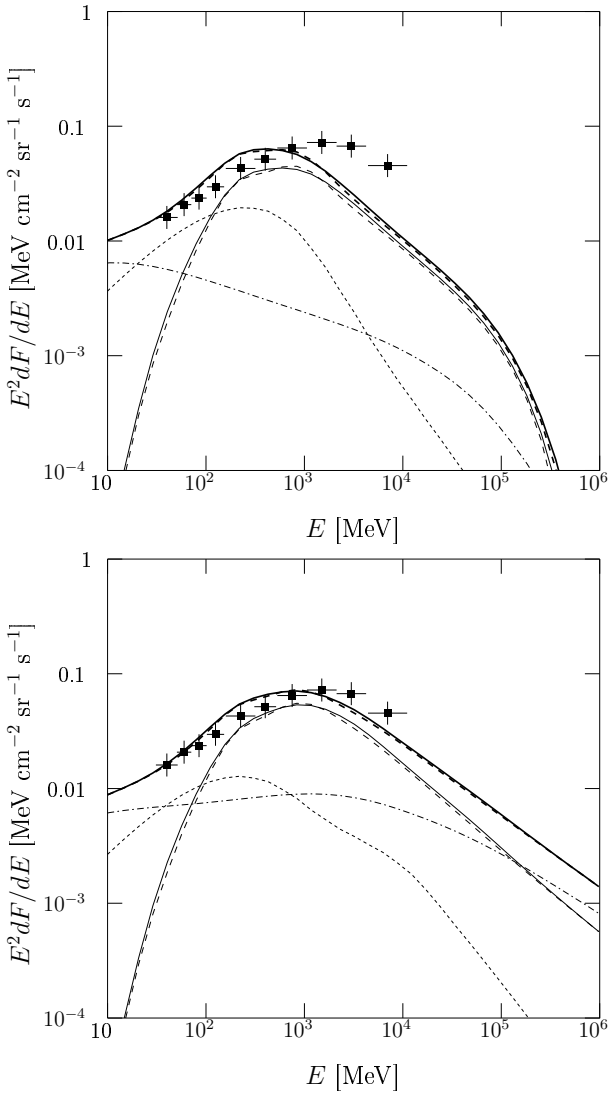


**Figure 6.6:** Gamma-ray spectrum in the inner Galaxy calculated by Galprop with the "conventional" model (galdef ID 52_599278; top panel) and the "optimized" model (galdef ID 500190; bottom panel) for both the new *pp* interaction model (solid) and the Galprop scaling model (dashed). The thick lines are the total and the thin lines are the pion decay component. Shown are also the Compton up-scattering (dash-dotted) and bremsstrahlung (dotted) components. Data points are calculated from the public EGRET diffuse maps (Cillis & Hartman, 2005).

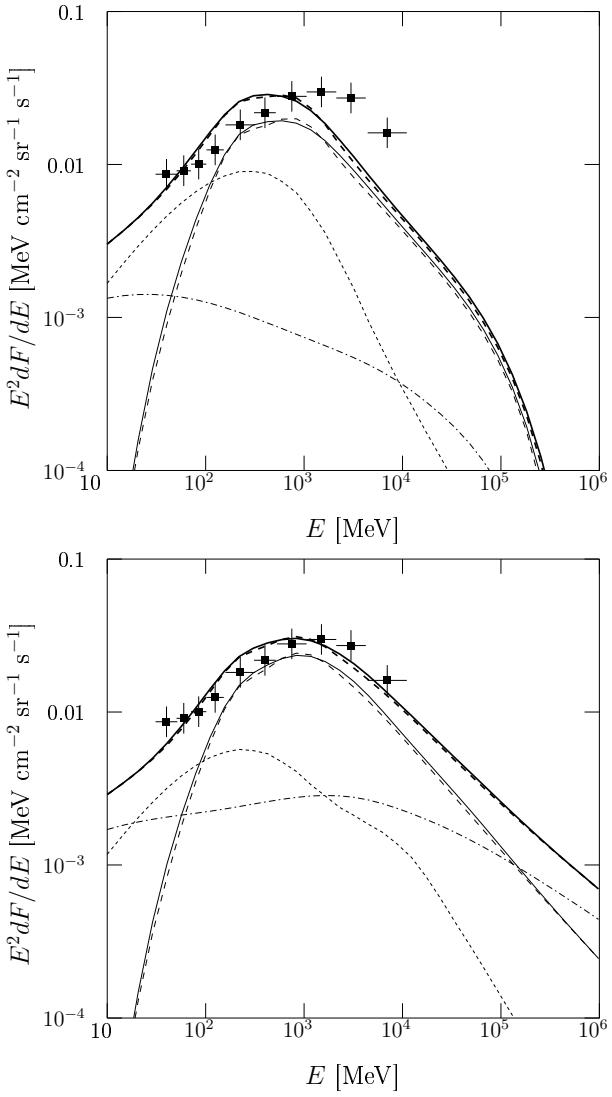


**Figure 6.7:** Gamma-ray spectrum in the Galactic plane (avoiding the inner Galaxy) calculated by Galprop with the "conventional" model (galdef ID 52_599278; top panel) and the "optimized" model (galdef ID 500190; bottom panel) for both the new *pp* interaction model (solid) and the Galprop scaling model (dashed). The thick lines are the total and the thin lines are the pion decay component. Shown are also the Compton up-scattering (dash-dotted) and bremsstrahlung (dottedd) components. Data points are calculated from the public EGRET diffuse maps (Cillis & Hartman, 2005).

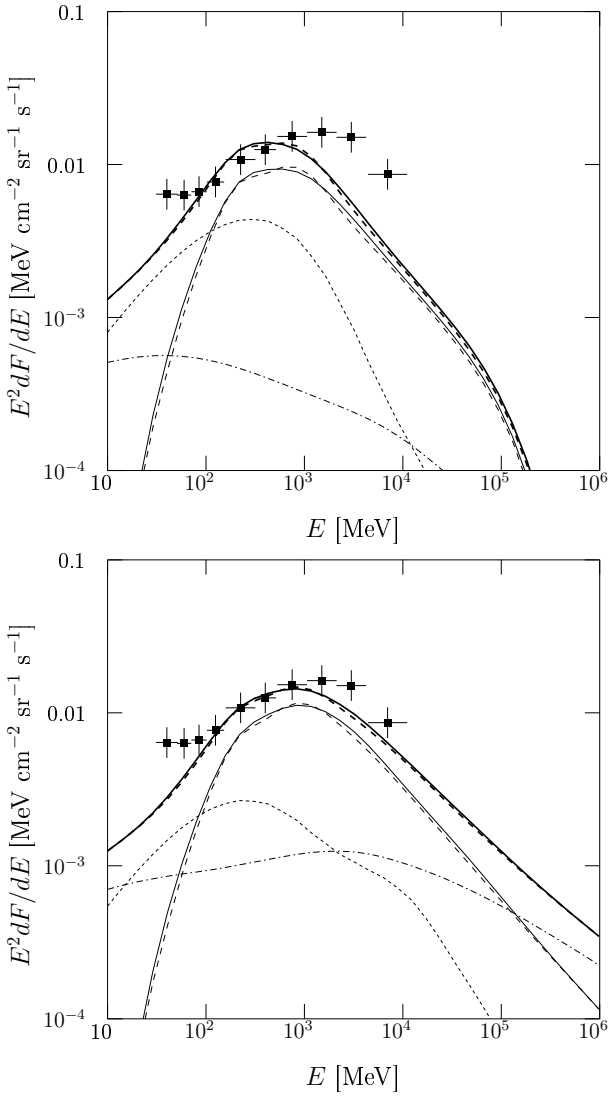


**Figure 6.8:** Gamma-ray spectrum in the outer Galaxy calculated by Galprop with the "conventional" model (galdef ID 52_599278; top panel) and the "optimized" model (galdef ID 500190; bottom panel) for both the new *pp* interaction model (solid) and the Galprop scaling model (dashed). The thick lines are the total and the thin lines are the pion decay component. Shown are also the Compton up-scattering (dash-dotted) and bremsstrahlung (dotted) components. Data points are calculated from the public EGRET diffuse maps (Cillis & Hartman, 2005).

**Table 6.2:** EGRET spectra in different regions of the Galaxy

| Energy range [MeV] | $E^2dF/dE$ [a] [MeV cm$^{-2}$ sr$^{-1}$ s$^{-1}$] | | |
|---|---|---|---|
| | Inner Galaxy | Galactic plane | Outer Galaxy |
| 30-50 | 0.016 | 0.0086 | 0.0064 |
| 50-70 | 0.021 | 0.0091 | 0.0063 |
| 70-100 | 0.024 | 0.010 | 0.0066 |
| 100-150 | 0.030 | 0.012 | 0.0077 |
| 150-300 | 0.043 | 0.018 | 0.011 |
| 300-500 | 0.052 | 0.022 | 0.013 |
| 500-1000 | 0.065 | 0.028 | 0.015 |
| 1000-2000 | 0.072 | 0.030 | 0.016 |
| 2000-4000 | 0.067 | 0.027 | 0.015 |
| 4000-10000 | 0.045 | 0.016 | 0.0086 |

[a] The statistical error is about 5% based on the photon counts.

## 6.2 Large Magellanic Cloud

Galaxies with gaseous matter densities and cosmic-ray content similar to our Galaxy may also produce diffuse gamma rays. Such galaxies could be detectable as dim extended sources. Because of the low luminosity of such diffuse emission, external galaxies must be close-by to be detectable. The Large Magellanic Cloud (LMC) was the only external galaxy detected by the EGRET instrument (Sreekumar et al., 1992). It is an irregular dwarf galaxy orbiting the Galaxy and is the nearest galaxy neighbor after the Sagittarius dwarf elliptical galaxy. The LMC is located in the southern hemisphere, $l = 280°, b = -32.9°$,[3] at a distance of about 50 kpc from the Earth (Macri et al., 2006). Its apparent dimensions on the sky is about $650' \times 550'$. The proximity to the Milky Way and the EGRET detection makes the LMC a prime candidate for investigating cosmic-ray distributions using gamma-ray observations.

### 6.2.1 EGRET Observation

EGRET measured the integrated flux over the entire LMC above 100 MeV to be $(1.9 \pm 0.4) \times 10^{-7}$ photons cm$^{-2}$ s$^{-1}$ (Sreekumar et al., 1992). In the third EGRET catalog (3EG), LMC is listed as a point-source detection with a flux above 100 MeV of $(14.2 \pm 2.2) \times 10^{-8}$ photons cm$^{-2}$ s$^{-1}$ and the spectrum is a power law

$$\frac{dF}{dE} \propto E^{-\Gamma} \tag{6.1}$$

[3] Given as Galactic coordinates, taken from the NASA/IPAC Extragalactic Database.

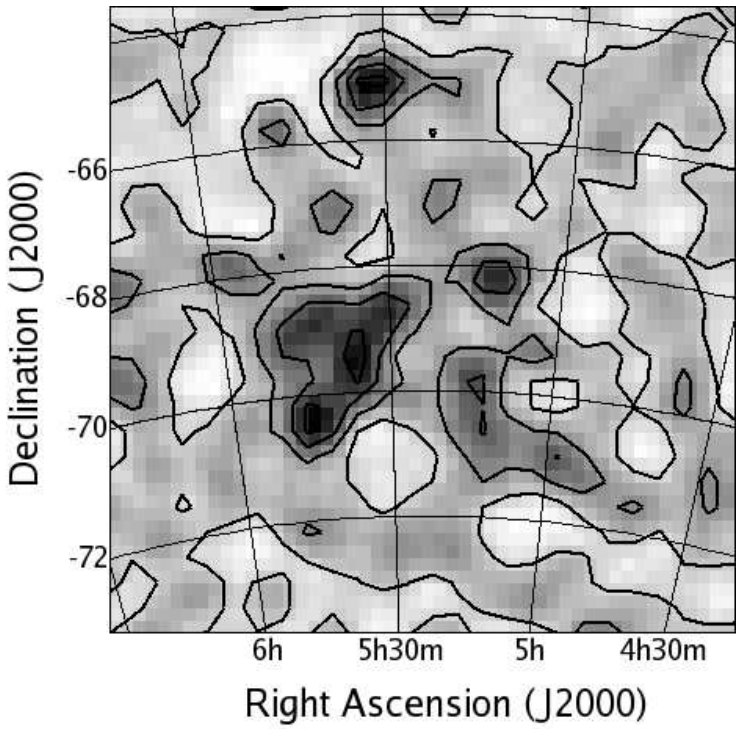


**Figure 6.9:** EGRET image of the LMC in equatorial coordinates. The 3EG point source is at right ascension 5h33m40s and declination $-69°16'$. The blob in the central part of the image is the feature picked up as the 3EG point source.

with power-law index $\Gamma = 2.20 \pm 0.20$ (Hartman et al., 1999). The EGRET image of the LMC is shown Figure 6.9.

### 6.2.2 Matter Density

The matter density in the LMC has been well studied in both atomic hydrogen (HI) and carbon monoxide (CO). The column density of HI, shown in Figure 6.10, has been obtained from the ATCA/Parkes 21 cm survey (Kim et al., 1998, 2003).[4] The HI has been rebinned to a map covering $6° \times 6°$ with $2' \times 2'$ pixels and is centered on the EGRET location of the LMC. The column density range is from 0 to about $1.2 \times 10^{21}$ cm$^{-2}$.

[4]The Australia Telescope Compact Array (ATCA) and the Parkes telescope are part of the Australia Telescope which is funded by the Commonwealth of Australia for operation as a National Facility managed by CSIRO.

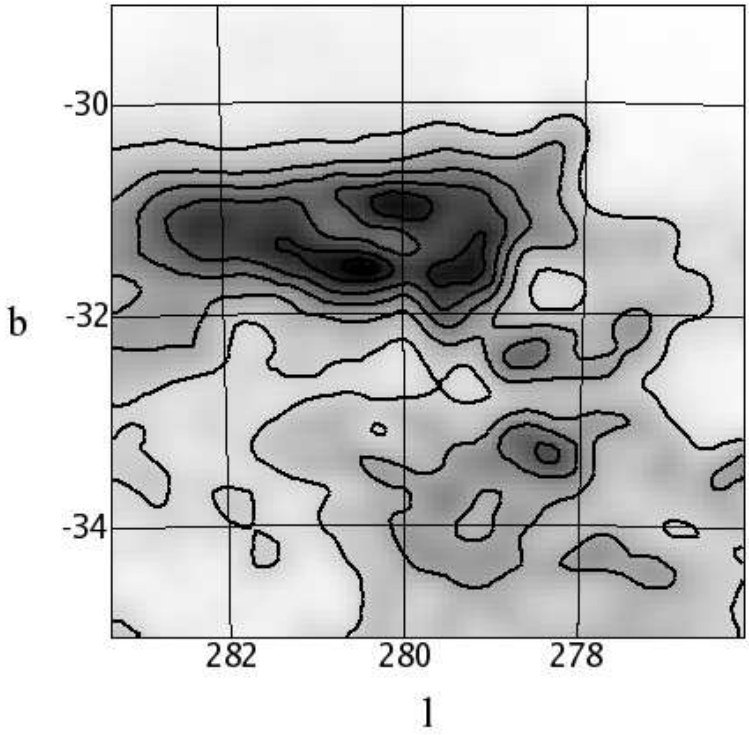


**Figure 6.10:** HI column density from the ATCA/Parkes 21 cm survey of the LMC (Kim et al., 1998, 2003). The density map, given in Galactic coordinates, covers $6^\circ \times 6^\circ$ and is centered on the EGRET location. The contours are for $(0, 2.0, 3.9, 5.8, 7.7, 9.7, 11.0) \times 10^{20}$ cm$^{-2}$.

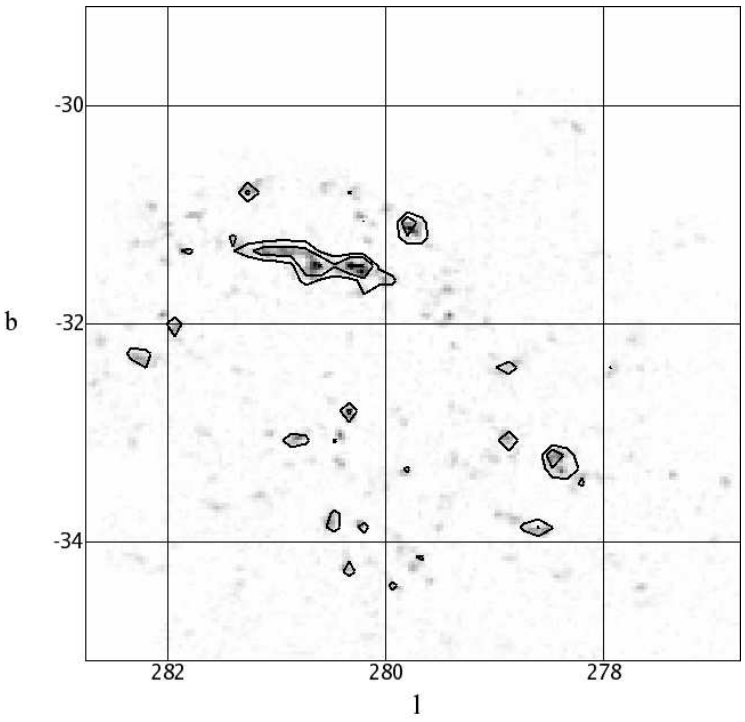


**Figure 6.11:** Velocity-integrated intensity map of $^{12}$CO($J = 1.0$) emission from the NANTEN survey of the LMC (Mizuno et al., 2001). The map, given in Galactic coordinates, covers $6^\circ \times 6^\circ$ and is centered on the EGRET location. The contours are for $(0, 1.5, 3.0, 6.0, 12.0)$ K km/s.

It is widely accepted that CO gas is a tracer of molecular hydrogen ($H_2$). Velocity-integrated intensity, $W_{\rm CO}$, can be converted to $H_2$ column density using the $X$-factor defined as

$$X = \frac{N_{\rm H_2}}{W_{\rm CO}} \tag{6.2}$$

The $X$-factor for the LMC was measured by the NANTEN team to be $X_{\rm LMC} \simeq (9 \pm 4) \times 10^{20}$ cm$^{-2}$ (K km/s)$^{-1}$ (Mizuno et al., 2001).

The total column density of protons in the LMC is estimated by

$$N_p = N_{\rm HI} + 2N_{\rm H_2} \tag{6.3}$$

It is noted that this neglects any He gas. In the Earth's vicinity, the interstellar medium contains about 10% helium. This may not be true for the LMC.

### 6.2.3 Cosmic-Ray Spectrum

Under the assumption that the cosmic-ray flux is isotropic, the differential gamma-ray flux is given by

$$\frac{dF}{dE} = \int_{\Omega} N_p d\Omega \int_{T_p} J_p(T_p) \frac{d\sigma(T_p, E)}{dE} dT_p \tag{6.4}$$

where $N_p$ is the column density of protons (HI and $H_2$), $J_p$ is the cosmic-ray spectrum as a function of the proton kinetic energy $T_p$ and $d\sigma/dE$ is the inclusive cross section as function of the proton kinetic energy $T_p$ and the gamma-ray energy $E$. The area of the sky integrated over, $\Omega$, is the $6^\circ \times 6^\circ$ covered by the density and intensity maps in Figures 6.10 and 6.11. The flux is calculated for proton energies, $T_p$, from the pion production threshold up to 512 TeV.

The column density of protons is given by equation 6.3. The differential gamma-ray flux is calculated in an iterative process. It is started with a reasonable initial guess for the cosmic-ray flux which is assumed to be a power law in proton kinetic energy

$$J_p(T_p) = n_0 T_p^{-\Gamma} \tag{6.5}$$

The spectral index of the resulting gamma-ray spectrum will only depend on the spectral index of the cosmic-ray spectrum, therefore $n_0 = 1.0$ in the initial guess. The differential gamma-ray spectrum is calculated for this guess and the spectral index is determined by fitting a straight line between $E = 0.25$ GeV and $E = 3.2$ GeV, because EGRET had very poor sensitivity above a few GeV and below a few hundred MeV bremsstrahlung and Compton up-scatterings may dominate the spectrum. The spectrum is then recalculated iteratively until the resulting index matches that of the EGRET observation. Then the normalization constant, $n_0$, is adjusted such that the total flux also matches the EGRET observation. The resulting normalization is $n_0 = (15.6 \pm 2.4) \times 10^{-8}$ cm$^{-2}$ s$^{-1}$ sr$^{-1}$ GeV$^{-1}$ and the power-law index is $\Gamma = 2.37$. The gamma-ray spectrum for this cosmic-ray flux is shown in Figure 6.12 together with the best-fit power law. From the figure it is clear that the spectrum is not a simple power law over the GLAST-LAT energy range. For a more complete treatment one must include heavier nuclei, both as target material and as cosmic rays. It is also important to include estimates of the bremsstrahlung and Compton up-scattering components.

### 6.2.4 Other External Galaxies

EGRET made upper-limit detections for a few other galaxies; Small Magellanic Cloud (SMC; Sreekumar et al., 1993), the Andromeda galaxy (M31; Sreekumar et al., 1994) and the giant radio galaxy M87 (Sreekumar et al., 1994). It is likely that these galaxies will be detected by the GLAST-LAT as extended sources alongside the LMC. The cosmic-ray distributions of these galaxies can then be investigated. According to (Blom et al., 1999), the upper limit to the gamma-ray flux above 100

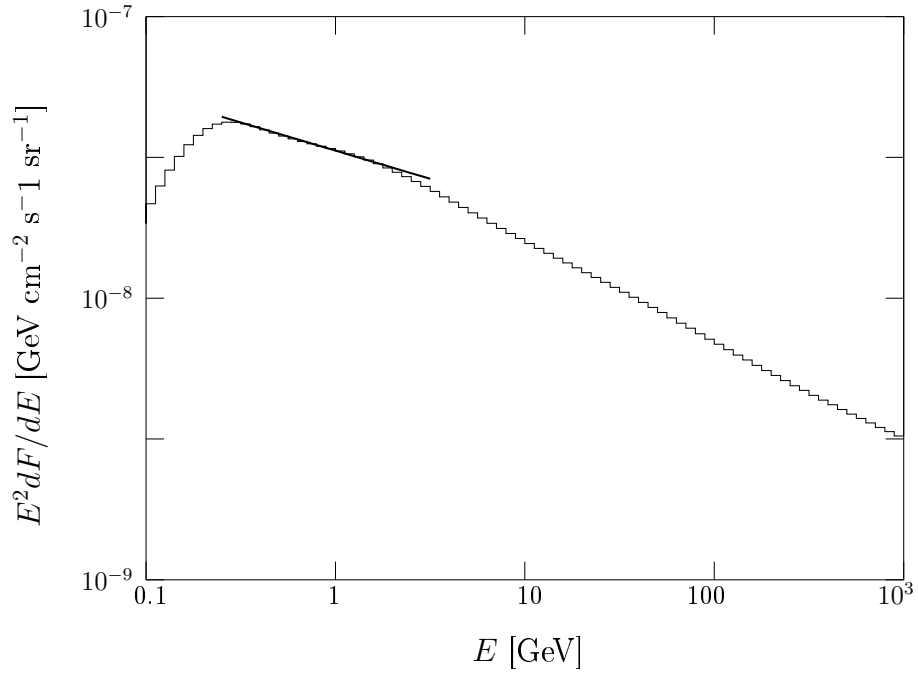


**Figure 6.12:** Gamma-ray spectrum (histogram) from the LMC calculated using the best estimate for the cosmic-ray flux under the assumption that all gamma rays detected by EGRET comes from pion decays. The matter density is taken from the 21 cm HI survey with ATCA/Parkes (Kim et al., 1998, 2003) and the NANTEN CO survey (Mizuno et al., 2001) of the LMC. The solid straight line is the best-fit power law with index 2.20 in the energy range $0.25 < E < 3.2$ GeV.

MeV for M31 is $1.6 \times 10^{-8}$ photons cm$^{-2}$ s$^{-1}$, which is much smaller than that of the Milky Way at M31. This has implications on the density of cosmic rays in M31 and further studies of it with GLAST can be very helpful for the understanding of the Milky Way. The improved angular resolution of the GLAST-LAT over EGRET will make it possible to detect structures in the gamma-ray emission from the LMC, which will make detailed cosmic-ray distribution analysis possible.

## 6.3 Fanned Proton Jet

The final example is a fanned proton jet with a Gaussian intensity profile sampled as pencil beams. The jet is assumed to have an opening angle of $10^\circ$ which corresponds to a Gaussian profile with FWHM of $3^\circ$. The predicted gamma-ray spectrum observed at a given angle $\theta$ off the jet axis is given by

$$\frac{dF}{dE} = \int I(\theta_i) d\Omega \int J_p(T_p) dT_p \int \frac{d\sigma(T_p, E, \theta)}{dE} d\theta \tag{6.6}$$

where $I$ is the intensity profile, $\theta_i$ is the angle between the jet axis and the pencil beam, $d\Omega$ is the surface element of the pencil beam, $J_p(T_p)$ is the incident proton spectrum, $\theta$ is the angle between the pencil beam and the observer and $d\sigma/dE$ is the differential cross section.

The gamma-ray spectrum from the jet is integrated over the intensity profile, which is sampled in $0.1^\circ \times 0.1^\circ$ bins and each bin is represented by the average of ten randomly sampled pencil beams pointing within the bin. The incident proton spectrum is assumed to be a power law with index $\Gamma = 2.0$, extending from the pion production threshold up to 512 TeV. For each pencil beam, the differential cross section is integrated over the annular portion $(\theta, \theta + \Delta\theta)$ with $\Delta\theta = 2'$ and then normalized to per solid angle.

The gamma-ray spectra, calculated per solid angle, observed from four different angles $\theta = 0^\circ$ (head on), $5^\circ, 10^\circ$ and $20^\circ$ are shown in Figure 6.13. The absolute normalization is here relative to the density and distribution of target protons and has been omitted for simplicity.

When the viewing angle is smaller than the opening angle of the jet, the gamma-ray spectrum features a tail extending up to the highest possible gamma-ray energy, about $10^6$ GeV, as can be seen in Figure 6.13. This highest gamma-ray energy is set by the cutoff in the incident proton spectrum at 512 TeV. The tail is suppressed for larger viewing angles because of the Gaussian intensity profile. At $\theta = 5^\circ$ the tail is about four orders of magnitud lower in flux than the head on spectrum.

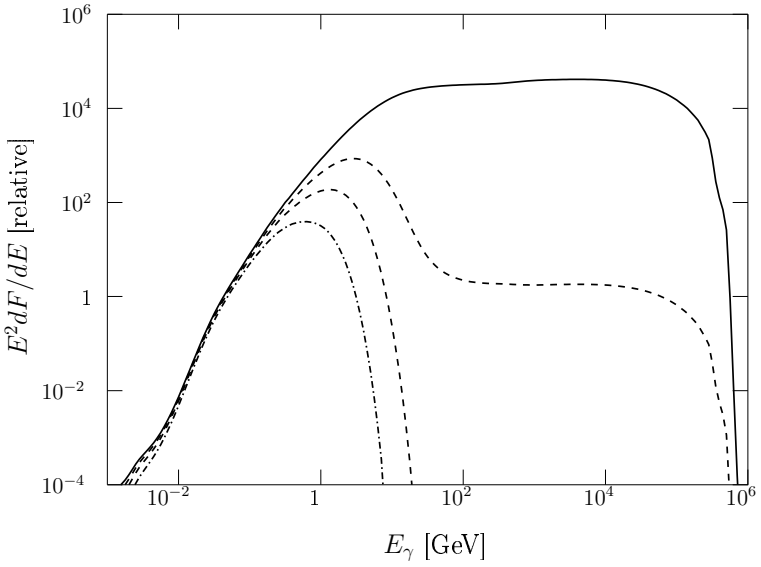


**Figure 6.13:** Gamma-ray spectra, calculated per solid angle, from a proton jet, with a Gaussian intensity profile (FWHM 3°) centered on the jet axis, observed from four different angles, $\theta = 0°$ (solid) 5° (dashed), 10° (dotted), and 20° (dot-dashed). The protons in the jet are assumed to follow a power-law distribution with index $\Gamma = 2.0$ and extending up to $T_p = 512$ TeV.

# Chapter 7

# Conclusions and Outlook

Cosmic gamma rays are of great importance for the understanding of processes occuring in the Universe and their properties make them excellent probes. By studying gamma rays of cosmic origin, one can learn about acceleration of particles in supernova remnants and AGN jets. They may also provide insights to the dark matter in the Universe. Gamma-ray telescopes, both ground-based, such as H.E.S.S. and VERITAS, and spaceborne, such as the upcoming GLAST satellite, provide the tools to observe cosmic gamma rays. The excellent angular resolution, field of view and sensitivity of the GLAST Large Area Telescope will provide greatly improved data in the GeV energy band.

Gamma rays can be produced by a number of different mechanisms. In the highest-energy regime, the dominant mechanism is the decay of neutral pions produced in interactions between cosmic-ray nuclei and interstellar matter; mostly proton-proton interactions. Another important mechanism is up-scattering of low-energy photons from the cosmic microwave background or even infrared starlight on ultra-relativistic electrons. The spectral shape is quite different for these two mechanisms. By accurately measuring gamma-ray source spectra it should be possible to distinguish between the two and give conclusive evidence for the acceleration of cosmic-ray nuclei in sources such as supernova remnants.

It was noted by Kamae et al. (2005) that the current models (Stecker, 1970, 1973; Strong et al., 1978; Stephens & Badhwar, 1981; Dermer, 1986a,b; Stecker, 1989; Mori, 1997; Strong et al., 2000, 2004) lacked several key features of the inelastic proton-proton interaction. All these models relied on the assumption of Feynman scaling, which is known to be violated, left out the diffractive interaction and used an outdated inelastic proton-proton cross section. A model for the inelastic proton-proton interaction that incorporated all these features was proposed by Kamae et al. (2005) and extended with two baryon resonance-excitation states by Kamae et al. (2006). Monte Carlo simulations based on this model showed that the gamma-ray spectrum becomes harder in power-law index and that the violation of Feynman scaling increases the gamma-ray yield by about 30-80% (Kamae et al., 2005).

This change in the gamma-ray spectrum and yield indicated the usefulness of the updated modeling of the inelastic proton-proton interaction and the model has been parameterized for all the stable secondary particles - gamma rays, electrons, positrons, $\nu_e$, $\bar{\nu}_e$, $\nu_\mu$ and $\bar{\nu}_\mu$ - to facilitate fast and accurate calculations of inclusive cross sections in astrophysical applications.

Calculations of the total inclusive $\pi^0$ cross section from Monte Carlo simulations showed that the addition of the two baryon resonances $\Delta(1232)$ and res(1600) was necessary to reproduce the experimental data near the pion production threshold.

The parametric model of inclusive cross sections presented here reproduces the Monte Carlo simulated gamma-ray spectra from proton power-law spectra of index 2.0 and 2.7 within 10%, except near the higher kinematical limit were the error can be as much as 20%. It predicts the spectra of all stable secondary particles to be harder than that of the incident proton spectrum. It also predicts larger inclusive cross sections than would have been expected from previous models.

Lorentz invariant cross sections, $Ed^3\sigma/dp^3$, calculated from Monte Carlo simulations reproduce well experimental data below $p_t = 1$ GeV/c. The parameterized transverse momentum distributions for gamma rays can be fitted well by an exponential function and integration over $p_t$ recovers the inclusive cross section. Calculations of gamma-ray spectra for pencil beams of protons show that the peak of the spectrum is shifted to lower energies and the flux is drastically reduced as the observer is moved off the beam axis.

The parametric model for the inclusive gamma-ray, electron and positron cross sections have been incorporated into the Galprop code and used to calculate the $\pi^0$ component of the Galactic diffuse emission. The calculations show that the presented parametric model does not result in the drastic changes claimed by Kamae et al. (2005) and Kamae et al. (2006). The present model is still very valuable and it gives a flatter spectrum near the peak. The model has also been used to estimate the cosmic-ray flux in the Large Magellanic Cloud, a near-by galaxy. The estimate was derived from gamma-ray observations with EGRET and matter densities from HI and CO surveys. It is concluded that the cosmic-ray spectrum in the LMC is quite different from the local interstellar spectrum and that further observations with the GLAST-LAT will provide more details on the distribution and flux of cosmic rays in local galaxies.

Due to paucity of experimental data and widely accepted modeling, the present work does not include the contributions from interactions of heavier nuclei, such as $\alpha$-proton, proton-He or $\alpha$-He. In the Earth's vicinity, $\alpha$-particles contribute about 9% of the cosmic-ray flux (Schlickeiser, 2002) and the interstellar medium contains about 10% helium. For energies above the resonance region (proton kinetic energies above 3 GeV), the $\alpha$-particle and helium nucleus can, to a good approximation, be regarded as four independent nucleons. The error due to the non-inclusion of these particles is expected to be about 10% or less for light secondary particles in the high-energy regime (Kamae et al., 2005).

Inclusion of the $\alpha$-particle as projectile and helium as target may change the predicted electron-positron ratio significantly. Fermi motion and interactions in

the nucleus affect the pion production near the threshold (Crawford et al., 1980; Mårtensson et al., 2000) and in the resonance region. The pion multiplicity below 100 MeV is enhanced by this effect. The need for separate treatment of p-He, $\alpha$-p, and $\alpha$-He interactions in the future is acknowledged.

Parameterization of transverse momentum distributions of other stable secondary particles, i.e. electrons, positrons and neutrinos, has been deferred due to observational limitations. When high-statistics neutrino data becomes available (Halzen, 2005) it may be worthwhile to extend the parameterization to include neutrinos.

# Author's Contributions

The proton-proton interaction model described in Chapter 4 was first proposed by Professor Tune Kamae (see Kamae et al., 2005). I became involved in this work when I started as a graduate student and I took on the detailed analysis of parameters describing proton-proton interactions and their energy dependence. This study involved parameterizing the inclusive cross sections of all the stable secondary particles produces in such interactions, as described in Chapter 5

I did the main part of the work on parameterizing the transverse momentum distributions of gamma rays after Tune Kamae had proposed this to me and I have written most of the publication describing this work. While doing this, Per Carlson suggested studying the energy dependence for the average $p_t$. For this, I made further comparisons with Pythia following advise given by Per Carlson and Torbjörn Sjöstrand. The applications described in Chapter 6 were initiated and completed by myself with guidance from Tune Kamae, Igor Moskalenko, Hiro Tajima and Seth Digel.

Parts of this thesis have been published as:

1. Kamae, T. et al. 2004, in Proceedings of the 22nd Texas Symposium, Stanford, California
2. Kamae, T. et al. 2006, ApJ, 647, 692 (erratum 662, 779)
3. Karlsson, N. & Kamae, T. 2007, ApJ, in press, preprint (astro-ph/0709.0233)
4. Karlsson, N. et al. 2007, in AIP Conference Proceedings, Vol. 921, The 1st GLAST Symposium, ed. S. Ritz, P. Michelson & C. Meegan (Stanford, California: AIP), 486-487

The work on the Large Magellanic Cloud will be published later.

I have also presented the parameterizations and related results as poster contributions to the following conferences:

1. 22nd Texas Symposium, Stanford 2004
2. 9th AAS High Energy Astrophysics Division meeting, San Francisco 2006
3. The 1st GLAST Symposium, Stanford 2007

# Acknowledgments

First and foremost, I would like to thank Professor Per Carlson at the Royal Institute of Technology and Professor Tuneyoshi Kamae at the Stanford Linear Accelerator Center for giving me the opportunity to do research as a graduate student. Professor Kamae became my mentor during my stay at the Stanford Linear Accelerator Center. He introduced me to the fields of gamma-ray astronomy and cosmic-ray physics and he also co-authored the papers on which the thesis is based.

I am grateful to the hospitality extended by SLAC and KIPAC and the encouragement given by Professor Roger Blandford, Professor Steve Kahn and Professor Persis Drell. I would like to thank Dr. Tsunefumi Mizuno, now at the University of Hiroshima, for many valuable discussions and kindly answering all my questions about cosmic rays, gamma rays and astrophysics in general. He also co-authored the first paper. I thank Dr. Tatsumi Koi for providing the pion decay program implemented with Geant4 and Dr. Toshinori Abe for providing fortran code for running Pythia. Dr. Igor Moskalenko kindly made all-sky maps generated with Galprop available to me, the NANTEN team provided LMC CO data and Professor Lister Staveley-Smith (University of Western Australia) provided LMC HI data. I thank Professor Torbjörn Sjöstrand (Lund University) for help with Pythia related questions. Dr. Greg Madejski and Martin Müller deserves thanks for many valuable discussions, and Dr. Johann Cohen-Tanugi for help related to hadron physics and hadronic interactions. I also thank Dr. Seth Digel for his help related to EGRET and diffuse emission.

Finally I wish to express my appreciation for the encouragement, love and support given by my parents and my sister and brother in law during my time as a graduate student.

This work was partially supported by generous scholarships from Kooperativa Förbundet, given as a doctoral research scholarship via the Sweden-America Foundation, and Längmanska Kulturfonden, the KTH Physics Department and the Swedish GLAST consortium, and by the Department of Energy contract DE-AC02-76SF00515 to the Stanford Linear Accelerator Center.

# Bibliography

**Journal Abbreviations used in the Bibliography:**
A&A: Astronomy and Astrophysics
A&AS: Astronomy and Astrophysics Supplement Series
ApJ: Astrophysical Journal
ApJS: Astrophysical Journal Supplement Series
ApJL: Astrophysical Journal Letters
Ap&SS: Astrophysics and Space Science
MNRAS: Monthly Notices of the Royal Astronomical Society
PASJ: Publ. Astronomical Society Japan
JETP: Journal of Experimental and Theoretical Physics


Abbasi, R. U. et al. 2005, ApJ, 622, 910

Abe, F. et al. 1988, Phys. Rev. Lett., 61, 1819

Abe, K. et al. 2003, Phys. Lett. B, 564, 8

Affolder, T. et al. 2001, Phys. Rev. Lett., 87, 141802

Aharonian, F. A. 2004, Very High Energy Cosmic Gamma Radiation: A Crucial Window on the Extreme Universe (World Scientific Publishing)

Aharonian, F. A. et al. 2003, A&A, 403, L1

—. 2004a, Nature, 432, 75

—. 2004b, A&A, 425, L13

—. 2005, Science, 307, 1938

Alberi, J. & Goggi, G. 1981, Phys. Rep., 74, 1

Alcaraz, J. et al. 2000a, Phys. Lett. B, 490, 27

—. 2000b, Phys. Lett. B, 484, 10

Alner, G. J. et al. 1984, Phys. Lett. B., 138, 304

—. 1986, Z. Phys. C - Particles and Fields, 33, 1

—. 1987, Physics Reports, 154, 247

Alper, B. et al. 1975, Nucl. Phys., B100, 237

Alpgard, K. et al. 1983, Phys. Lett., 121, 209

Altarelli, G. & Parisi, G. 1977, Nucl. Phys. B, 126, 298

Amaldi, U. et al. 1978, Nucl. Phys. B, 145, 367

Andersson, B. 1998, The Lund Model (Cambridge University Press)

Andersson, B., Gustafson, G., & Peterson, C. 1979, Z. Phys., C1, 105

Andersson, B., Gustafson, G., & Sjöstrand, T. 1980, Z. Phys., C6, 235

Aversa, F. et al. 1997, Astroparticle Physics, 7, 219

Badhwar, G. D., Stephens, S. A., & Golden, R. L. 1977, Phys. Rev. D, 15, 820

Baksay, L. et al. 1988, Phys. Rev. D, 37, 587

Balke, B. et al. 1978, Nucl. Phys. B, 141, 1

Baltz, E. A., Taylor, J. E., & Wai, L. L. 2007, ApJ, 659, L125

Banner, M. et al. 1982, Phys. Lett., 115B, 59

—. 1983, Phys. Lett., 122B, 322

Baughman, B. M. et al. 2007, in Proceedings of the 30th International Cosmic Ray Conference, Merida, Mexico

Beilicke, M. et al. 2005, in Proceedings of the 29th International Cosmic Ray Conference, ed. B. S. Acharya et al., Pune, India

Bell, A. R. 1978, MNRAS, 182, 147

Bellotti, R. 1999, Phys. Rev. D, 60, 052002

Beltrami, I. et al. 1987, Phys. Lett. B, 194, 326

Berezhko, E. G. & Volk, H. J. 2000, ApJ, 540, 923

Bergström, L. et al. 2007, in AIP Conference Proceedings, Vol. 921, The 1st GLAST Symposium, ed. S. Ritz, P. Michelson, & C. Meegan (Stanford, California: AIP), 504–505

Bigongiari, C. 2006, preprint (astro-ph/0611847)

Blandford, R. D. & Eichler, D. 1987, Physics Reports, 154, 1

Blattnig, S. R. et al. 2000, Phys. Rev. D, 62, 094030

Blom, J. J. et al. 1999, ApJ, 516, 44

Boetzio, M. et al. 1999, ApJ, 518, 457

—. 2000, ApJ, 532, 653

—. 2004, preprint (astro-ph/0212253)

Böttcher, M. & Reimer, A. 2004, ApJ, 609, 576

Breakstone, A. et al. 1984, Phys. Rev. D, 30, 528

Bugg, D. V. et al. 1964, Phys. Rev., 133

Burkard, H. et al. 1985, Phys. Lett. B, 160, 343

Carlson, P. 1986, in Proceedings of the 10th European Cosmic Ray Symposium, ed. M. F. Bourdeau, J. N. Capdevielle, & P. Gabinski, Bordeaux University, France

Carlson, P. 2005, in Proceedings of the 17th ESA Symposium on European Rocket and Balloon Programmes and Related Research, ed. B. Warmbein, Sandefjord, Norway, ESA SP-590

Chamberlain, O. et al. 1955, Phys. Rev. Lett., 100, 947

Chiang, J. & Mukherjee, R. 1998, ApJ, 496, 752

Chiba, N. et al. 1992, Nucl. Instr. Methods A, 311, 338

Cillis, A. N. & Hartman, R. C. 2005, ApJ, 621, 291

Commins, E. D. & Bucksbaum, P. H. 1983, Weak interactions of leptons and quarks (Cambridge University Press)

Cool, R. L. et al. 1982, Phys. Rev. Lett., 48, 1451

Crawford, J. F. et al. 1980, Phys. Rev., C22, 1184

Derenzo, S. E. 1969, Phys. Rev., 181, 1854

Dermer, C. D. 1986a, A&A, 157, 223

—. 1986b, ApJ, 307, 47

—. 2006, ApJ, in press, preprint astro-ph/0605402

Dissertori, G., Knowles, I., & Schmelling, M. 2003, Quantum chromodynamics: High energy experiments and theory (Clarendon Press)

DuVernois, M. A. et al. 2001, ApJ, 559, 296

Edmonds, E. et al. 2007, in AIP Conference Proceedings, Vol. 921, The 1st GLAST Symposium, ed. S. Ritz, P. Michelson, & C. Meegan (Stanford, California: AIP), 514–515

Eggert, K. et al. 1975, Nucl. Phys. B, 98, 73

Enomoto, R. et al. 2002, Nature, 416, 823

Esposito, J. A. et al. 1999, ApJS, 123, 203

Fermi, E. 1949, Phys. Rev., 75, 1169

Feynman, R. P. 1969, High Energy Collisions, ed. C. N. Yang (Gordon & Breach), 237

—. 1972, Photon-Hadron Interactions (Reading, W. A. Benjamin)

Fickinger, W. J. et al. 1962, Phys. Rev., 125

Field, R. D. 2002, ME/MC Tuning Workshop, `http://www.phys.ufl.edu/~rfield/cdf/rdf_talks.html`

Funk, S. 2005, PhD thesis, Ruprecht-Karls-Universität Heidelberg, `http://www.ub.uni-heidelberg.de/archiv/5542`

Geich-Gimbel, C. 1987, Particle production at collider energies, Tech. Rep. Bonn-HE-87-30, Bonn University

Ginzburg, V. L. 1967, The Astrophysics of Cosmic Rays (Dokl. Acad. Nauk. SSR; English transl: NASA-TT-F561)

Givernaud, A. et al. 1979, Nucl. Phys. B, 152, 189

Good, M. L. & Walker, W. D. 1960, Phys. Rev., 120, 1855

Goulianos, K. 1983, Phys. Rep., 101, 169

—. 1995, Phys. Lett. B., 358, 379

Goulianos, K. & Montanha, J. 1999, Phys. Rev. D, 59, 114017

Greiner, W., Schramm, S., & Stein, E. 2002, Quantum Chromodynamics (Springer)

Greisen, K. 1966, Phys. Rev. Lett., 16, 748

Grimani, C. et al. 1989, Nucl. Instr. and Methods in Physics Res. A, 276, 367

—. 2002, A&A, 392, 287

Guzhavin, V. M. et al. 1964, Sov. Phys. JETP, 19, 847

Hagiwara, K. et al. 2002, Phys. Rev., D66, 010001

Halzen, F. 2005, in AIP Conference Proceedings, Vol. 745, 2nd International Symposium on High Energy Gamma-Ray Astronomy, ed. F. A. Aharonian, H. J. Völk, & D. Horns (New York: AIP), 3–13

Hartman, R. C. et al. 1999, ApJS, 123, 79

Hayakawa, S. 1969, Cosmic Ray Physics (John Wiley & Sons)

Hunter, S. D. et al. 1997, ApJ, 481, 205

Hurley, K. et al. 1994, Nature, 372, 652

Iyudin, A. F. et al. 2005, A&A, 429, 225

Jodidio, A. et al. 1986, Phys. Rev. D, 34, 1967

Kamae, T., Abe, T., & Koi, T. 2005, ApJ, 620, 244

Kamae, T. et al. 2006, ApJ, 647, 692, (erratum 662, 779)

Karlsson, N. & Kamae, T. 2007, ApJ, in press, preprint (astro-ph/0709.0233)

Katagiri, H. et al. 2005, ApJ, 619, L163

Kim, S. et al. 1998, ApJ, 503, 674

—. 2003, ApJS, 148, 473

Kobayashi, T. et al. 1999, in Proceedings of the 26th International Cosmic Ray Conference, Salt Lake City

Konopelko, A. et al. 2003, ApJ, 597, 851

Koyama, K. et al. 1997, PASJ, 49, L7

Kraushaar, W. L. & Clark, G. W. 1962, Phys. Rev. Lett., 8, 106

Lemoine, M. & Sigl, G. 2001, Physics and Astrophysics of Ultra-High-Energy Cosmic Rays (Springer)

Longair, M. S. 1994, High Energy Astrophysics, vol. 2, 2nd edn. (Cambridge University Press)

Macomb, D. J. & Gehrels, N. 1999, ApJS, 120, 335

Macri, L. M. et al. 2006, ApJ, 652, 1133

Menn, W. et al. 2000, ApJ, 533, 281

Mitchell, J. W. et al. 2005, Adv. Space res., 35, 135

Mizuno, N. et al. 2001, PASJ, 53, 971

Mori, M. 1997, ApJ, 478, 225

Moskalenko, I. V. et al. 2002, ApJ, 565, 280

Mårtensson, J. et al. 2000, Phys. Rev., C62, 014610

Mücke, A. & Pohl, M. 2000, MNRAS, 312, 177

Mücke, A. & Protheroe, R. J. 2001, Astroparticle Physics, 15, 121

Mücke, A. et al. 2003, Astroparticle Physics, 18, 593

Murthy, P. V. R. & Wolfendale, A. W. 1986, Gamma-Ray Astronomy (Cambridge University Press)

Ong, R. A. 1998, Physics Reports, 305, 93

Ong, R. A. 2005, in Proceedings of the 29th International Cosmic Ray Conference, ed. B. S. Acharya et al., Pune, India

Perl, M. 1974, High Energy Hadron Physics (John Wiley & Sons)

Pickup, E., Robinson, D. K., & Salant, E. O. 1962, Phys. Rev., 125, 2091

Picozza, P. et al. 2007, preprint (astro-ph/0608697

Punch, M. et al. 1992, Nature, 358, 477

Quinn, J. et al. 1996, ApJ, 456, L83

Reimer, A., Protheroe, R. J., & Donea, A.-C. 2004, A&A, 419, 89

Rossi, A. M. et al. 1975, Nuclear Physics, B84, 269

Rossi, B. 1930, Phys. Rev., 36, 606

Rybicki, G. B. & Lightman, A. P. 2004, Radiative Processes in Astrophysics (John Wiley & Sons)

Sanuki, T. et al. 2000, ApJ, 545, 1135

Schein, M. et al. 1941, Phys. Rev., 59, 615

Schlickeiser, R. 2002, Cosmic Ray Astrophysics (Springer)

Schönfelder, V. 2001, The Universe in Gamma Rays (Springer)

Schroedter, M. et al. 2005, ApJ, 634, 947

Seo, E. S. et al. 1991, ApJ, 378, 763

Sjöstrand, T., Lönnblad, L., & Mrenna, S. 2001a, Pythia 6.2: Physics and Manual, hep-ph/0108264

Sjöstrand, T. & Skands, P. Z. 2004, preprint (hep-ph/0402078)

Sjöstrand, T. et al. 2001b, Comput. Phys. Commun., 135, 238

Slane, P. et al. 1999, ApJ, 525, 357

Sreekumar, P. et al. 1992, ApJ, 400, L67

—. 1993, Phys. Rev. L, 70, 127

—. 1994, ApJ, 426, 105

Stecker, F. W. 1970, Ap&SS, 377

—. 1973, ApJ, 185, 499

—. 1989, Cosmic Gamma Rays, Neutrinos and Related Astrophysics, ed. M. M. Shapiro & J. P. Wefel (Kluwer Academic Publishers), 85–120

Stecker, F. W., Hunter, S. D., & Kniffen, D. A. 2007, preprint (astro-ph/07054311)

Stecker, F. W. & Salamon, M. H. 1996, ApJ, 464, 600

Stephens, S. A. & Badhwar, G. G. 1981, Ap&SS, 76, 213

Strong, A. W. & Moskalenko, I. V. 1998, ApJ, 509, 212

Strong, A. W., Moskalenko, I. V., & Ptuskin, V. S. 2007, Annu. Rev. Nucl. Part. Sci., 57, 285

Strong, A. W., Moskalenko, I. V., & Reimer, O. 2000, ApJ, 537, 763, (erratum 541, 1109)

—. 2004, ApJ, 613, 962

Strong, A. W. et al. 1978, MNRAS, 182, 751

—. 1982, A&A, 115, 404

Swanenburg, B. N. et al. 1981, ApJ, 243, L69

Tsunemi, H. et al. 2000, PASJ, 52, 887

Uchiyama, Y., Aharonian, F. A., & Takahashi, T. 2003, A&A, 400, 567

Uchiyama, Y. et al. 2007, Nature, 449, 576

Vladimirov, A., Ellison, D. C., & Bykov, A. 2006, ApJ, 652, 1246

Watson, A. 2007, in Proceedings of the 30th International Cosmic Ray Conference, Merida, Mexico

Weekes, T. C. 2003a, in Proceedings of the 28th International Cosmic Ray Conference, Tsukuba, Japan

Weekes, T. C. 2003b, Very High Energy Gamma-Ray Astronomy (IOP Publishing)

Weekes, T. C. et al. 1989, ApJ, 342, 379

Yamamoto, A. et al. 2003, in Proceedings of the 28th International Cosmic Ray Conference, Tsukuba, Japan

Yoshida, S. et al. 1995, Astroparticle Physics, 3, 105

Yoshida, T. et al. 2004, Adv. Space res., 33, 1755

Zatsepin, G. T. & Kuzmin, V. A. 1966, Pisma Zh. Eksp. Teor. Fiz., 4, 114, (also 1966, JETP Lett. 4, 78)

# List of Figures

# List of Tables

# Appendix A

# Pion Decay Kinematics

The pion decays are

$$\begin{aligned} \pi^0 &\rightarrow \gamma\gamma \quad (98.80\%) \\ \pi^+ &\rightarrow \mu^+ + \nu_\mu \quad (99.99\%) \\ \pi^- &\rightarrow \mu^- + \bar{\nu}_\mu \quad (99.99\%) \end{aligned} \tag{A.1}$$

These are all two-body decays and the kinematics can easily be worked out. The value in the parenthesis is the branching ratio for that particular mode. These are the dominant decay modes and all other modes can safely be neglected. In the following the kinetic energies of the decay products in each of the decays will be derived.

The $\pi^0$ decays into two gamma rays. In the pion rest frame, conservation of linear momentum requires the photons be emitted in opposite directions and conservation of energy gives $E^*_\gamma = m_{\pi^0}/2$. Because the neutral pion has spin zero, the angular distribution will be isotropic in spherical coordinates ($\theta^*$, $\phi^*$) in the pion rest frame. Performing a Lorentz transformation from the rest frame to the laboratory frame gives a flat energy spectrum with gamma-ray energy $E_\gamma$ in the range

$$\frac{E_\pi}{2}(1+\beta) \leq E_\gamma \leq \frac{E_\pi}{2}(1-\beta) \tag{A.2}$$

where $E_\pi$ is the energy of the pion in the laboratory frame and $\beta = v/c$ for the pion.

As shown in A.1, charged pions decay into a muon and a muon neutrino. Assuming a negligible neutrino mass, in the pion rest frame conservation of linear momentum gives

$$p_\nu^2 = p_\mu^2 = T_\mu^2 + 2T_\mu m_\mu \tag{A.3}$$

and conservation of energy gives

$$m_\pi = E_\mu + p_\nu \tag{A.4}$$

and then it follows that

$$T_\mu = E_\mu - m_\mu = (m_\pi - p_\nu) - m_\mu \tag{A.5}$$

Using equation A.5 in equation A.3 gives

$$p_\nu^2 = (m_\pi - m_\mu)^2 + p_\nu^2 - 2p_\nu(m_\pi - m_\mu) + 2(m_\pi - m_\mu - p_\nu)m_\mu \tag{A.6}$$

and it follows that

$$2p_\nu(m_\pi - m_\mu) + 2p_\nu m_\mu = (m_\pi - m_\mu)^2 + 2(m_\pi - m_\mu)m_\mu \tag{A.7}$$

and

$$p_\nu = \frac{(m_\pi - m_\mu)^2 + 2(m_\pi - m_\mu)m_\mu}{2m_\pi} = \frac{m_\pi^2 - m_\mu^2}{2m_\pi} \tag{A.8}$$

The charged pions also have spin zero and the angular distribution of the muon and neutrino will be isotropic in spherical coordinates ($\theta^*$, $\phi^*$), in the pion rest frame. Performing a Lorentz transformation, gives the muon energy and momentum in the laboratory frame.

The muon is itself unstable and will decay into an electron or a positron and more neutrinos

$$\begin{aligned} \mu^+ &\rightarrow e^+ + \nu_e + \bar{\nu}_\mu \\ \mu^- &\rightarrow e^- + \bar{\nu}_e + \nu_\mu \end{aligned} \tag{A.9}$$

These are three-body decays, and the decay products do not have fixed energies but will follow some spectrum. Since this is a weak interaction decay, this spectrum is the Michel spectrum from V-A theory.

According to the Michel spectrum (Commins & Bucksbaum, 1983)

$$\frac{d^2\Gamma}{dx\,d\cos(\theta)} \propto F_{\rm IS}(x) + P_\mu \cos(\theta) F_{\rm AS}(x) \tag{A.10}$$

where $x = E_e/E_e^{\rm max}$, $P_\mu$ is the muon polarization, and

$$F_{\rm IS}(x) = x^2(1-x) + \frac{2}{9}\rho(4x^3 - 3x^2) + \eta\frac{m_e}{E_e^{\rm max}}x(1-x) \tag{A.11}$$

$$F_{\rm AS}(x) = \frac{1}{3}\xi x^2\left[1 - x + \frac{2}{3}\delta(4x-3)\right] \tag{A.12}$$

where $\rho$, $\eta$, $\delta$ and $\xi$ are the Michel parameters and their predicted values as well as experimentally measured values are listed in Table A.1.

Integrating equation A.10 over $d\cos(\theta)$ we get

$$\frac{d\Gamma}{dx} = \int \frac{d^2\Gamma}{dx\,d\cos(\theta)} d\cos(\theta) = 2F_{IS}(x) \tag{A.13}$$

The energy and direction of the electron in the muon rest frame can now be calculated by the following algorithm:

**Table A.1:** Parameters for the Michel spectrum

| Parameter | V-A prediction | Experimental | Reference |
|---|---|---|---|
| $\rho$ | 0.75 | 0.7518±0.0026 | Derenzo (1969) |
| $\eta$ | 0.0 | -0.007±0.0013 | Burkard et al. (1985) |
| $\delta$ | 0.75 | 0.7486±0.0026±0.0028 | Balke et al. (1978) |
| $P_\mu\xi$ | $\xi$=1.0 | 1.0027±0.0079±0.0030 | Beltrami et al. (1987) |
| $P_\mu\frac{\xi\delta}{\rho}$ | $\xi\delta/\rho$=1.0 | 0.99682, CL=90% | Jodidio et al. (1986) |

1. Draw a random number $x$ according to $d\Gamma/dx$. This gives the electron energy through $x = E_e/E_e^{\max}$. If the neutrino masses are neglected, the maximum electron energy, $E_e^{\max}$, can be taken as

$$E_e^{\max} \simeq \frac{m_\mu}{2} \tag{A.14}$$

2. Assume $\theta = 0$ is in the muon direction.

3. Pick $\theta$ according to $d^2\Gamma/(dx d\cos(\theta))$ with $x$ from above.

4. Randomly pick $\phi$ on $[0, 2\pi]$.

Again, performing a Lorentz transformation gives the electron energy in the laboratory frame. If one wants to know the angular distribution, it is neccessary to rotate the coordinate system to line up with that of the pion.

# Appendix B

# Pythia Parameter Settings

In the high energy range, i.e. proton kinetic energies 52.6 GeV and above, events for the non-diffractive process were generated with Pythia version 6.2. The same parameter set as used by Kamae et al. (2005) for "model A", i.e. that of CDF collaboration "tune A" (Field, 2002; Sjöstrand & Skands, 2004), was used for the model in this thesis.

The default setup for proton-proton interaction was selected by setting MSEL=1 in COMMON/PYSUBS. Other parameters used are listed below. For Pythia 6.4 parameters does not have to be set manually. A call of PYTUNE(100) sets up "tune A" and PYTUNE(104) sets up "tune DWT".

(a) Multiple interaction, CDF "tune A":

| | | | | | |
|---|---|---|---|---|---|
| MSTP(81) | = | 1 | MSTP(82) | = | 4 |
| PARP(82) | = | 2.0 | PARP(83) | = | 0.5 |
| PARP(84) | = | 0.4 | PARP(85) | = | 0.9 |
| PARP(86) | = | 0.95 | PARP(67) | = | 4.0 |
| PARP(89) | = | 1800.0 | PARP(90) | = | 0.25 |

(c) Force instant decay of charged pions, kaons, K-longs and muons:

| | | |
|---|---|---|
| KCPI | = | PYCOMP(211) |
| MDCY(KCPI, 1) | = | 1 |
| KCK | = | PYCOMP(321) |
| MDCY(KCK, 1) | = | 1 |
| KCKL | = | PYCOMP(130) |
| MDCY(KCKL, 1 | = | 1 |
| KCMU | = | PYCOMP(13) |
| MDCY(KCMU, 1) | = | 1 |

# Appendix C

# Parametric Model Parameters

## C.1 Kinematic Cutoff Parameters

**Table C.1:** Parameters for the non-diffractive cutoff function

| Particle | $L_{\min}$ | $L_{\max}$[a] | $W_{\mathrm{nd,l}}$ | $W_{\mathrm{nd,h}}$ |
|---|---|---|---|---|
| $\gamma$ | -2.6 | $0.96\log(T_p)$ | 15 | 44 |
| $e^-$ | -2.6 | $0.96\log(T_p)$ | 20 | 45 |
| $e^+$ | -2.6 | $0.94\log(T_p)$ | 15 | 47 |
| $\nu_e$ | -2.6 | $0.98\log(T_p)$ | 15 | 42 |
| $\bar{\nu}_e$ | -2.6 | $0.98\log(T_p)$ | 15 | 40 |
| $\nu_\mu$ | -2.6 | $0.94\log(T_p)$ | 20 | 45 |
| $\bar{\nu}_\mu$ | -2.6 | $0.98\log(T_p)$ | 15 | 40 |

[a] Proton kinetic energy $T_p$ is in GeV

## C.2 Parameters for Inclusive Cross Sections

The following tables summarize the parameters $a_0, \ldots, a_8$, $b_0, \ldots, b_7$, $c_0, \ldots, c_4$ and $d_0, \ldots, d_4$ in equations 5.7, 5.9, 5.10, 5.11 for gamma rays, electrons, positrons, $\nu_e$, $\bar{\nu}_e$, $\nu_\mu$ and $\bar{\nu}_\mu$. To ease the use of these, a library, `cparamlib`, in the c programming language is readily available at `http://www.slac.stanford.edu/~niklas/Public/`. An example program calculating gamma-ray spectra is also included.

**Table C.2:** Parameters describing gamma ray spectra for arbitrary proton energy

| Parameter | Formulae as functions of proton kinetic energy ($y = \log T_p$) in TeV. |
|---|---|
| | Non-diff., eq. 5.7 |
| $a_0$ ..... | $-0.51187(y+3.3) + 7.6179(y+3.3)^2 - 2.1332(y+3.3)^3 + 0.22184(y+3.3)^4$ |
| $a_1$ ..... | $-1.2592 \cdot 10^{-5} + 1.4439 \cdot 10^{-5} \exp(-0.29360(y+3.4)) + 5.9363 \cdot 10^{-5}/(y+4.1485) +$ $2.2640 \cdot 10^{-6} y - 3.3723 \cdot 10^{-7} y^2$ |
| $a_2$ ..... | $-174.83 + 152.78 \log(1.5682(y+3.4)) - 808.74/(y+4.6157)$ |
| $a_3$ ..... | $0.81177 + 0.56385y + 0.0040031y^2 - 0.0057658y^3 + 0.00012057y^4$ |
| $a_4$ ..... | $0.68631(y+3.32) + 10.145(y+3.32)^2 - 4.6176(y+3.32)^3 + 0.86824(y+3.32)^4 +$ $-0.053741(y+3.32)^5$ |
| $a_5$ ..... | $9.0466 \cdot 10^{-7} + 1.4539 \cdot 10^{-6} \log(0.015204(y+3.4)) + 1.3253 \cdot 10^{-4}/(y+4.7171)^2 +$ $-4.1228 \cdot 10^{-7} y + 2.2036 \cdot 10^{-7} y^2$ |
| $a_6$ ..... | $-339.45 + 618.73 \log(0.31595(y+3.9)) + 250.20/(y+4.4395)^2$ |
| $a_7$ ..... | $-35.105 + 36.167y - 9.3575y^2 + 0.33717y^3$ |
| $a_8$ ..... | $0.17554 + 0.37300y - 0.014938y^2 + 0.0032314y^3 + 0.0025579y^4$ |
| $r(y)$ ..... | $3.05 \exp(-107((y+3.25)/(1+8.08(y+3.25)))^2)$; $T_p \leq 1.95$ GeV<br>1.01; $T_p > 1.95$ GeV |
| | Diffraction, eq. 5.9[a] |
| $b_0$ ..... | $60.142 \tanh(-0.37555(y+2.2)) - 5.9564(y+0.59913)^2 + 6.0162 \cdot 10^{-3}(y+9.4773)^4$ |
| $b_1$ ..... | $35.322 + 3.8026 \tanh(-2.5979(y+1.9)) - 2.1870 \cdot 10^{-4}(y+369.13)^2$ |
| $b_2$ ..... | $-15.732 - 0.082064 \tanh(-1.9621(y+2.1)) + 2.3355 \cdot 10^{-4}(y+252.43)^2$ |
| $b_3$ ..... | $-0.086827 + 0.37646 \exp(-0.53053((y+1.0444)/(1.0+0.27437(y+1.0444)))^2)$ |
| $b_4$ ..... | $2.5982 + 0.39131(y+2.95)^2 - 0.0049693(y+2.95)^4 +$ $+0.94131 \exp(-24.347(y+2.45-0.19717(y+2.45)^2)^2)$ |
| $b_5$ ..... | $0.11198 - 0.64582y + 0.16114y^2 +$ $+2.2853 \exp(-0.0032432((y-0.83562)/(1.0+0.33933(y-0.83562)))^2)$ |
| $b_6$ ..... | $1.7843 + 0.91914y + 0.050118y^2 + 0.038096y^3 - 0.027334y^4 - 0.0035556y^5 +$ $+0.0025742y^6$ |
| $b_7$ ..... | $-0.19870 - 0.071003y + 0.019328y^2 - 0.28321 \exp(-6.0516(y+1.8441)^2)$ |
| | $\Delta(1232)$, eq. 5.10 |
| $c_0$ ..... | $2.4316 \exp(-69.484((y+3.1301)/(1.0+1.24921(y+3.1301)))^2) - 6.3003 +$ $-9.5349/y + 0.38121y^2$ |
| $c_1$ ..... | $56.872 + 40.627y + 7.7528y^2$ |
| $c_2$ ..... | $-5.4918 - 6.7872 \tanh(4.7128(y+2.1)) + 0.68048y$ |
| $c_3$ ..... | $-0.36414 + 0.039777y$ |
| $c_4$ ..... | $-0.72807 - 0.48828y - 0.092876y^2$ |
| | res(1600), eq. 5.11 |
| $d_0$ ..... | $3.2433 \exp(-57.133((y+2.9507)/(1.0+1.2912(y+2.9507)))^2) - 1.0640 - 0.43925y$ |
| $d_1$ ..... | $16.901 + 5.9539y - 2.1257y^2 - 0.92057y^3$ |
| $d_2$ ..... | $-6.6638 - 7.5010 \tanh(30.322(y+2.1)) + 0.54662y$ |
| $d_3$ ..... | $-1.50648 - 0.87211y - 0.17097y^2$ |
| $d_4$ ..... | $0.42795 + 0.55136y + 0.20707y^2 + 0.027552y^3$ |

[a] $b_0, \ldots, b_3 = 0$ for $T_p < 5.52$ GeV

**Table C.3:** Parameters describing electron spectra for arbitrary proton energy

| Parameter | Formulae as functions of proton kinetic energy ($y = \log T_p$) in TeV. |
|---|---|
| | Non-diff., eq. 5.7 |
| $a_0$ ..... | $-0.018639(y+3.3) + 2.4315(y+3.3)^2 - 0.57719(y+3.3)^3 + 0.063435(y+3.3)^4$ |
| $a_1$ ..... | $7.1827 \cdot 10^{-6} - 3.5067 \cdot 10^{-6} y + 1.3264 \cdot 10^{-6} y^2 - 3.3481 \cdot 10^{-7} y^3 + 2.3551 \cdot 10^{-8} y^4 +$ $+3.4297 \cdot 10^{-8} y^5$ |
| $a_2$ ..... | $563.91 - 362.18 \log(2.7187(y+3.4)) - 2.8924 \cdot 10^4/(y+7.9031)^2$ |
| $a_3$ ..... | $0.52684 + 0.57717y + 0.0045336y^2 - 0.0089066y^3$ |
| $a_4$ ..... | $0.36108(y+3.32) + 1.6963(y+3.32)^2 - 0.074456(y+3.32)^3 - 0.071455(y+3.32)^4 +$ $+0.010473(y+3.32)^5$ |
| $a_5$ ..... | $9.7387 \cdot 10^{-5} + 7.8573 \cdot 10^{-5} \log(0.0036055(y+4.3)) + 0.00024660/(y+4.9390) +$ $-3.8097 \cdot 10^{-7} y^2$ |
| $a_6$ ..... | $-273.00 - 106.22 \log(0.34100(y+3.4)) + 89.037y - 12.546y^2$ |
| $a_7$ ..... | $432.53 - 883.99 \log(0.19737(y+3.9)) - 4.1938 \cdot 10^4/(y+8.5518)^2$ |
| $a_8$ ..... | $-0.12756 + 0.43478y - 0.0027797y^2 - 0.0083074y^3$ |
| $r(y)$ ..... | $3.63 \exp(-106((y+3.26)/(1+9.21(y+3.26)))^2) - 0.182y - 0.175y^2$; $T_p \leq 15.6$ GeV<br>1.01; $T_p > 15.6$ GeV |
| | Diffraction, eq. 5.9[a] |
| $b_0$ ..... | $0.20463 \tanh(-6.2370(y+2.2)) - 0.16362(y+1.6878)^2 + 3.5183 \cdot 10^{-4}(y+9.6400)^4$ |
| $b_1$ ..... | $1.6537 + 3.8530 \exp(-3.2027((y+2.0154)/(1.0+0.62779(y+2.0154)))^2)$ |
| $b_2$ ..... | $-10.722 - 0.082672 \tanh(-1.8879(y+2.1)) + 1.4895 \cdot 10^{-4}(y+256.63)^2$ |
| $b_3$ ..... | $-0.023752 - 0.51734 \exp(-3.3087((y+1.9877)/(1.0+0.40300(y+1.9877)))^2)$ |
| $b_4$ ..... | $0.94921 + 0.12280(y+2.9)^2 - 7.1585 \cdot 10^{-4}(y+2.9)^4 + 0.52130 \log(y+2.9)$ |
| $b_5$ ..... | $-4.2295 - 1.0025 \tanh(9.0733(y+1.9)) - 0.11452 * (y - 62.382)$ |
| $b_6$ ..... | $1.4862 + 0.99544y - 0.042763y^2 - 0.0040065y^3 + 0.0057987y^4$ |
| $b_7$ ..... | $6.2629 + 6.9517 \tanh(-0.36480(y+2.1)) - 0.026033 * (y - 2.8542)$ |
| | res(1600), eq. 5.11 |
| $d_0$ ..... | $0.37790 \exp(-56.826((y+2.9537)/(1.0+1.5221(y+2.9537)))^2) - 0.059458 +$ $+0.0096583y^2$ |
| $d_1$ ..... | $-5.5135 - 3.3988y$ |
| $d_2$ ..... | $-7.1209 - 7.1850 \tanh(30.801(y+2.1)) + 0.35108y$ |
| $d_3$ ..... | $-6.7841 - 4.8385y - 0.91523y^2$ |
| $d_4$ ..... | $-134.03 - 139.63y - 48.316y^2 - 5.5526y^3$ |

[a] $b_0, \ldots, b_3 = 0$ for $T_p < 5.52$ GeV

**Table C.4:** Parameters describing positron spectra for arbitrary proton energy

| Parameter | Formulae as functions of proton kinetic energy ($y = \log T_p$) in TeV. |
|---|---|
| | Non-diff., eq. 5.7 |
| $a_0$ ..... | $-0.79606(y+3.3) + 7.7496(y+3.3)^2 - 3.9326(y+3.3)^3 + 0.80202(y+3.3)^4 +$ $-0.054994(y+3.3)^5$ |
| $a_1$ ..... | $6.7943 \cdot 10^{-6} - 3.5345 \cdot 10^{-6} y + 6.0927 \cdot 10^{-7} y^2 + 2.0219 \cdot 10^{-7} y^3 + 5.1005 \cdot 10^{-8} y^4 +$ $-4.2622 \cdot 10^{-8} y^5$ |
| $a_2$ ..... | $44.827 - 81.378 \log(0.027733(y+3.5)) - 1.3886 \cdot 10^4/(y+8.4417)$ |
| $a_3$ ..... | $0.52010 + 0.59336y + 0.012032y^2 - 0.0064242y^3$ |
| $a_4$ ..... | $2.1361(y+3.32) + 1.8514(y+3.32)^2 - 0.47872(y+3.32)^3 + 0.0032043(y+3.32)^4 +$ $+0.0082955(y+3.32)^5$ |
| $a_5$ ..... | $1.0845 \cdot 10^{-6} + 1.4336 \cdot 10^{-6} \log(0.0077255(y+4.3)) + 1.3018 \cdot 10^{-4}/(y+4.8188)^2 +$ $+9.3601 \cdot 10^{-8} y$ |
| $a_6$ ..... | $-267.74 + 14.175 \log(0.35391(y+3.4)) + 64.669/(y-7.7036)^2$ |
| $a_7$ ..... | $138.26 - 539.84 \log(0.12467(y+3.9)) - 1.9869 \cdot 10^4/(y+7.6884)^2 + 1.0675y^2$ |
| $a_8$ ..... | $-0.14707 + 0.40135y + 0.0039899y^2 - 0.0016602y^3$ |
| $r(y)$ ..... | $2.22 \exp(-98.9((y+3.25)/(1+10.4(y+3.25)))^2)$; $T_p \leq 5.52$ GeV |
| | 1.0; $T_p > 5.52$ GeV |
| | Diffraction, eq. 5.9[a] |
| $b_0$ ..... | $29.192 \tanh(-0.37879(y+2.2)) - 3.2196(y+0.67500)^2 + 0.0036687(y+9.0824)^4$ |
| $b_1$ ..... | $-142.97 + 147.86 \exp(-0.37194((y+1.8781)/(1.0+3.8389(y+1.8781)))^2)$ |
| $b_2$ ..... | $-14.487 - 4.2223 \tanh(-13.546(y+2.2)) + 1.6988 \cdot 10^{-4}(y+234.65)^2$ |
| $b_3$ ..... | $-0.0036974 - 0.41976 \exp(-6.1527((y+1.8194)/(1.0+0.99946(y+1.8194)))^2)$ |
| $b_4$ ..... | $1.8108 + 0.18545(y+2.9)^2 - 0.0020049(y+2.9)^4 +$ $+0.85084 \exp(-14.987(x+2.29-0.18967(x+2.29)^2)^2)$ |
| $b_5$ ..... | $2.0404 - 0.51548 \tanh(2.2758(y+1.9)) - 0.035009/(y-6.6555)$ |
| $b_6$ ..... | $1.5258 + 1.0132y - 0.064388y^2 - 0.0040209y^3 - 0.0082772y^4$ |
| $b_7$ ..... | $3.0551 + 3.5240 \tanh(-0.36739(y+2.1)) - 0.13382 * (y-2.7718)$ |
| | $\Delta(1232)$, eq. 5.10 |
| $c_0$ ..... | $2.9841 \exp(-67.857((y+3.1272)/(1.0+0.22831(y+3.1272)))^2) - 6.5855 - 9.6984/y +$ $+0.41256y^2$ |
| $c_1$ ..... | $6.8276 + 5.2236y + 1.4630y^2$ |
| $c_2$ ..... | $-6.0291 - 6.4581 \tanh(5.0830(y+2.1)) + 0.46352y$ |
| $c_3$ ..... | $0.59300 + 0.36093y$ |
| $c_4$ ..... | $0.77368 + 0.44776y + 0.056409y^2$ |
| | res(1600), eq. 5.11 |
| $d_0$ ..... | $1.9186 \exp(-56.544((y+2.9485)/(1.0+1.2892(y+2.9485)))^2) - 0.23720 + 0.041315y^2$ |
| $d_1$ ..... | $-4.9866 - 3.1435y$ |
| $d_2$ ..... | $-7.0550 - 7.2165 \tanh(31.033(y+2.1)) + 0.38541y$ |
| $d_3$ ..... | $-2.8915 - 2.1495y - 0.45006y^2$ |
| $d_4$ ..... | $-1.2970 - 0.13947y - 0.41197y^2 - 0.10641y^3$ |

[a] $b_0, \ldots, b_3 = 0$ for $T_p < 11.05$ GeV

**Table C.5:** Parameters describing electron neutrino spectra for arbitrary proton energy

| Parameter | Formulae as functions of proton kinetic energy ($y = \log T_p$) in TeV. |
|---|---|
| | Non-diff., eq. 5.7 |
| $a_0$ ..... | $0.0074087 + 2.9161(y+3.31) + 0.99061(y+3.31)^2 - 0.28694(y+3.31)^3 + +0.038799(y+3.31)^4$ |
| $a_1$ ..... | $-3.2480 \cdot 10^{-5} + 7.1944 \cdot 10^{-5} \exp(-0.21814(y+3.4)) + 2.0467 \cdot 10^{-5}/(y+4.1640) + +5.6954 \cdot 10^{-6} y - 3.4105 \cdot 10^{-7} y^2$ |
| $a_2$ ..... | $-230.50 + 58.802y - 9.9393y^2 + 1.2473y^3 - 0.26322y^4$ |
| $a_3$ ..... | $0.45064 + 0.56930y + 0.012428y^2 - 0.0070889y^3$ |
| $a_4$ ..... | $-0.011883 + 1.7992(y+3.32) + 3.5264(y+3.32)^2 - 1.7478(y+3.32)^3 + +0.32077(y+3.32)^4 - 0.017667(y+3.32)^5$ |
| $a_5$ ..... | $-1.6238 \cdot 10^{-7} + 1.8116 \cdot 10^{-6} \exp(-0.30111(y+3.4)) + 9.6112 \cdot 10^{-5}/(y+4.8229)^2$ |
| $a_6$ ..... | $-261.30 - 43.351 \log(0.35298(y+3.4)) + 70.925/(y-8.7147)^2$ |
| $a_7$ ..... | $184.45 - 1473.6/(y+6.8788) - 4.0536y^2$ |
| $a_8$ ..... | $-0.24019 + 0.38504y + 0.0096869y^2 - 0.0015046y^3$ |
| $r(y)$ ..... | $0.329 \exp(-247((y+3.26)/(1+6.56(y+3.26)))^2) - 0.957y - 0.229y^2$; $T_p \leq 7.81$ GeV<br>1.0; $T_p > 7.81$ GeV |
| | Diffraction, eq. 5.9[a] |
| $b_0$ ..... | $53.809 \tanh(-0.41421(y+2.2)) - 6.7538(y+0.76010)^2 + 0.0088080(y+8.5075)^4$ |
| $b_1$ ..... | $-50.211 + 55.131 \exp(1.3651((y+1.8901)/(1.0+4.4440(y+1.8901)))^2)$ |
| $b_2$ ..... | $-17.231 + 0.041100 \tanh(7.9638(y+1.9)) - 0.055449y + 2.5866 \cdot 10^{-4}(y+250.68)^2$ |
| $b_3$ ..... | $12.335 - 12.893 \exp(-1.4412((y+1.8998)/(1.0+5.5969(y+1.8998)))^2)$ |
| $b_4$ ..... | $1.3558 + 0.46601(y+2.95) + 0.052978(y+2.2)^2 + +0.79575 \exp(-5.4007(y+2.2+4.6121(x+2.2)^2)^2)$ |
| $b_5$ ..... | $1.8756 - 0.42169 \tanh(1.6100(y+1.9)) - 0.051026 * (y-3.9573)$ |
| $b_6$ ..... | $1.5016 + 1.0118y - 0.072787y^2 - 0.0038858y^3 + 0.0093650y^4$ |
| $b_7$ ..... | $4.9735 + 5.5674 \tanh(-0.36249(y+2.1)) - 0.20660 * (y-2.8604)$ |
| | $\Delta(1232)$, eq. 5.10 |
| $c_0$ ..... | $2.8290 \exp(-71.339((y+3.1282)/(1.0+0.48420(y+3.1282)))^2) - 9.6339 - 15.733/y + +0.52413y^2$ |
| $c_1$ ..... | $-24.571 - 15.831y - 2.1200y^2$ |
| $c_2$ ..... | $-5.9593 - 6.4695 \tanh(4.7225(y+2.1)) + 0.50003y$ |
| $c_3$ ..... | $0.26022 + 0.24545y$ |
| $c_4$ ..... | $0.076498 + 0.061678y + 0.0040028y^2$ |
| | res(1600), eq. 5.11 |
| $d_0$ ..... | $1.7951 \exp(-57.260((y+2.9509)/(1.0+1.4101(y+2.9509)))^2) - 0.58604 - 0.23868y$ |
| $d_1$ ..... | $-2.6395 - 1.5105y + 0.22174y^2$ |
| $d_2$ ..... | $-7.0512 - 7.1970 \tanh(31.074(y+2.1)) + 0.39007y$ |
| $d_3$ ..... | $-1.4271 - 1.0399y - 0.24179y^2$ |
| $d_4$ ..... | $0.74875 + 0.63616y + 0.17396y^2 + 0.017636y^3$ |

[a] $b_0, \ldots, b_3 = 0$ for $T_p < 11.05$ GeV

**Table C.6:** Parameters describing electron anti-neutrino spectra for arbitrary proton energy

| Parameter | Formulae as functions of proton kinetic energy ($y = \log T_p$) in TeV. |
|---|---|
| | Non-diff., eq. 5.7 |
| $a_0$ ..... | $0.0013113 + 0.36538(y+3.31) + 1.5178(y+3.31)^2 - 0.20668(y+3.31)^3 + +0.024255(y+3.31)^4$ |
| $a_1$ ..... | $-4.7833 \cdot 10^{-6} + 4.5837 \cdot 10^{-5} \exp(-0.42980(y+3.4)) + 6.1559 \cdot 10^{-6}/(y+4.1731) + +1.1928 \cdot 10^{-6} y$ |
| $a_2$ ..... | $-245.22 + 73.223y - 19.652y^2 + 0.083138y^3 + 0.71561y^4$ |
| $a_3$ ..... | $0.45232 + 0.52934y + 0.010078y^2 - 0.0017092y^3$ |
| $a_4$ ..... | $-0.0025734 + 0.38424(y+3.32) + 1.5517(y+3.32)^2 + 0.17336(y+3.32)^3 + -0.17160(y+3.32)^4 + 0.021059(y+3.32)^5$ |
| $a_5$ ..... | $4.7673 \cdot 10^{-5} + 5.4936 \cdot 10^{-5} \log(0.0067905(y+4.3)) + 0.00020740/(y+4.9772)$ |
| $a_6$ ..... | $-270.30 - 114.47 \log(0.34352(y+3.4)) + 80.085y - 7.9240y^2$ |
| $a_7$ ..... | $3272.9 - 2.9161 \cdot 10^5/(y+87.847) - 6.2330y^2$ |
| $a_8$ ..... | $-0.17787 + 0.36771y - 0.025397y^2 + 0.0019238y^3 + 0.0032725y^4$ |
| $r(y)$ ..... | $2.67 \exp(-45.7((y+3.27)/(1+6.59(y+3.27)))^2) - 0.301y - 0.208y^2$; $T_p \leq 15.6$ GeV<br>1.0; $T_p > 15.6$ GeV |
| | Diffraction, eq. 5.9[a] |
| $b_0$ ..... | $41.307 \tanh(-0.37411(y+2.2)) - 4.1223(y+0.55505)^2 + 0.0042652(y+9.2685)^4$ |
| $b_1$ ..... | $-132.50 + 142.12 \exp(-8.0289((y+1.9196)/(1.0+11.530(y+1.9196)))^2)$ |
| $b_2$ ..... | $-17.223 + 0.011285 \tanh(-69.746(y+1.9)) - 0.048233y + 2.5881 \cdot 10^{-4}(y+250.77)^2$ |
| $b_3$ ..... | $8.1991 - 9.6437 \exp(-45.261((y+1.9292)/(1.0+16.682(y+1.9292)))^2)$ |
| $b_4$ ..... | $0.55919 + 0.36647(y+2.95)^2 + 0.056194(y+2.95)^4 + +0.49957 \exp(-5.5317(y+2.2+0.43867(y+2.2)^2)^2)$ |
| $b_5$ ..... | $1.2544 - 0.52362 \tanh(2.7638(y+1.9)) + 0.055837 * (y - 17.638)$ |
| $b_6$ ..... | $1.4788 + 1.0278y - 0.092852y^2 - 0.0062734y^3 + 0.011920y^4$ |
| $b_7$ | $5.1651 + 5.7398 \tanh(-0.37356(y+2.1)) - 0.22234 * (y - 2.7889)$ |
| | res(1600), eq. 5.11 |
| $d_0$ ..... | $0.36459 \exp(-58.210((y+2.9537)/(1.0+1.4320(y+2.9537)))^2) - 0.11283 - 0.046244y$ |
| $d_1$ ..... | $-9.5066 - 5.4655y - 0.31769y^2$ |
| $d_2$ ..... | $-7.1831 - 7.1551 \tanh(30.354(y+2.1)) + 0.33757y$ |
| $d_3$ ..... | $2.7938 + 1.6992y + 0.20161y$ |
| $d_4$ ..... | $0.61878 + 0.62371y + 0.18913y^2 + 0.019118y^3$ |

[a] $b_0, \ldots, b_3 = 0$ for $T_p < 11.05$ GeV

**Table C.7:** Parameters describing muon neutrino spectra for arbitrary proton energy

| Parameter | Formulae as functions of proton kinetic energy ($y = \log T_p$) in TeV. |
|---|---|
| | Non-diff., eq. 5.7 |
| $a_0$ ..... | $-0.63611(y+3.3) + 9.9015(y+3.3)^2 - 4.5897(y+3.3)^3 + 0.91778(y+3.3)^4 + -0.060724(y+3.3)^4$ |
| $a_1$ ..... | $6.8700 \cdot 10^{-6} - 2.8245 \cdot 10^{-6} y + 7.6032 \cdot 10^{-7} y^2 - 3.2953 \cdot 10^{-7} y^3 + 7.4292 \cdot 10^{-8} y^4$ |
| $a_2$ ..... | $-240.46 + 58.405y - 9.8556y^2 + 3.1401y^3 - 0.88932y^4$ |
| $a_3$ ..... | $0.49935 + 0.60919y + 0.0024963y^2 - 0.0099910y^3$ |
| $a_4$ ..... | $2.5094(y+3.32) + 4.1350(y+3.32)^2 - 0.89534(y+3.32)^3 - 0.0027577(y+3.32)^4 + +0.014511(y+3.32)^5$ |
| $a_5$ ..... | $8.2046 \cdot 10^{-7} + 1.4085 \cdot 10^{-6} \log(0.016793(y+4.3)) + 0.00013340/(y+4.7136)^2$ |
| $a_6$ ..... | $-267.55 - 0.21018 \log(0.35217(y+3.9)) + 69.586y - 9.9930y^2$ |
| $a_7$ ..... | $2742.8 + 222.01 \log(9.7401(y+3.9)) - 4772.5/(y+19.773) - 6.1001y^2$ |
| $a_8$ ..... | $-0.11857 + 0.39072y - 0.037813y^2 + 0.0022265y^3 + 0.0046931y^4$ |
| $r(y)$ ..... | $2.23 \exp(-93.4((y+3.25)/(1+8.38(y+3.25)))^2) - 0.376y - 0.121y^2$; $T_p \leq 15.6$ GeV 1.0; $T_p > 15.6$ GeV |
| | Diffraction, eq. 5.9[a] |
| $b_0$ ..... | $64.682 \tanh(-0.34313(y+2.2)) - 5.5955(y+0.44754)^2 + 0.0050117(y+9.9165)^4$ |
| $b_1$ ..... | $-7.6016 + 3.0427 \cdot 10^4 \exp(-1.0134 \cdot 10^4((y+2.3066)/(1.0+41.612(y+2.3066)))^2)$ |
| $b_2$ ..... | $-1.4978 - 0.58163 \tanh(-0.36488(y+1.9)) + 0.031825(y+2.8097) + +0.022796(y-1.8861)^2$ |
| $b_3$ ..... | $-0.0061483 - 65.799 \exp(-4.8239((y+3.8835)/(1.0+0.53343(y+3.8835)))^2)$ |
| $b_4$ ..... | $2.8009 + 0.35341(y+2.95)^2 - 0.0039779(y+2.95)^4 + +1.3012 \exp(-10.592(y+2.2-0.19149(y+2.2)^2)^2)$ |
| $b_5$ ..... | $1.8016 - 0.69847 \tanh(2.8627(y+1.9)) - 0.015722 * (y-45.4)$ |
| $b_6$ ..... | $1.4617 + 1.0167y - 0.078617y^2 - 0.0038336y^3 + 0.010141y^4$ |
| $b_7$ ..... | $3.5599 + 4.0041 \tanh(-0.41889(y+2.1)) - 0.18182 * (y-2.4209)$ |
| | $\Delta(1232)$, eq. 5.10 |
| $c_0$ ..... | $3.6052 \exp(-60.914((y+3.1278)/(1.0-0.19497(y+3.1278)))^2) - 0.92514 + 2.1315/y + +0.23548y^2$ |
| $c_1$ ..... | $95.310 + 70.497y + 13.636y^2$ |
| $c_2$ ..... | $-6.2158 - 6.2939 \tanh(21.592(y+2.1)) + 0.37440y$ |
| $c_3$ ..... | $2.7485 + 1.1692y$ |
| $c_4$ ..... | $-2.7568 - 1.8461y - 0.31376y^2$ |
| | res(1600), eq. 5.11 |
| $d_0$ ..... | $2.5489 \exp(-58.488((y+2.9509)/(1.0+1.3154(y+2.9509)))^2) - 0.83039 - 0.34412y$ |
| $d_1$ ..... | $88.173 + 65.148y + 12.585y^2$ |
| $d_2$ ..... | $-7.0962 - 7.1690 \tanh(30.890(y+2.1)) + 0.38032y$ |
| $d_3$ ..... | $-4.1440 - 3.2717y - 0.70537y^2$ |
| $d_4$ ..... | $2.2624 + 1.1806y - 0.0043450y^2 - 0.043020y^3$ |

[a] $b_0, \ldots, b_3 = 0$ for $T_p < 11.05$ GeV

**Table C.8:** Parameters describing muon anti-neutrino spectra for arbitrary proton energy

| Parameter | Formulae as functions of proton kinetic energy ($y = \log T_p$) in TeV. |
|---|---|
| | Non-diff., eq. 5.7 |
| $a_0$ ..... | $-1.5243(y+3.3) + 10.107(y+3.3)^2 - 4.3126(y+3.3)^3 + 0.80081(y+3.3)^4 + -0.048724(y+3.3)^5$ |
| $a_1$ ..... | $-2.6297 \cdot 10^{-5} + 9.3858 \cdot 10^{-5} \exp(-0.32384(y+3.4)) + 7.7821 \cdot 10^{-6}/(y+4.0560) + +7.6149 \cdot 10^{-6} y - 8.4091 \cdot 10^{-6} y^2$ |
| $a_2$ ..... | $-223.62 + 59.374y - 5.7356y^2 + 1.9815y^3 - 1.0478y^4$ |
| $a_3$ ..... | $0.50807 + 0.60221y + 0.0034120y^2 - 0.011139y^3$ |
| $a_4$ ..... | $2.6483(y+3.32) + 4.4585(y+3.32)^2 - 1.2744(y+3.32)^3 - 0.11659(y+3.32)^4 + +0.0030477(y+3.32)^5$ |
| $a_5$ ..... | $9.1101 \cdot 10^{-7} + 1.3880 \cdot 10^{-6} \log(0.016998(y+4.3)) 1.2744 \cdot 10^{-4}/(y+4.7707)^2$ |
| $a_6$ ..... | $-272.11 - 53.477 \log(0.35531(y+3.9)) + 56.041/(y-6.0876)^2$ |
| $a_7$ ..... | $6431.8 + 893.92 \log(5.713 \cdot 10^{-9}(y+3.9)) + 2103.6/(y+5.6740) - 6.1125y^2$ |
| $a_8$ ..... | $-0.11120 + 0.38144y - 0.040128y^2 + 0.0047484y^3 + 0.0054707y^4$ |
| $r(y)$ ..... | $2.56 \exp(-107((y+3.25)/(1+8.34(y+3.25)))^2) - 0.385y - 0.125y^2$; $T_p \leq 15.6$ GeV<br>1.0; $T_p > 15.6$ GeV |
| | Diffraction, eq. 5.9[a] |
| $b_0$ ..... | $70.430 \tanh(-0.35816(y+2.2)) - 6.6796(y+0.52273)^2 + 0.0065659(y+9.5266)^4$ |
| $b_1$ ..... | $-8.1145 + 7686.0 \exp(4.4046 \cdot 10^4((y+2.2190)/(1.0+81.105(y+2.2190)))^2)$ |
| $b_2$ ..... | $-1.3095 + 0.071270 \tanh(-0.0075463(y+1.9)) + 0.067759(y+5.3433) + -0.0044205(y-1.8683)^2$ |
| $b_3$ ..... | $0.082149 - 2190.1 \exp(-533.75((y+2.8363)/(1.0+7.0976(y+2.8363)))^2)$ |
| $b_4$ ..... | $2.7540 + 0.33859(y+2.95)^2 - 0.0034274(y+2.95)^4 + +1.1679 \exp(-10.408(y+2.2-0.18922(y+2.2)^2)^2)$ |
| $b_5$ ..... | $2.1817 - 0.59584 \tanh(2.7054(y+1.9)) - 0.010909 * (y-14.9)$ |
| $b_6$ ..... | $1.4591 + 1.0275y - 0.074949y^2 - 0.0060396y^3 + 0.0097568y^4$ |
| $b_7$ ..... | $3.7609 + 4.2843 \tanh(-0.37148(y+2.1)) - 0.16479 * (y-2.7653)$ |
| | $\Delta(1232)$, eq. 5.10 |
| $c_0$ ..... | $2.8262 \exp(-62.894((y+3.1250)/(1.0-0.47567(y+3.1250)))^2) + 5.6845 + 13.409/y + -0.097296y^2$ |
| $c_1$ ..... | $16.721 + 11.750y + 2.4637y^2$ |
| $c_2$ ..... | $-6.0557 - 6.3378 \tanh(21.984(y+2.1)) + 0.43173y$ |
| $c_3$ ..... | $0.37009 + 0.27706y$ |
| $c_4$ ..... | $0.047507 + 0.061570y + 0.0070117y^2$ |
| | res(1600), eq. 5.11 |
| $d_0$ ..... | $2.2400 \exp(-57.159((y+2.9492)/(1.0+1.2994(y+2.9492)))^2) - 0.66521 - 0.27554y$ |
| $d_1$ ..... | $-7.0650 - 4.2773y - 0.17648y^2$ |
| $d_2$ ..... | $-7.0410 - 7.1977 \tanh(31.095(y+2.1)) + 0.40238y$ |
| $d_3$ ..... | $-1.2354 - 0.87581y - 0.20829^2$ |
| $d_4$ ..... | $-0.11395 + 0.34418y + 0.27103y^2 + 0.050248y^3$ |

[a] $b_0, \ldots, b_3 = 0$ for $T_p < 5.52$ GeV

## C.3 Parameters for Gamma-Ray $p_t$ Distributions

**Table C.9:** Parameters describing transverse momentum distributions

| Parameter | Formulae as functions of proton kinetic energy ($y = \log T_p$) in TeV |
|---|---|
| | Non-resonance, eq. (5.27) |
| $a_{10}$ ..... | $0.043775 + 0.010271 \exp(-0.55808y)$ |
| $a_{11}$ ..... | 0.8 |
| $a_{12}$ ..... | $0.34223 + 0.027134y - 0.0089229y^2 + 4.9996 \times 10^{-4} y^3$ |
| $a_{13}$ ..... | $-0.20480 + 0.013372y + 0.13087 \exp\left(0.0044021(y - 11.467)^2\right)$ |
| $a_{14}$ ..... | $a_1(x = -0.75)$ |
| | $\Delta(1232)$, eq. (5.32) |
| $b_{10}$ ..... | $18.712 + 18.030y + 5.8239y^2 + 0.62728y^3$ |
| $b_{11}$ ..... | $612.61 + 404.80y + 67.406y^2$ |
| $b_{12}$ ..... | $98.639 + 96.741y + 31.597y^2 + 3.4567y^3$ |
| $b_{13}$ ..... | $-208.38 - 183.65y - 53.283y^2 - 5.0470y^3$ |
| $b_{20}$ ..... | $0.21977 + 0.064073x$ |
| $b_{21}$ ..... | $3.3187 \times 10^3 + 3463.4y + 1.1982 \times 10^3 y^2 + 136.71y^3$ |
| $b_{22}$ ..... | $91.410 + 91.613y + 30.621y^2 + 3.4296y^3$ |
| $b_{23}$ ..... | $-521.40 - 529.06y - 178.49y^2 - 19.975y^3$ |
| | res(1600), eq. (5.33) |
| $c_{10}$ ..... | $-1.5013 - 1.1281y - 0.19813y^2$ |
| $c_{11}$ ..... | $-33.179 - 22.496y - 3.3108y^2$ |
| $c_{12}$ ..... | $116.44 + 122.11y + 42.594y^2 + 4.9609y^3$ |
| $c_{13}$ ..... | $-545.77 - 574.80y - 201.25y^2 - 23.400y^3$ |
| $c_{20}$ ..... | $0.68849 + 0.36438y + 0.047958y^2$ |
| $c_{21}$ ..... | $-1.6871 \times 10^4 - 1.7412 \times 10^4 y - 5.9648 \times 10^3 y^2 - 679.27y^3$ |
| $c_{22}$ ..... | $-88.565 - 94.034y - 33.014y^2 - 3.8205y^3$ |
| $c_{23}$ ..... | $1.5141 \times 10^3 + 1.5757 \times 10^3 y + 544.20y^2 + 62.446y^3$ |